ABACUS: An Electronic Structure Analysis Package for the AI Era

Weiqing Zhou,[1] Daye Zheng,[1] Qianrui Liu,[2] Denghui Lu,[3,1] Yu Liu,[2] Peize Lin,[4] Yike Huang,[1] Xingliang Peng,[1] Jie J. Bao,[1] Chun Cai,[1] Zuxin Jin,[1] Jing Wu,[1] Haochong Zhang,[4] Gan Jin,[4] Yuyang Ji,[5] Zhenxiong Shen,[4,5] Xiaohui Liu,[6] Liang Sun,[2] Yu Cao,[7,2] Menglin Sun,[8] Jianchuan Liu,[9] Tao Chen,[2] Renxi Liu,[10,1] Yuanbo Li,[2] Haozhi Han,[3,1] Xinyuan Liang,[10] Taoni Bao,[2] Nuo Chen,[3] Hongxu Ren,[3] Xiaoyang Zhang,[3,1] Zhaoqing Liu,[11] Yiwei Fu,[12] Maochang Liu,[12,13] Zhuoyuan Li,[14,15] Tongqi Wen,[14,15] Zechen Tang,[16] Yong Xu,[16,17,18] Wenhui Duan,[16,19,17] Xiaoyang Wang,[20] Qiangqiang Gu,[21,1] Fu-Zhi Dai,[22,1] Qijing Zheng,[23] Jin Zhao,[23] Yuzhi Zhang,[24,1] Qi Ou,[25] Hong Jiang,[11] Shi Liu,[26,27] Ben Xu,[28] Shenzhen Xu,[8,1] Xinguo Ren,[7] Lixin He,[5,4,29] Linfeng Zhang,[24,1] and Mohan Chen[1,2]

[1] *AI for Science Institute, Beijing 100080, China*
[2] *HEDPS, CAPT, School of Physics and College of Engineering, Peking University, Beijing, 100871, China*
[3] *College of Engineering, Peking University, Beijing, 100871, China*
[4] *Institute of Artificial Intelligence, Hefei Comprehensive National Science Center, Hefei 230026, China*
[5] *Key Laboratory of Quantum Information, University of Science and Technology of China, Hefei 230026, China*
[6] *Supercomputing Center, University of Science and Technology of China, Hefei, Anhui 230026, China*
[7] *Institute of Physics, Chinese Academy of Sciences, Beijing 100190, China*
[8] *School of Materials Science and Engineering, Peking University, Beijing 100871, China*
[9] *School of Electrical Engineering and Electronic Information, Xihua University, Chengdu 610039, China*
[10] *Academy for Advanced Interdisciplinary Studies, Peking University, Beijing, 100871, China*
[11] *College of Chemistry and Molecular Engineering, Peking University, Beijing 100871, China*
[12] *International Research Center for Renewable Energy, State Key Laboratory of Multiphase Flow, Xi'an Jiaotong University, Xi'an, Shaanxi 710049, China*
[13] *Suzhou Academy of Xi'an Jiaotong University, Suzhou, Jiangsu 215123, China*
[14] *Center for Structural Materials, Department of Mechanical Engineering, The University of Hong Kong, Hong Kong, China*
[15] *Materials Innovation Institute for Life Sciences and Energy (MILES), The University of Hong Kong, Shenzhen, China*
[16] *State Key Laboratory of Low Dimensional Quantum Physics and Department of Physics, Tsinghua University, Beijing, 100084, China*
[17] *Frontier Science Center for Quantum Information, Beijing, China*
[18] *RIKEN Center for Emergent Matter Science (CEMS), Wako, Saitama 351-0198, Japan*
[19] *Institute for Advanced Study, Tsinghua University, Beijing 100084, China*
[20] *Laboratory of Computational Physics, Institute of Applied Physics and Computational Mathematics, Fenghao East Road 2, Beijing 100094, China*
[21] *School of Artificial Intelligence and Data Science, University of Science and Technology of China, Hefei 230026, China*
[22] *School of Materials Science and Engineering, University of Science and Technology Beijing, Beijing 100083, China*
[23] *Department of Physics, University of Science and Technology of China, Hefei, Anhui 230026, China*
[24] *DP Technology, Beijing 100080, China*
[25] *Basic Research Department, SINOPEC Research Institute of Petroleum Processing Co., Ltd, Beijing 100083, China*
[26] *Department of Physics, School of Science, Westlake University, Hangzhou, Zhejiang 310030, China*
[27] *Institute of Natural Sciences, Westlake Institute for Advanced Study, Hangzhou, Zhejiang 310024, China*
[28] *Graduate School of China Academy of Engineering Physics, Beijing 100193, China*
[29] *Synergetic Innovation Center of Quantum Information and Quantum Physics, University of Science and Technology of China, Hefei, 230026, China*

(*Electronic mail: mohanchen@pku.edu.cn)

(*Electronic mail: helx@ustc.edu.cn)

(*Electronic mail: renxg@iphy.ac.cn)

(Dated: 22 January 2025)

ABACUS (Atomic-orbital Based Ab-initio Computation at USTC) is an open-source software for first-principles electronic structure calculations and molecular dynamics simulations. It mainly features density functional theory (DFT) and is compatible with both plane-wave basis sets and numerical atomic orbital basis sets. ABACUS serves as a platform that facilitates the integration of various electronic structure methods, such as Kohn-Sham DFT, stochastic DFT, orbital-free DFT, and real-time time-dependent DFT, etc. In addition, with the aid of high-performance computing, ABACUS is designed to perform efficiently and provide massive amounts of first-principles data for generating general-purpose machine learning potentials, such as DPA models. Furthermore, ABACUS serves as an electronic structure platform that interfaces with several AI-assisted algorithms and packages, such as DeePKS-kit, DeePMD, DP-GEN, DeepH, DeePTB, etc.

CONTENTS

I. INTRODUCTION

In recent decades, coupled with the development of algorithms and the monumental leap in computational power, Density Functional Theory (DFT)[1,2] has achieved immense success in materials science, physics, and chemistry, among others. To meet the needs of different application scenarios, a multitude of unique DFT software has emerged[3–14]. For instance, the well-established plane-wave basis with pseudopotential method can accurately handle systems containing hundreds of atoms[11,13]. With advancements in high-performance technologies and algorithms, the plane-wave basis set is now capable of addressing systems with thousands or even tens of thousands of atoms[15–19]. Smaller basis sets of localized orbitals can effectively handle systems with thousands of atoms with considerably less computational resources and exhibit lower scaling in small systems[7,12]. Also, linear-scaling algorithms expand the first-principles calculations to larger scales[6,8,9]. All these DFT software packages are dedicated to extending the applicability of DFT in terms of precision and scale, which has significantly contributed to the current popularity and success of density functional theory.

The ABACUS project was initiated before 2006 and has achieved a series of progress over the nearly past 20 years[20–32], supporting both plane-wave (PW) basis and numerical atomic orbitals (NAO) basis for first-principles electronic structure and molecular dynamics calculations. The ABACUS team started to cooperate with the open-source community **DeepModeling** since 2021[33], providing a flexible platform for utilizing various electronic structure methods. For example, based on the plane-wave basis set, low-scaling method stochastic DFT (sDFT) for calculations of warm dense matter has been implemented[29]; and for numerical atomic orbitals, meta-GGA[31] and DFT+U methods have been realized.

The effort to create such an integrated platform is particularly critical today, given the growing intersection of artificial intelligence (AI) and electronic structure algorithms[34–42]. The field of AI is rapidly advancing in algorithm development, thanks to well-built infrastructure such as PyTorch[43] and TensorFlow[44]. In contrast, algorithm research in electronic structure typically spans several years. In the context of a deep integration between AI and electronic structure, this significant discrepancy in development efficiency makes it challenging for electronic structure to keep pace with cutting-edge AI algorithms. To be a competent electronic structure al-
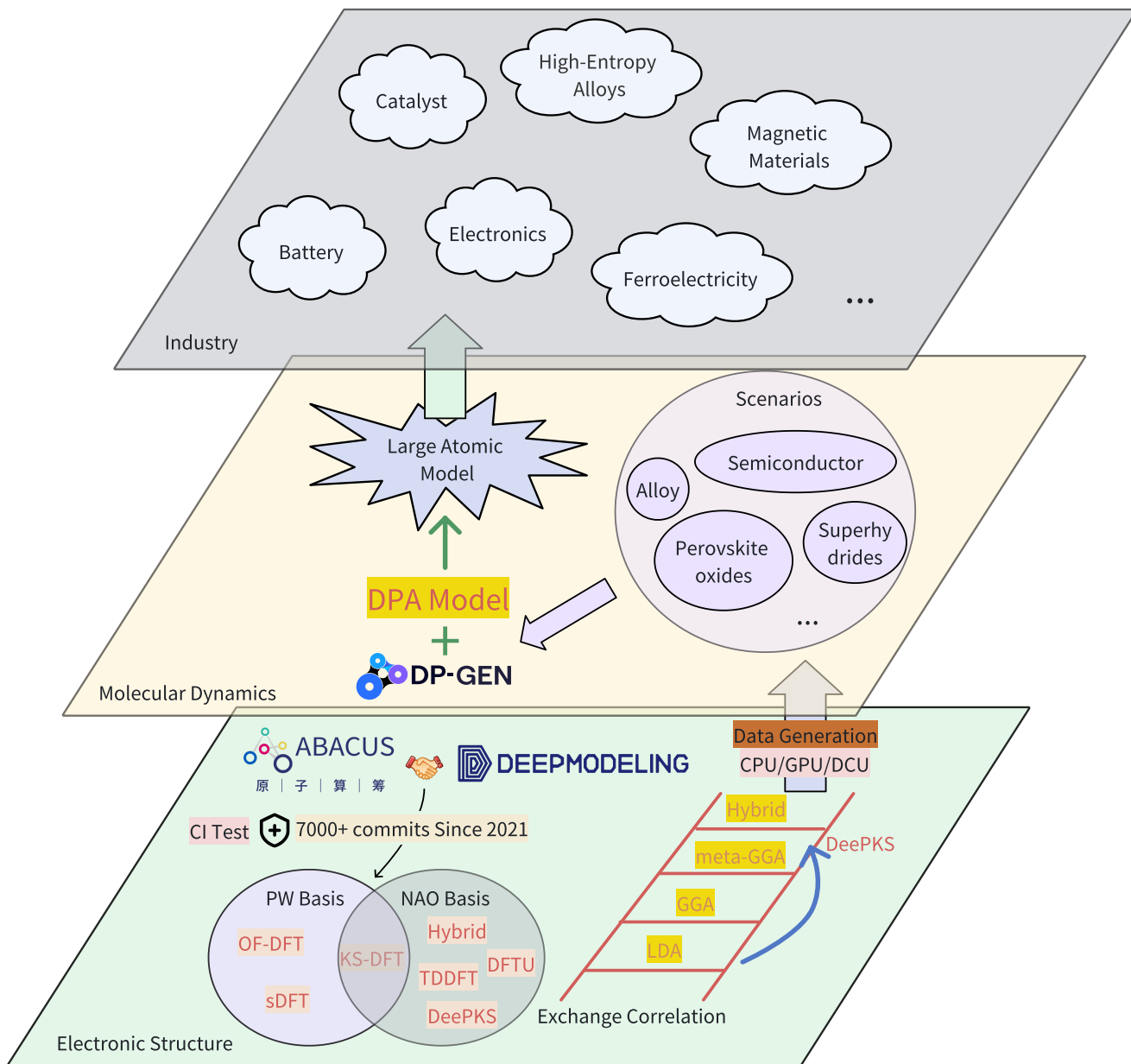
FIG. 1: ABACUS is dedicated to building an algorithm platform and data engine for AI4ES (AI for Electronic Structure). Since partnering with the open-source community **DeepModeling** in 2021, ABACUS has garnered over 7,000 commits under the protection of Continuous Integration (CI) tests. Its adaptable architecture allows developers to incorporate numerous electronic structure algorithms. The AI-assisted functional correction method DeePKS permits ABACUS to achieve precise functional results at a reduced cost. Owing to high-performance implementation at various devices, ABACUS effectively produces extensive first-principles data across multiple sectors. Combining advanced electronic structure algorithms and AI-assisted pre-trained model, one can transfer the precision of quantum mechanics across scales.

gorithm platform in the AI era, one must fulfill the following criteria: code flexibility that allows for rapid implementation of new algorithms; code engineering to ensure stability under high-frequency development; and open community to attract a large number of researchers interested in electronic structure and AI to make ongoing contributions. A notably successful case is the swift implementation of the AI-assisted algorithm

DeePKS[45] in ABACUS, which will be addressed in Sec. V F.

In recent years, the rapid development of generative pre-trained models has offered unprecedented opportunities for unifying models with quantum mechanics. Recently, the Deep Potential team has launched open large atomic model project, namely OpenLAM[46]. Owing to informative testing reports, comprehensive functionality, and high-performance heteroge-

neous implementation, ABACUS effectively meets the needs of OpenLAM for massive and high-precision data production. As depicted in Fig. 1, ABACUS is committed to building an electronic structure algorithm platform and computing engine for the AI4S (AI for Science) era, combining advanced electronic structure algorithms and AI-assisted algorithms to transfer the precision of quantum mechanics across scales.

In this article, we provide a detailed overview of the latest advancements in ABACUS. Sec. III details the theoretical foundations and practical implementation of Kohn-Sham Density Functional Theory (KS-DFT) within ABACUS, including the exchange-correlation functionals, magnetic calculations, self-consistent field iterations, and modifications for surface chemistry, etc. Sec. IV introduces the algorithms based on the plane wave basis employed in ABACUS for KS-DFT, stochastic DFT (sDFT), Orbital-Free DFT (OF-DFT), and its progress in AI-assisted kinetic energy functional. Sec. V discusses methods such as Hybrid Functionals, the DFT+U technique, Real-Time Time-Dependent DFT (RT-TDDFT), and the AI-augmented functional correction method DeePKS, all of which rely on the numerical atomic orbitals basis. Sec. VI concentrates on AI-assisted molecular dynamics and describes ABACUS's role in generating data for the pre-trained model OpenLAM. Meanwhile, Sec. VII presents the interface between ABACUS and other softwares, while Sec. VI A introduces the ongoing pseudopotential orbital library project. Finally, Sec. VIII summarizes the whole review.

II. OVERVIEW OF ABACUS

Despite ABACUS supporting two types of basis sets and various DFT algorithms, the input file format required for these computations is uniform. A typical ABACUS PW calculation requires the user to prepare a few input files in advance. **INPUT** specifies the basic parameters of the calculation. Users can select the type of DFT method to enable through the keyword `esolver_type`, with options including KS-DFT, OF-DFT, sDFT, RT-TDDFT, etc. On the other hand, the keyword `calculation` determines the type of computation, such as self-consistent field calculation, relaxation, and other options. ABACUS only supports pseudopotential first-principles calculations, thus the pseudopotential files are indispensable. ABACUS supports both norm-conserving and ultrasoft pseudopotentials in various formats.

STRU defines the crystal cell, atomic coordinates, and initial magnetic moments. ABACUS adopts periodic boundary conditions (PBCs) for both crystals and finite systems. For isolated systems, such as atoms, molecules, clusters, etc., one can use a large vacuum layer to avoid interactions from atoms in neighboring cells. In ABACUS, the Ewald method is used to solve the divergence problem caused by PBC[47].

KPT specifies the k-point sampling of the first Brillouin zone. However, it can be omitted if the user sets the keyword `kspacing` in **INPUT**. ABACUS offers three versatile templates for k-point configuration. The first mode reads the number of k-point grids in three dimensions and uniformly sam-

ples the Brillouin zone using the Monkhorst-Pack method[48], with the option to center k-point sampling at the Gamma point or not. In the second mode, users provide the coordinates and weights of specific k-points directly. The third mode is designed for band structure calculations, where users designate high-symmetry points and the number of k-points between them. For larger systems, ABACUS's Gamma-Only mode employs real wavefunctions to save time and resources.

ABACUS PW calculations can be activated with the input settings introduced above and optionally with `basis_type=pw` in the **INPUT** file. For ABACUS LCAO (Linear combination of atomic orbitals) calculation, alternatively the `basis_type=lcao`, and additional numerical atomic orbital files ***.orb** are needed. We provide fully ready-to-use orbital files for users on the official website[49].

For new feature developers, ABACUS offers highly modular code that allows one to implement new functionalities quickly in a Lego-like assembly way. For core developers, a clear dependency ensures that different modules can be optimized locally. All joint efforts are intended to make ABACUS a user- and developer-friendly software.

III. KOHN-SHAM DENSITY FUNCTIONAL THEORY

A. Kohn-Sham Equation

In 1964, Hohenberg and Kohn[1] demonstrated that the energy of a non-degenerate ground state can be uniquely obtained from a density functional of the electronic density of this system, whereas the exact form of such density functional is unknown. In 1965, Kohn and Sham[2] proposed what is later referred to as the Kohn-Sham density functional theory (KS-DFT), where a Slater determinant is used to compute the non-interacting kinetic energy, as well as the densities for computing the electron-nuclear, classical electron-electron, and the non-classical energy. The non-classical energy is obtained from an exchange-correlation functional of density and other ingredients (see discussions in Sec. III for details of the ingredients), so the non-classical energy is more often called the exchange-correlation energy. In KS-DFT, the orbitals are obtained by solving the KS equation

$$\left(-\frac{1}{2}\nabla^2 + \hat{V}_{\text{KS}} \right) |\psi_j\rangle = \varepsilon_j |\psi_j\rangle, \tag{1}$$

where $|\psi_j\rangle$ is a Kohn-Sham orbital with energy ε_j, and $\hat{V}_{\text{KS}}$ is called the KS potential:

$$\hat{V}_{\text{KS}} = \hat{V}_{\text{ext}} + \hat{V}_{\text{H}} + \hat{V}_{\text{xc}}, \tag{2}$$

where the three terms on the right-hand side are called the external-filed term, the Hartree term, and the exchange-correlation (XC) term, respectively. In ABACUS, the Hartree potential is calculated via fast Fourier transforms under periodic boundary conditions[47].

The KS orbitals in Eq. 1 can be expressed on various types of basis functions, such as plane waves[5,11,13], numerical atomic orbitals[6,12,50,51], real-space grids[8,52], Gaussian orbitals[7,14], wavelet basis sets[53], etc. ABACUS supports both
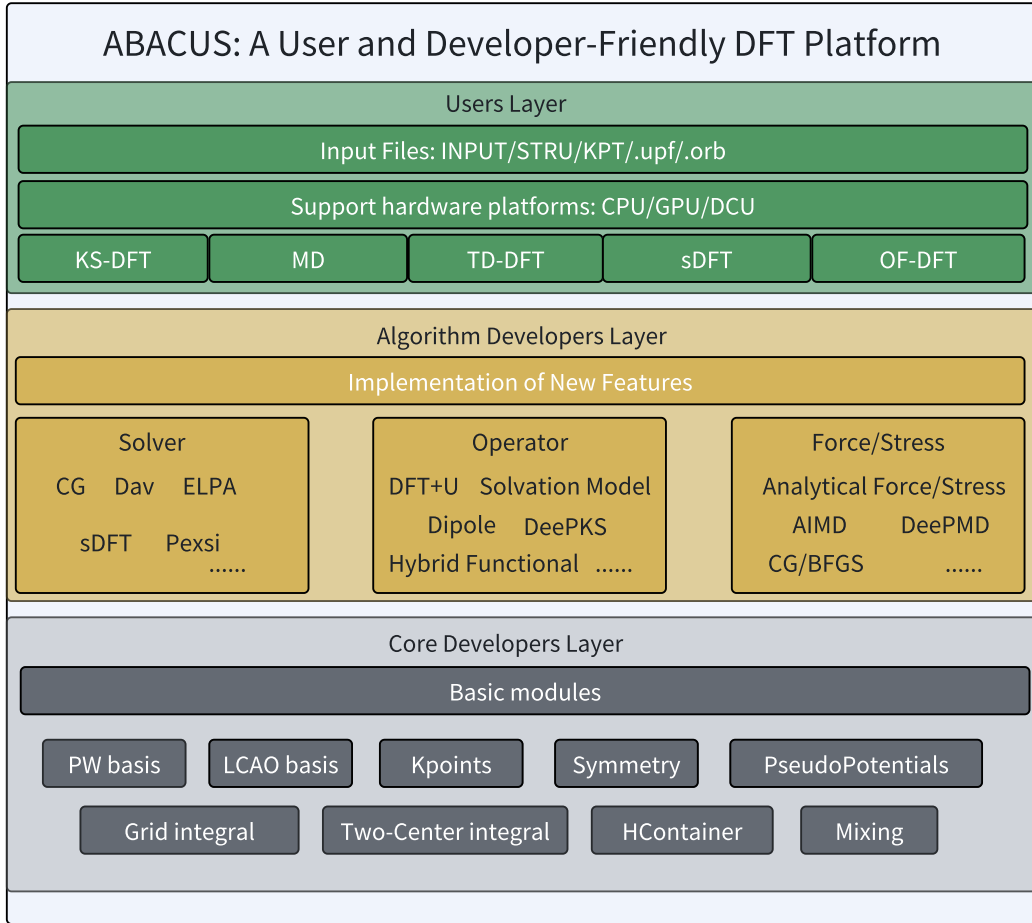
FIG. 2: Code architecture of ABACUS. For users, a few input files need to be prepared in advance, including **INPUT**, **STRU**, **KPT**, pseudopotential files, and orbital files (only for numerical atomic orbitals calculations). For developers who are new to ABACUS, the software features a highly modular design that allows for the swift integration of new functionalities. The core development team is responsible for formulating and refining key data structures, mathematical routines, and other foundational components in ABACUS. For instance, the `HContainer` module is utilized for storing sparse matrices under the numerical atomic orbital basis set, such as Hamiltonian and density matrices; the `Grid Integral` module is implemented for grid integration.

plane waves (PWs) and numerical atomic orbitals (NAOs) as basis sets, which are introduced in Sec. IV and Sec. V, respectively.

1. Pseudopotentials

The external-field term, in absence of external electric field, is computed from a pseudopotential term. First-principles pseudopotentials are essential tools to increase the efficiency in quantum mechanical calculations. A pseudopotential approximates the effect of core electrons and represents the ion core through a simpler potential, which allows valence electrons to be treated explicitly within manageable computational resources.

Several forms of pseudopotentials are now widely used in electronic structure calculations. For example, the norm-conserving pseudopotentials (NCPP)[54,55] ensure that pseudo-wavefunctions coincide with true wavefunctions outside a certain cutoff radius, while the norm of pseudo-wavefunctions is conserved.

The pseudopotential, $\hat{V}^{\mathrm{PS}}$, consists of a local part and a nonlocal part, namely,

$$\hat{V}^{\mathrm{PS}} = V_{\mathrm{local}}(r) + \hat{V}^{\mathrm{KB}}. \tag{3}$$

Here, the nonlocal operator is written in the fully nonlocal form proposed by Kleinman and Bylander (KB)[56]

$$\hat{V}^{\mathrm{KB}} = \sum_{ll'mm'} D_{ll'} |\beta_{lm}^{\mathrm{KB}}\rangle \langle \beta_{l'm'}^{\mathrm{KB}}|, \tag{4}$$

which projects $D_{ll'}$ onto a set of pseudo-atomic orbital bases, β_{lm}^{KB}, with an angular quantum number l and a magnetic quantum number m. The pseudo-atomic-orbital basis function is

expressed as a product of a spherical harmonic function and a radial function, namely

$$\beta_{lm}^{\mathrm{KB}}(\mathbf{r}) = \phi_{lm}^{\mathrm{ps}}(r) Y_{lm}(\theta, \phi). \tag{5}$$

Furthermore, the ultrasoft pseudopotentials (USPP)[13,57] allow for higher computational efficiency by relaxing the norm-conservation condition. The result is more flexibility in the pseudo-wavefunction within the core region, which in turn means that softer waves can be used. This yields faster-converging basis sets but requires a more sophisticated approach to solve the Kohn-Sham equation.

2. Exchange-Correlation Functional

Many density functional approximations (DFAs) have been proposed since the publication of KS-DFT. The earliest realization of KS-DFA is local density approximation (LDA), which is the functional of the spin-summed electron density $\rho(\mathbf{r})$. One also finds that using spin density components, namely $\rho_\uparrow$ and $\rho_\downarrow$, together with a broken-symmetry Slater determinant, gives correct dissociation limit of H_2, and the resulting DFA is called local spin density approximation (LSDA).

Density gradients, or spin density gradients, were then introduced as an ingredient to the density functional, resulting in a generalized gradient approximation (GGA) functional. The accuracy of GGAs is greatly improved from the LDA or LSDA functionals, for example, PBE[58] reduces mean absolute error (MAE) of the atomization energies for 20 main-group molecules to 7.9 kcal/mol, whereas the MAE of LSDA is 31.4 kcal/mol.

The next generation of successful DFA is called meta-GGA, to which the introduction of the kinetic energy density, $\tau(\mathbf{r})$, shows improved accuracy compared with GGAs. A widely-used meta-GGA functional is the strongly constrained and appropriately normed (SCAN) functional[59].

The above-mentioned DFAs use only the local ingredients, which depend solely on a grid point $\mathbf{r}$ in space. However, one may also include a fraction of exact Hartree-Fock exchange energy, and the resulting functional is called hybrid DFA, such as the HSE03 functional[60].

In ABACUS, LDA (and LSDA), GGA, and meta-GGA functionals are implemented with both the plane-wave and the atomic-orbital basis sets. The LDA and GGA functionals are available from both home-built codes and the Libxc library[61]. Meta-GGA functionals, however, can only be used with Libxc in the current version of ABACUS. We refer audiences to Ref. 31 for testings of SCAN, rSCAN[62], and r2SCAN[63] on ABACUS. Hybrid functionals are available only with the LCAO basis set in combination with the Libxc and the local resolution of identity (LRI) libraries (More discussions can be found in Sec. V E on how hybrid functionals are computed in ABACUS).

3. Collinear and Non-Collinear Spin

Extending the original spinless KS-DFT to incorporate collinear spin densities involves assigning distinct treatment to the spin-up and spin-down electron populations. In this formalism, each electron is strictly aligned either parallel (spin-up) or antiparallel (spin-down) to a chosen quantization axis. Spin densities for spin up and down channels are defined as $\rho_\uparrow(\mathbf{r})$ and $\rho_\downarrow(\mathbf{r})$, respectively. The total electron density is

$$\rho(\mathbf{r}) = \rho_\uparrow(\mathbf{r}) + \rho_\downarrow(\mathbf{r}) \tag{6}$$

while the spin density takes the form of

$$m(\mathbf{r}) = \rho_\uparrow(\mathbf{r}) - \rho_\downarrow(\mathbf{r}). \tag{7}$$

The spin-dependent Kohn-Sham equation has effective potentials from the external, Hartree, and exchange-correlation potentials, with the latter now explicitly dependent on both the spin-up and spin-down densities.

The exchange-correlation potential V_{XC} is split into two components $V_{\mathrm{XC},\uparrow}(\mathbf{r})$ and $V_{\mathrm{XC},\downarrow}(\mathbf{r})$, which are derived from the derivative of the exchange-correlation energy $E_{\mathrm{XC}}[\rho_\uparrow, \rho_\downarrow]$ with respect to the electron density

$$V_{\mathrm{XC},\sigma}(\mathbf{r}) = \frac{\delta E_{\mathrm{XC}}[\rho_\uparrow, \rho_\downarrow]}{\delta \rho_\sigma(\mathbf{r})}, \tag{8}$$

where σ represents either spin-up or spin-down electrons. Similarly to spinless cases, the approximations of E_{XC} include the local spin density approximation (LSDA)[64], where E_{XC} depends only on the local spin densities. In addition, the generalized gradient approximation E_{XC} also depends on the gradients of the spin densities. More sophisticated methods incorporate additional ingredients, such as the kinetic energy density for meta-GGA and occupied KS orbitals for hybrid functionals.

The non-collinear spin calculation permits electron spins to orient in arbitrary directions rather than being restricted to a single axis. In the non-collinear spin KS-DFT, the Kohn-Sham electronic wave function i can be represented as two-component spinors as

$$\Psi_i(\mathbf{r}) = \begin{pmatrix} \psi_{i\uparrow}(\mathbf{r}) \\ \psi_{i\downarrow}(\mathbf{r}) \end{pmatrix}. \tag{9}$$

The density matrices with spin indices $\rho^{\sigma\sigma'}$, where $\sigma\sigma'$ refer to the spin-spin indices of $\uparrow\uparrow, \uparrow\downarrow, \downarrow\uparrow, \downarrow\downarrow$, can be expressed using charge density ρ, spin density m and Pauli matrices σ for each grid $\mathbf{r}$

$$\begin{pmatrix} \rho^{\uparrow\uparrow} & \rho^{\uparrow\downarrow} \\ \rho^{\downarrow\uparrow} & \rho^{\downarrow\downarrow} \end{pmatrix} = (\rho \boldsymbol{I} + \boldsymbol{\sigma} \cdot \boldsymbol{m}) = \frac{1}{2} \begin{pmatrix} \rho + m_z & m_x - im_y \\ m_x + im_y & \rho - m_z \end{pmatrix}. \tag{10}$$

where $\boldsymbol{I}$ is $2*2$ diagonal matrix, $m_i|_{i=x,y,z}$ refer to magnetic density along three axis.

The exchange-correlation potential V_{xc} in the presence of non-collinear spins becomes a 2×2 matrix that acts on these spinors

$$V_{\mathrm{xc}}(\mathbf{r}) = \begin{pmatrix} V_{\mathrm{xc}}^{\uparrow\uparrow}(\mathbf{r}) & V_{\mathrm{xc}}^{\uparrow\downarrow}(\mathbf{r}) \\ V_{\mathrm{xc}}^{\downarrow\uparrow}(\mathbf{r}) & V_{\mathrm{xc}}^{\downarrow\downarrow}(\mathbf{r}) \end{pmatrix}, \tag{11}$$

where the off-diagonal terms $V_{xc}^{\uparrow\downarrow}$ and $V_{xc}^{\downarrow\uparrow}$ represent the non-collinear components of the potential, which mix the spin-up and spin-down states due to spin-orbit coupling (SOC) or other magnetic interactions.

Taking advantage of the Pauli matrices, the exchange-correlation potential can be converted into:

$$
\begin{aligned}
v_{xc}(\mathbf{r}) &= \frac{\delta E_{xc}}{\delta \rho(\mathbf{r})} = \frac{1}{2}(V_{xc}^{\uparrow\uparrow}(\mathbf{r}) + V_{xc}^{\downarrow\downarrow}(\mathbf{r})), \\
b_{xc}^{x}(\mathbf{r}) &= \frac{\delta E_{xc}}{\delta m_x(\mathbf{r})} = \frac{1}{2}(V_{xc}^{\uparrow\downarrow}(\mathbf{r}) + V_{xc}^{\downarrow\uparrow}(\mathbf{r})), \\
b_{xc}^{y}(\mathbf{r}) &= \frac{\delta E_{xc}}{\delta m_y(\mathbf{r})} = \frac{1}{2}(i(V_{xc}^{\uparrow\downarrow}(\mathbf{r}) - V_{xc}^{\downarrow\uparrow}(\mathbf{r}))(\mathbf{r})), \\
b_{xc}^{z}(\mathbf{r}) &= \frac{\delta E_{xc}}{\delta m_z(\mathbf{r})} = \frac{1}{2}(V_{xc}^{\uparrow\uparrow}(\mathbf{r}) - V_{xc}^{\downarrow\downarrow}(\mathbf{r})).
\end{aligned}
\tag{12}
$$

Following this format, the charge density and exchange-correlation potential can be stored as real numbers rather than as complex numbers in the spinor format. When constructing the Hamiltonian, however, it is necessary to convert the exchange-correlation potential back into the spinor format to act on the two-component spinor wavefunctions. This approach facilitates the handling of non-collinear spin configurations within the DFT framework.

In ABACUS, the spin-orbit coupling effect are introduced through the non-local terms of the norm-conserving pseudopotentials using the Kleinman-Bylander (KB) projector[54,55] formalism. The projector orbitals are expanded using complex spherical harmonics Y_{lj} with orbital angular moment l and total angular moment j rather than the real spherical harmonics Y_{lm}. Given that the complex spherical harmonics Y_{lj} can be expressed as combinations of the real spherical harmonics Y_{lm}, the formula of the non-local terms[65,66] can be reformulated accordingly

$$
V_{NL}^{\sigma\sigma'} = \sum_{\tau}\sum_{pp'} D_{\tau lj} \left[\sum_{m_j=-j}^{j} \alpha_{m_j}^{\sigma lj} U_{m_j m}^{\sigma lj} \alpha_{m_j}^{\sigma' lj} U_{m_j m}^{*\sigma' lj} \right] \\
\left| \beta_{\tau p} Y_{lm} \right\rangle \left\langle Y_{lm'} \beta_{\tau p'} \right|,
\tag{13}
$$

where $U_{jm}^{\sigma lj}$ are unitary matrix and $\alpha_{m_j}^{\sigma lj}$ are Clebsch-Gordan coefficients, $D_{\tau lj}$ are radial pseudopotential components of non-local part with atom τ and $j = l + \frac{1}{2}$ for $l >= 0$ and $j = l - \frac{1}{2}$ for $l > 0$. Norm-Conserving pseudopotential with SOC effect is labeled as "full-relativistic" (FR), to distinguish them from "scalar-relativistic" (SR), which considers the relativistic mass correction without spin-orbit interactions.

B. Self-Consistent Field Method

The self-consistent field (SCF) method is an iterative method to update the electron density and solve the KS equation. For each electronic step during the SCF calculations, an input electron density ρ_{in} is used to construct the Hamiltonian, and an output electron density ρ_{out} is constructed from the Kohn-Sham wave functions. Typically, the self-consistency

is achieved when the electron density is converged within a threshold.

Essentially, in order to obtain stable and efficient convergence during the SCF calculations for the nonlinear Kohn-Sham equation, several charge mixing methods have been proposed[67–69]. In this regard, a residual vector can be defined as

$$
R[\rho_{\text{in}}] = \rho_{\text{out}} - \rho_{\text{in}}.
\tag{14}
$$

The simplest mixing method is so-called plain mixing, where the input density of $(i+1)$-th iteration is determined by

$$
\rho_{in}^{i+1} = \rho_{in}^{i} + \alpha_\rho R[\rho_{in}^{i}],
\tag{15}
$$

where $\alpha_\rho \in [0,1]$ specifies the linear mixing parameter.

Effective mixing algorithms aid the SCF procedure in correctly identifying the ground state, preventing entrapment in local minima, and avoiding convergence to excited states. Fig. 3 demonstrates that ABACUS incorporates sophisticated preconditioning and mixing strategies to guarantee stable and dependable SCF convergence. We will now provide a detailed discussion of these algorithms.

1. Modified Kerker Preconditioner

During SCF procedure, it is reasonable to assume that when the input charge density approaches the ground state charge density, the residual density relates proportionally to the discrepancy between the input charge density and the ground state charge density. In the context of linear response theory, the residual density is intricately associated with the dielectric function. The pace of convergence is primarily contingent upon $\overline{\Gamma}$, which signifies the energy spectrum of the dielectric function ε[70].

Mixing methods that forgo a preconditioner adopt a rudimentary dielectric matrix characterized by unity across its diagonal elements, that is, $\varepsilon(q) = 1$. This simplification may suffice for insulators or semiconductors where the dielectric function demonstrates gradual variation, in contrast to metals where it is subject to notable fluctuations. To address the issues with metals' dielectric functions, a preconditioning approach, known as the Kerker preconditioner, incorporates a factor of $\frac{q^2}{q^2+q_0^2}$ for varying wavevector $\boldsymbol{q}$ to modulate the influence of distinct components[70], where $q = |\boldsymbol{q}|$ is the module of wavevector and q_0 is the damping parameter. Although this adjustment originates from the uniform electron gas model, it can significantly reduce long-range charge oscillations and accelerate convergence.

Excessive damping of the long-wavelength components of charge density sometimes impedes convergence. To this end, ABACUS has implemented a modified Kerker preconditioner method from v3.5.0. This method sets a minimum threshold K_{min}, safeguarding a minimum proportion of the long-wavelength contribution by setting the prefactor to $\max\{\alpha_\rho \frac{q^2}{q^2+q_0^2}, K_{\text{min}}\}$[72].

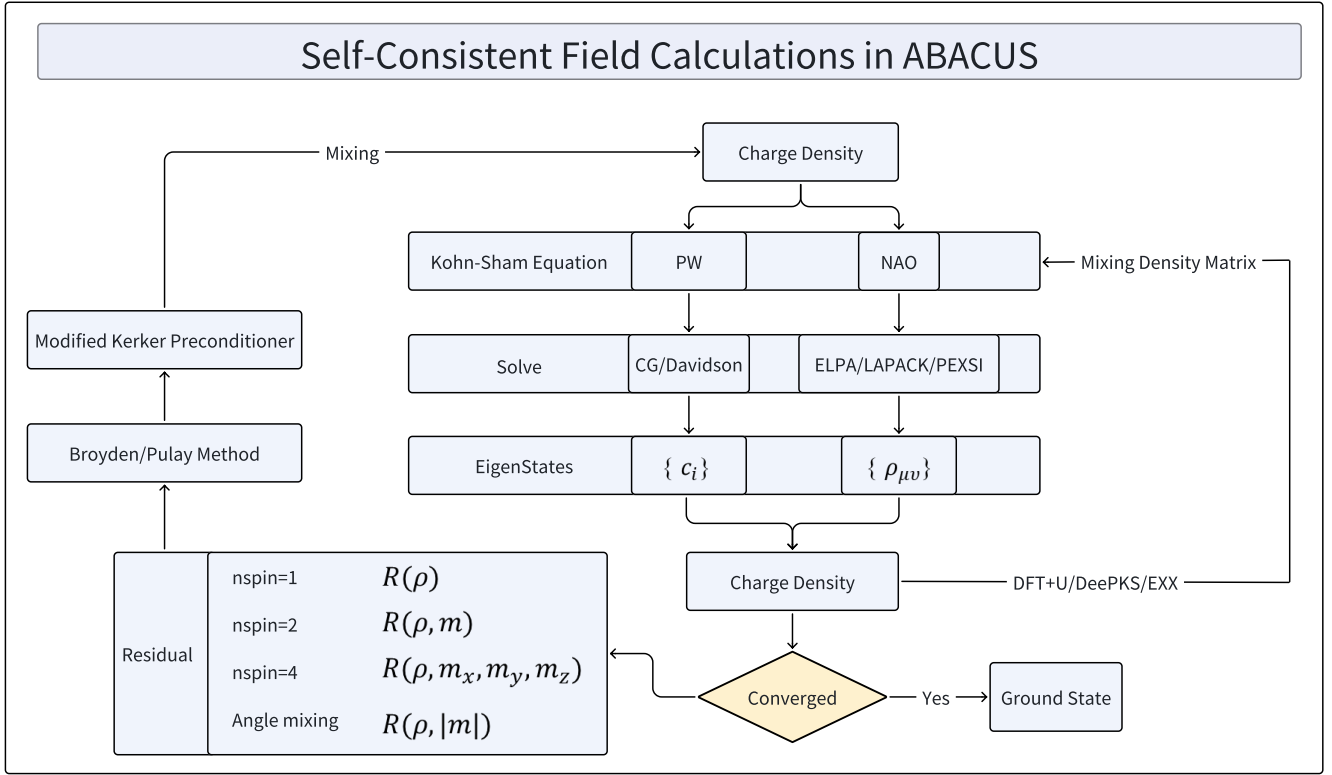## Self-Consistent Field Calculations in ABACUS

FIG. 3: ABACUS performs self-consistent field calculations using two types of basis sets: PW and NAOs. The PW basis set employs iterative diagonalization methods like CG and Davidson to solve the Kohn-Sham equations. For NAOs, it uses exact diagonalization or the low-scaling method PEXSI. ABACUS applies different mixing algorithms for various types of calculations, including non-magnetic, collinear, and non-collinear. Additionally, ABACUS handles density matrix mixing for DFT+U, hybrid functionals, and DeePKS calculations with the NAOs basis.

We tested two preconditioner methods over 50 different cases. As depicted in Fig. 4, the modified Kerker preconditioner reduces the number of convergence steps considerably in most instances, as compared to its traditional preconditioner[71]. The modified method proves more effective with lower α_ρ.

2. Charge Density Mixing

Compared with non-magnetic calculations, magnetic SCF often struggles to converge and sometimes may even converge to incorrect magnetic configurations. For the Broyden/Pulay mixing method, the residual vector R is formulated as a function of the charge ρ and magnetization densities m as

$$R(\rho, m) = R(\rho_\uparrow + \rho_\downarrow, \rho_\uparrow - \rho_\downarrow). \quad (16)$$

ABACUS v3.5 starts to utilize the mixing (Eq. 17) that leverages the improved residual definition shown in Eq. 16. It is demonstrated in Fig. 5 that using Eq.16 for defining residuals leads to notably better results compared to using the direct charge density $R(\rho_\uparrow, \rho_\downarrow)$. The $(i+1)$-th input density can be

given by

$$\rho_{in}^{i+1} = \sum_{j=i-n}^{i} p_j \left[\rho_{in}^j + \alpha_\rho \frac{q^2}{q^2 + q_\rho^2} \left(\rho_{out}^j - \rho_{in}^j \right) \right],$$

$$m_{in}^{i+1} = \sum_{j=i-n}^{i} p_j \left[m_{in}^j + \alpha_m \frac{q^2}{q^2 + q_m^2} \left(m_{out}^j - m_{in}^j \right) \right], \quad (17)$$

here n is the number of historical charge densities considered. p_j is the coefficient calculated by the Pulay/Broyden method, and $\alpha_\rho \frac{q^2}{q^2 + q_\rho^2}$ actually represent the modified Kerker preconditioner mentioned in Sec.III B 1. ABACUS considers the preconditioning and mixing parameters for the magnetic density (q_ρ, q_m) separately from those for the charge density (α_ρ, α_m). By default, ABACUS only applies a preconditioner to the charge density, not the magnetic density $(q_m = 0)$. Users can enable preconditioning for the magnetic density by setting a non-zero value for q_m through the `mixing_mag_gg0` keyword. Fig. 5 (a) compares the performance of collinear magnetic calculations in practice among different versions of ABACUS.

ABACUS extends the collinear mixing method mentioned in Sec.III B 2 to non-collinear calculations by defining a more
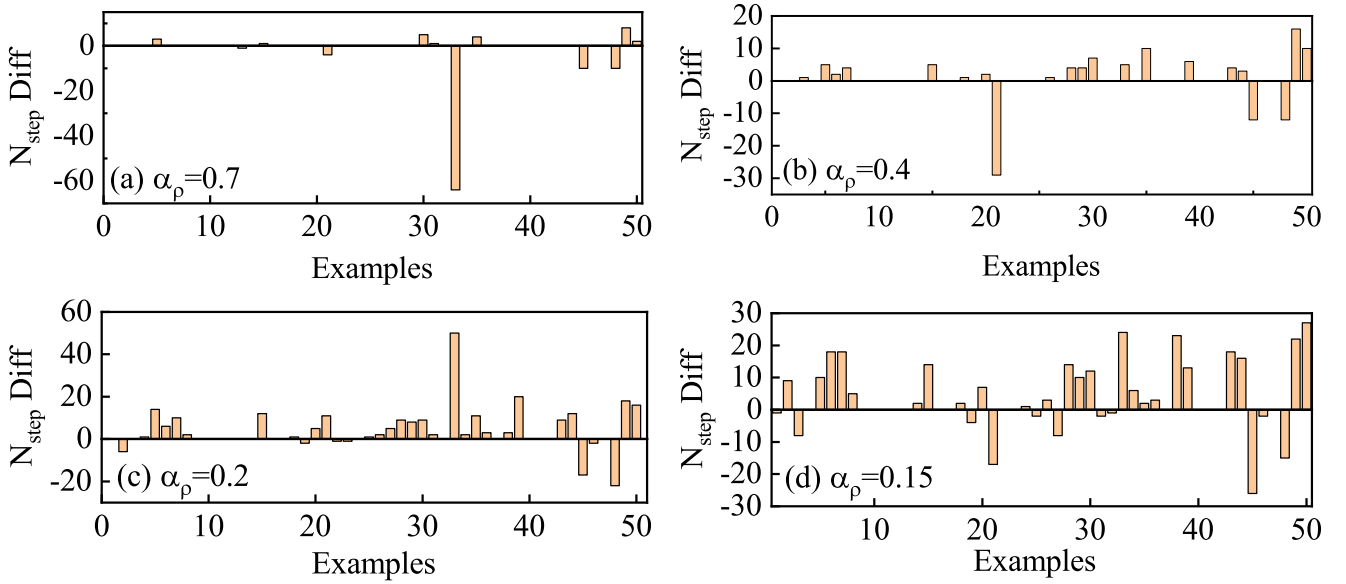
FIG. 4: For various α_ρ in Eq. 15, the difference in convergence steps (N_{step}) between ABACUS version v3.4 (the original Kerker preconditioner) and v3.5 (the modified Kerker preconditioner) when performing SCF calculations on the selection set of 50 examples which contain metals and semimetals. A positive value indicates that version 3.5 requires fewer convergence steps, and vice versa. The modified Kerker preconditioner shows a much better SCF performance than the original one. For the sake of reproduction, we have made public all the details of the calculations in the link[71], where one can find the complete report and download all input files. Index 1-8 cases are Si_{16}, Si_{32}, Cu_4, $Bi_2Se_2Cu_2O_2$, Ge_4As_8, H_2O, C_2H_6O, $H_{64}O_{32}$ for PW calculations; Index 9-16 cases are Si_{16}, Si_{32}, Si_{64}, Si_{128}, Cu_4, $Bi_2Se_2Cu_2O_2$, Ge_4As_8, H_2O for LCAO calculations. These 16 examples can be found in the subfolder of source code "`abacus-develop/example`". Index 17-50 cases are collected from the Issues posted by the users: $I_3Pb_1CN_2H_5$, $I_{12}Pb_4C_4N_8H_20$, $Li_{88}Ge_{20}$, $C_{60}H_{80}O_{60}$, $Li_{128}C_{75}H_{100}O_{75}$, $As_4Ca_4Mg_2$, Ti_{15}, $Al_{12}Hf_1Mg_{16}$, Au_1Mg_{63}, $Cs_1Pb_8I_{24}C_7N_{14}H_{35}$, GaAs (Zinc-Blend), C_2H_6O, MoS_2 (2×2), Pt-(111), $Ba_3Ti_3O_9$, Na_{16}, BCC-Fe ($3\times3\times3$), 64 H_2O, $Li_{27}Ni_9O_{54}Mn_9Co_9$, Si_{216}, $Na_9Fe_9O_{54}Ni_9Mn_9$, $Fe_9O_{54}Ni_9Mn_9$, LiNiOMnCo, $Fe_{14}H_4Mn_2C_1$, $Fe_{14}H_5Mn_2$, $Fe_{14}H_3Mn_2C_1B_1$, $MnBiTe_1$, $MnBiTe_2$, $Mg_{140}Zn_{12}Y_{16}$, Ti_5W_5, $Al_2Ga_1Sc_1$, $Li_{128}C_{75}O_{75}H_{100}$, $Cu_{12}Zn_8Ge_4S_{24}H_8$, $Si_{96}O_{32}H_{32}Hf_1Cl_4$.

general residual R as a function of four vectors:

$$R = R(\rho, \boldsymbol{m}_x, \boldsymbol{m}_y, \boldsymbol{m}_z), \qquad (18)$$

where $\boldsymbol{m}_x$ is the component of magnetic density $\boldsymbol{m} = \rho_\uparrow - \rho_\downarrow$ in the x-direction.

If one is not interested in the energies of a given magnetic configuration but wants to determine the ground state by relaxing the magnetic moments' directions, the standard Broyden mixing algorithm defined by Eqs. 17 and 18 sometimes fails to find the lowest magnetic configuration. ABACUS implements a promising angle mixing method proposed by Ref. 73, where the residual R is defined as a function of two-dimensional vector $\boldsymbol{n}$

$$R(\boldsymbol{n}) = R(\rho, |\boldsymbol{m}|), \qquad (19)$$

where $|\boldsymbol{m}_{in}^i| - |\boldsymbol{m}_{out}^i|$ contributes to the residual vector. At i-th iteration, and for each real-space point, θ_{out}^i is determined by the angle between $\boldsymbol{m}_{in}^i$ and $\boldsymbol{m}_{out}^i$. The next input $\boldsymbol{m}_{in}^{i+1}$ can be generated by following rules: i) keep $|\boldsymbol{m}_{out}^i|$ unchanged, namely $|\boldsymbol{m}_{in}^{i+1}| = |\boldsymbol{m}_{out}^i|$; ii) set the angle between $\boldsymbol{m}_{in}^{i+1}$ and $\boldsymbol{m}_{in}^i$ as $\theta_{in}^{i+1} = \beta\theta_{out}^i$; iii) the new input magnetization lies in the plane spanned by $\boldsymbol{m}_{in}^i$ and $\boldsymbol{m}_{out}^i$.

Traditional SCF iterations mix the charge density without involving the density matrix. However, the DFT+U

method[74–78] relies on the density matrix to construct the operators, leading to the discrepancy between the density matrix and the charge density, especially far from the ground state. This complicates the convergence process. ABACUS adopts a restart mixing method, which enables the density matrix to be mixed. Based on that, an automatic workflow named the U-Ramping method is realized, where ABACUS increases the U parameter step by step.

Owing to the initial charge density being estimated from atomic wavefunctions or other methods, it is not straightforward to make an analogous assumption for the density matrix. At the very beginning, SCF iterations mix only the charge density. Once a predefined threshold for convergence is achieved, the SCF calculations restart and enable the simultaneous mixing of the density matrix and charge density thereafter. This method has been shown to markedly advance the convergence rate of DFT+U simulations (see Fig. 5 (b)). For cases that are hard to converge, the U-Ramping method may prove beneficial[79,80]. ABACUS begins with an LDA/PBE calculation that excludes the U term, incorporating it incrementally only after surpassing a specified convergence level, and continues to periodically restart SCF computations until convergent with the complete U value.

Notably, this restart mixing method also enhances the con-

vergence efficiency of other approaches that depend on density matrices, such as hybrid functional method (see Sec. V E), and AI-assisted functional method DeePKS (see Sec. V F).

3. Smearing Methods

In metallic systems or semiconductors with small band gaps, the order of filled and empty states around the Fermi level may alternate during SCF calculations. This can cause charge density oscillations and lead to a lack of convergence. The smearing method helps speed up SCF convergence for such scenarios by permitting partial occupation of Kohn-Sham orbitals close to the Fermi energy.

For systems with narrow band gaps, a Gaussian distribution function can approximate the electrons' occupancy:

$$f(\varepsilon) = \frac{1}{\sigma\sqrt{2\pi}} e^{\frac{(\varepsilon - E_\mathrm{F})^2}{2\sigma^2}}, \tag{20}$$

where E_F represents the Fermi energy, and σ characterizes the extent of Gaussian broadening.

One can achieve a more accurate depiction of energy levels around the Fermi surface using the Methfessel-Paxton approach. Higher-order Methfessel-Paxton expansions[83] can yield better ground-state convergence results, speeding up the convergence. The Methfessel-Paxton distribution function takes the following form:

$$S_0(x) = \frac{1}{2}(1 - \mathrm{erf}(x)),$$
$$S_N(x) = S_0(x) + \sum_{n=1}^{N} A_n H_{2n-1}(x)e^{-x^2}, \tag{21}$$

where $x = \frac{\varepsilon - E_\mathrm{F}}{\sigma}$, $\mathrm{erf}(x)$ represents the error function. H_n is the N-th Hermite polynomial with the expansion coefficient A_n. The Methfessel-Paxton method is notably suggested for metals.

The Fermi-Dirac smearing can be described by the well-known Fermi-Dirac distribution:

$$f(\varepsilon) = 1/\{1 + \exp[(\varepsilon - E_\mathrm{F})/k_B T]\}, \tag{22}$$

where T is electron temperature, k_B is Boltzmann's constant.

In ABACUS, four distinct smearing methods are offered: Gaussian, Methfessel-Paxton (MP), Marzari-Vanderbilt (MV), and the Fermi-Dirac method.

C. Geometry Relaxation

During the ionic relaxation procedure with fixed lattice, the optimal ionic positions that minimize the total energy are found when the residual ionic forces smaller than a given threshold. The forces of atom τ is defined as

$$\mathbf{F}_\tau = -\partial E/\mathbf{R}_\tau. \tag{23}$$

The above optimization problem can be addressed via various algorithms, including the steepest descent (SD) algorithm, the conjugate gradient (CG) algorithm, the Broyden-Fletcher-Goldfarb-Shanno (BFGS) algorithm, and the Fast Inertial Relaxation Engine (FIRE) method[84]. During the optimization process, the optimization direction $\mathbf{D}_\tau$ for atom τ as well as the optimization step length α are determined, and the ionic positions are then updated iteratively

$$\mathbf{R}_\tau^{n+1} = \mathbf{R}_\tau^n + \alpha\mathbf{D}_\tau^n, \tag{24}$$

where n denotes the iteration number of the ionic step. This iterative procedure continues until the ionic positions reach a stable configuration, signifying the attainment of a local energy minimum.

Cell relaxation follows a two-step process. First, while lattice vectors are held constants, ionic positions are optimized through relaxation. Next, with fixed ionic positions, lattice vectors are optimized. During this stage, the stress tensor $\sigma_{\alpha\beta}$ is calculated, which takes the form of

$$\sigma_{\alpha\beta} = -\frac{1}{\Omega}\frac{\partial E}{\partial \varepsilon_{\alpha\beta}}, \tag{25}$$

where Ω is the volume of the cell. $\varepsilon_{\alpha\beta}$ represents strain with spatial coordinates α and β. The CG algorithm updates the lattice vectors based on the computed stress tensor, leading to an optimized unit cell. This iterative method continues until the system approaches a minimum energy state with stability in both the lattice vectors and ionic positions.

In addition, ABACUS allows users to specify certain ions to remain fixed during geometry relaxation, ensuring that only the positions of selected ions are optimized. It can also maintain the shape of simulation cell with fixed volume or modify volume while preserving the shape. Taking advantage of the numerical atomic orbital basis sets, ABACUS is capable of performing geometry relaxation calculations for large systems such as alloys[85], interfaces[86], slabs[87], low-dimensional materials[88,89], and more.

D. Molecular Dynamics

Molecular dynamics (MD) is widely used to analyze and predict the motions of molecules and atoms over time and serves as a powerful tool to study phase transition, diffusion, chemical reaction, and various properties of matter. In molecular dynamics, the motion of atoms is described by Newton's equations:

$$M_I\ddot{\mathbf{R}}_I = \mathbf{F}_I = -\frac{\partial E}{\partial \mathbf{R}_I}, \tag{26}$$

where M_I is the effective mass. Different molecular dynamics methods primarily differ in the way to calculate the atomic forces $\mathbf{F}_I$. Among them, ABACUS offers Lennard-Jones[90,91] classical MD, Born-Oppenheimer MD and Deep Potential molecular dynamics (DeePMD)[35,92]. The latter two are outlined below.

Born-Oppenheimer molecular dynamics (BOMD) is a type of ab initio MD where forces on atoms are calculated using
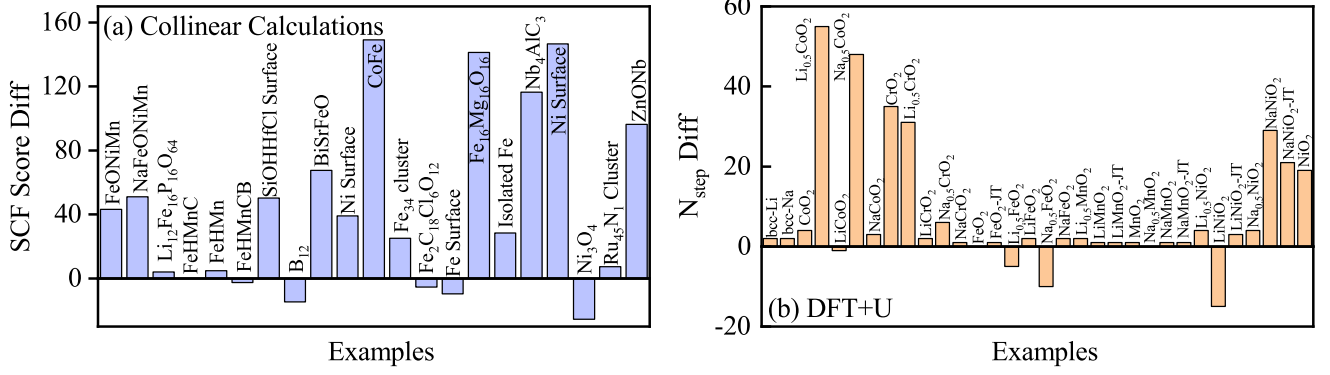
FIG. 5: (a) the difference in SCF performance between two mixing methods when performing SCF calculations on the selection set of 21 examples. Prior to v3.4, the residual was defined by $\rho_\uparrow$ and $\rho_\downarrow$, whereas starting from v3.5, the residual is defined by the charge density and the magnetic density, and they are mixed separately. Since some test cases failed to converge in v3.4, we present results with convergence scores rather than directly using convergence steps. The max number of iterations is set to 100 in all calculations, and the SCF convergence threshold `scf_thr=1e-6`. The SCF score is defined by $|\log_{10}(\delta\rho_{\text{last}})| \times 10 \times \frac{100}{N_{\text{step}}}$, where $\delta\rho_{\text{last}}$ is the density difference $R(\rho_{in})$ of the last iteration and N_{step} is the number of convergence iterations. (b) the difference in SCF convergence step (N_{step}) for the DFT+U calculation with only mixing charge density (RHO) and both mixing charge density and density matrix (RHO&DM). Here, "JT" represents a structure under Jahn–Teller distortion[81]. For the sake of reproduction, we have made public all the details of the calculations in the link[82], where one can find the complete report and download all input files.

quantum mechanical methods. Specifically, the atomic force is given by Eq. 37 in PW basis, and described by Eq. 98 in NAOs basis. BOMD is highly accurate because explicit electronic structure calculation is performed at each step. This allows for larger time steps and makes it suitable for longer simulations in real time. However, it is computationally demanding due to frequent electronic structure calculations. In ABACUS, we offer multiple ensembles and simulation methods, such as NVE ensemble with velocity Verlet algorithm[93], NVT ensemble[94], Nose-Hoover NPT ensemble[95–97], the Langevin thermostat[98]. In addition, the multi-scale shock technique (MSST) is integrated to simulate a compressive shock wave passing through the system. This method allows for molecular dynamics simulations of the system under dynamic shock conditions for significantly more extended time periods than NEMD.

BOMD simulations implemented in ABACUS have been used in various applications.[99–104] In 2017, Liu *et al.*[100] employed BOMD simulations to forecast the diffusion coefficients of deuterium in the liquid tin over a temperature range of 573 to 1673 K. Fig. 6(a) shows the diffusion coefficients of deuterium in a liquid tin cell consisting of 216 atoms at five temperatures between 573 and 1673 K. These simulations reveal that deuterium diffuses through liquid tin more rapidly than tin atoms diffuse within themselves. Fig. 6(b) depicts the effects of deuterium concentration on the diffusion rates of both deuterium and tin at 1073 K. The findings suggest that tin's structural and dynamic characteristics remain largely unaffected by the presence of deuterium for the tested temperatures and concentrations.

Wang *et al.*[105] studied the intercalation behavior of $AlCl_4$ molecule in graphite by employing BOMD. Fig. 7 illustrates the mean-square displacements (MSD) as simulated using
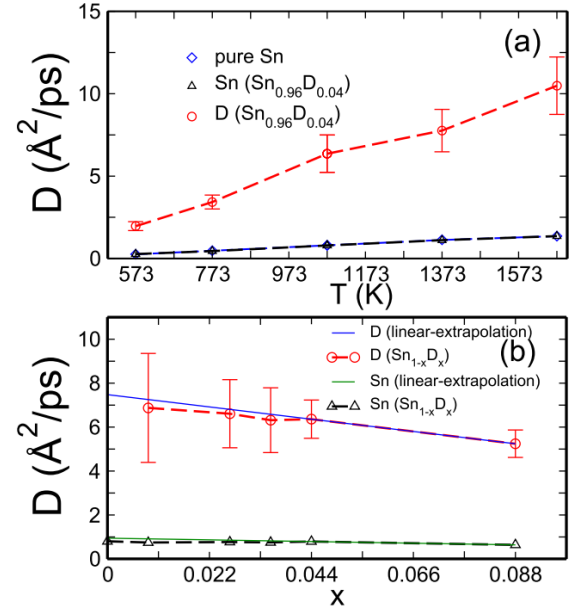
FIG. 6: (a) Diffusion coefficients of D in liquid $Sn_{0.96}D_{0.04}$, Sn in $Sn_{0.96}D_{0.04}$, and Sn in pure liquid Sn as a function of temperature. (b) Diffusion coefficients of D and Sn in liquid $Sn_{1-x}D_x$ at 1073 K with x being 0.009, 0.027, 0.036, 0.044, and 0.085. (Adapted with permission from J. Chem. Phys. 147, 064505 (2017). Copyright 2017 AIP Publishing.)

FHI-AIMS and ABACUS. The results exhibit rapid diffusion within the graphite layers, evident from the steep rises in their MSD. Additionally, the MSD trajectories for the Chlorine atoms feature periodic oscillations that are ascribed to

FIG. 7: Mean square displacement (MSD) as a function of molecular dynamics simulation time (in femtoseconds) for the three types of atom species in the stage-4 AlCl$_4$ graphite intercalation compound (GIC) u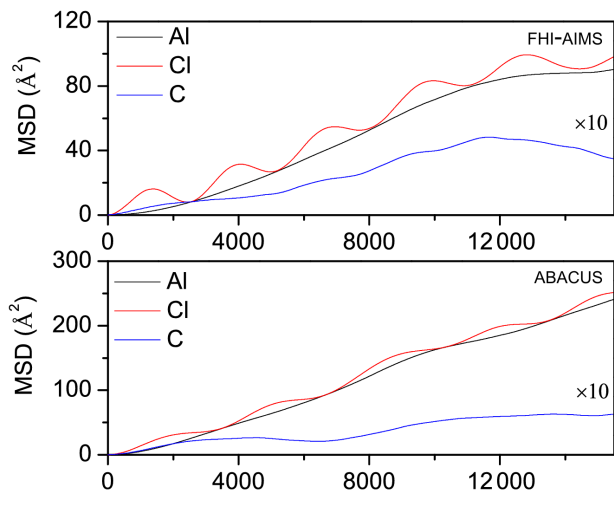sing ABACUS and FHI-AIMS packages. (Adapted with permission from Phys. Rev. Applied 12, 044060 (2019). Copyright 2019 American Physical Society.)

FIG. 8: Radial distribution functions (RDFs) $g(r)$ for B systems at a density of 2.46 g/cm^3 were analyzed at temperatures of (a) 86 eV and (b) 350 eV. The $g(r)$ derived using Ext-FPMD[106] The sDFT calculations employed the PBE[58] and corrKSDT[107] XC functionals. The number of B atoms is set to 32 in AIMD simulations. DPMD denotes the model trained by the traditional DP method[35], whereas DPMD-T indicates the TDDP method applied model training as reported by Zhang *et al.*[108]. N is the number of B atoms in a cell.(Adapted with permission from Matter. Radiat. Extremes 9, 015604 (2024). Copyright 2024 AIP Publishing.)

the rotational motion of these atoms around an axis orthogonal to the graphene layers during intercalation. This study revealed that AlCl$_4$ molecule retains its tetrahedral structure post-intercalation into graphite. Based on diffusion behavior, they suggest that an aluminum chloride graphene battery (AIB) with AlCl$_4$ could deliver a higher cathode specific capacity, elevated voltage, and improved rate capability.

Chen *et al.*[99] integrated stochastic density functional theory with BOMD to explore warm dense matter systems within a temperature range from several tens to 1000 eV. They also trained machine-learning-based interatomic models using the first-principles data and employed these models to examine large systems via extended simulations. Furthermore, they evaluated the structural and dynamic characteristics, as well as the transport coefficients, of warm dense matter. Fig. 8 shows the Radial distribution functions $g(r)$ of warm dense B with a density of 2.46 g/cm^3 at 86 and 350 eV, and the sDFT results are in excellent agreement with those obtained from Ext-FPMD. Ma *et al.*[109] combine AIMD and finite-temperature orbital-free DFT (FT-OFDFT) with a nonlocal free energy functional XWM to study a variety of warm dense matter systems including the Si, Al, H, He, and H-He mixtures. The KS-DFT calculations were performed using ABACUS, while the OF-DFT calculations were carried out with ATLAS[110]. The XWMF functional is expected to be a good choice for the realistic simulations of warm dense matter systems covering a broad range of temperatures and pressures.
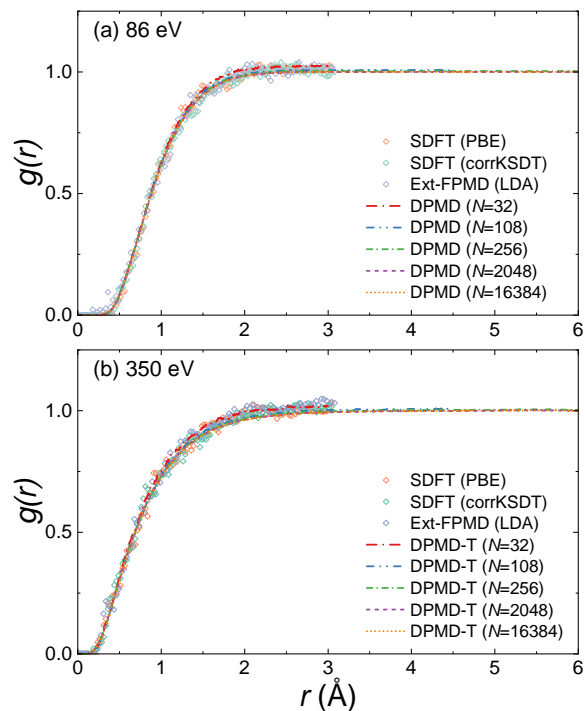
E. Implicit Solvation Model

Electrochemical reactions, which refer to potential-driven processes at electrode/solvent interfaces, are becoming essential for developing green-energy technologies used in producing clean fuels. Understanding electrochemical interfaces' structure and properties is crucial for designing and optimizing electrochemical systems. In this regard, atomic-scale computational simulations are pivotal in supporting the description of more complex electrochemical interfaces. However, theoretical modeling at the molecular level encounters significant challenges, such as addressing solvent layers, electrical double layers, and the variation of electron numbers at electrode/solvent surfaces, etc.

The implicit solvation model, together with the dipole correction and the compensating charge plate can achieve more realistic simulations of electrochemical reactions. These functions are integrated into the self-consistent field workflow of ABACUS, as illustrated in Fig. 9. After obtaining the initial electron density $\rho(\mathbf{r})$, several correction potential terms
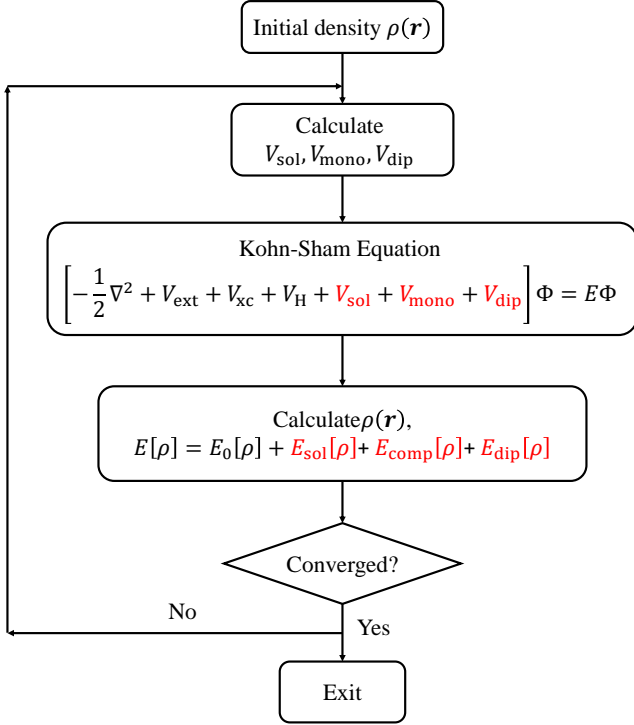
FIG. 9: Implementation of the implicit solvation model in ABACUS. The self consistent loop of solving the Kohn-Sham equation starts with an initial electron density $\rho(\mathbf{r})$. Then, the external potential V_{ext}, the Hartree potential V_H, and the exchange-correlation potential V_{XC} are constructed. In the solvation model, the Hamiltonian consists of three additional terms (highlighted by red color), which are the implicit solvation potential V_{sol}, the dipole correction term V_{dip}, and the compensating charge term V_{comp}. The corresponding energy corrections are also evaluated to yield the total energy $E[\rho]$. $E_0[\rho]$ denotes the system energy with no corrections.

are evaluated, including the potential of the implicit solvent V_{sol}, the compensating charge V_{comp}, and the dipole correction V_{dip}. These potential corrections are then applied to the Kohn-Sham equation, allowing computation of new electron density and the total energy.

Solid-liquid interfaces are ubiquitous and frequently encountered and employed in electrochemical simulations. For accurately modeling such systems, it is important to consider the solvation effect. The implicit solvation model is a well-developed method to deal with solvation effects, widely used in both finite and periodic systems. This approach treats the solvent as a continuous medium instead of individual "explicit" solvent molecules, which means that the solute embedded in an implicit solvent and the average over the solvent degrees of freedom becomes implicit in the properties of the solvent bath.

We place the solute in a cavity surrounded by a continuum dielectric medium characterized by the relative permittivity of the solvent, as employed in a previous work.[111]. We describe the dielectric response in terms of the solute's electron density, considering the polarization of solvents in response to the electronic structures of solute, the effects of cavitation and dispersion, and the reaction of solute system to the presence of the solvent.

We determine the form of the dielectric cavity in the solvent by assuming a diffuse cavity that is a local functional of the electron density $\rho(\mathbf{r})$ of the solute, which satisfies the following functional dependence

$$\varepsilon(\rho) = 1 + (\varepsilon_b - 1)S(\rho), \qquad (27)$$

where ε_b is the relative permittivity of the bulk solvent and $S(\rho)$ is the cavity shape function, given by[112]

$$S(\rho) = \frac{1}{2}\mathrm{erfc}\left(\frac{\ln\left(\frac{\rho}{\rho_c}\right)}{\sigma\sqrt{2}}\right). \qquad (28)$$

The parameter ρ_c is the charge density cutoff determining at what value of the electron density the dielectric cavity forms. σ determines the width of the diffuse cavity. This assumption leads to a smooth variation of the relative permittivity from $\varepsilon(\mathbf{r})=1$ of the solute to ε_b in the solvent.

The conjugate gradient method is used to solve the generalized Poisson equation

$$\nabla \cdot \left[\varepsilon(\rho)\nabla\phi\right] = -4\pi(N - \rho), \qquad (29)$$

where $\phi(\mathbf{r})$ is the electrostatic potential due to the electron density $\rho(\mathbf{r})$ and nuclear charge density $N(\mathbf{r})$ of the solute system in a polarizable medium.

The typical Kohn-Sham Hamiltonian consists of two additional terms in the local part of the potential. One of them is the electrostatic correction caused by the induced charge[111]

$$V_{el} = -\frac{d\varepsilon(\rho(\mathbf{r}))}{d\rho(\mathbf{r})}\frac{|\nabla\phi|^2}{8\pi}, \qquad (30)$$

and the other term is the cavity potential, which describes the cavitation, dispersion, and repulsion interaction between the solute and the solvent that is not captured by the electrostatic terms alone[111]

$$V_{cav} = \tau\frac{d|\nabla S|}{d\rho(\mathbf{r})}, \qquad (31)$$

where τ is the effective surface tension parameter. The two corrections (Eqs. 30 and 31) are collectively referred to as the implicit solvent-induced potential term V_{sol}. The energy correction terms is

$$E_{el} = -\frac{1}{8\pi}\int \varepsilon(\rho(\mathbf{r}))|\nabla\varphi|^2 d\mathbf{r} \qquad (32)$$

$$E_{cav} = \tau\int |\nabla S| d\mathbf{r}. \qquad (33)$$

We benchmark the accuracy of the implicit solvation implementation by calculating molecular solvation energies E_{sol},
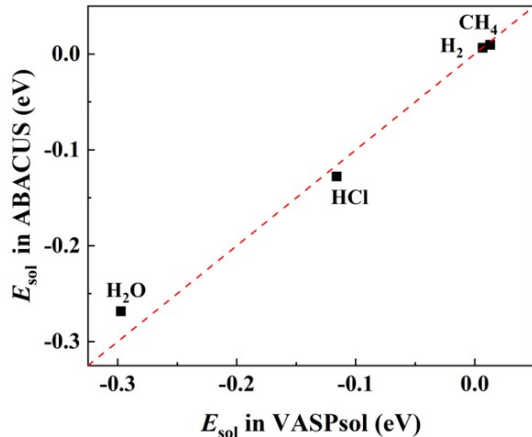
FIG. 10: Solvation energies (the total energy difference between a solvated condition and a vacuum condition) calculated by VASPsol and ABACUS for H_2O, HCl, H_2, and CH_4.

which is defined as the total energy differences between a solvated condition and a vacuum condition in ABACUS and comparing them against VASPsol-calculated values[113]. We can see from Fig.10 that the solvation energy results from ABACUS agree well with those produced by the VASPsol package. The minor discrepancies between the solvation energies computed by the two methods may be attributed to the pseudopotential difference. We use projector-augmented-wave (PAW) potentials in VASPsol and the norm-conserving pseudopotentials in ABACUS.

ABACUS also support to add dipole correction and compensating charge when modeling surfaces. The periodic boundary conditions imposed on the electrostatic potential create an artificial electric field across a slab. By introducing an isolated slab-shaped density distribution $\rho(\mathbf{r})$ that is normal to the z-axis, a dipole correction[114] is added to the bare ionic potential to compensate for the artificial dipole field within the context of periodic supercell calculations.

Modeling a constant-potential electrochemical surface reaction requires the adjustment of electron numbers in a simulation cell. Simultaneously, we must preserve the supercell's neutrality under the periodic boundary conditions. Thus, a distribution of compensating charge needs to be implemented in the vacuum region of surface models when extra electrons are added to or extracted from the system. The compensating charge implemented in ABACUS follows the methodology developed by Brumme *et al.* in 2014[115]. We assume that the monopole with a total charge of $-n_{\text{dop}}$ per unit cell is located at $z = z_{\text{mono}}$. In this case, the effective potential $V_{\text{mono}}(\mathbf{r})$ is added to the Hamiltonian, and the additional term E_{mono} is included in the total energy. Since $V_{\text{mono}}(\mathbf{r})$ is independent of the electronic density, it is unnecessary to update in a self-consistent manner. We derive the correction on the ionic forces induced by the presence of the monopole, allowing for calculating the electronic structure and complete structural re-
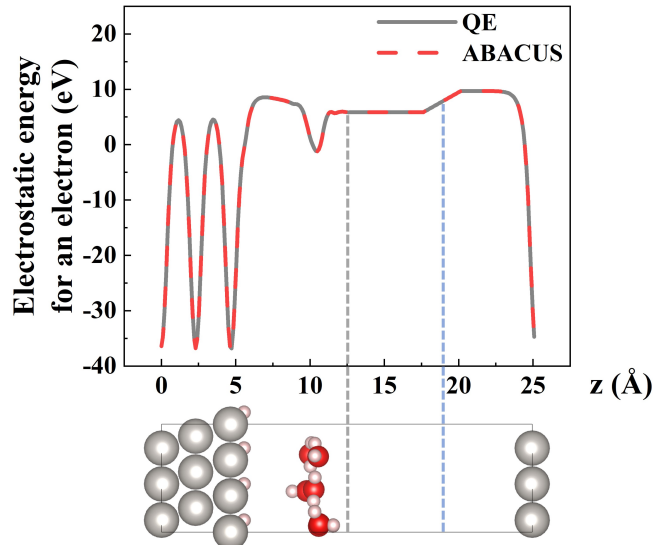

FIG. 11: Electrostatic energy of an electron along the direction (z) perpendicular to the Pt surface calculated by Quantum ESPRESSO and ABACUS[116]. The gray vertical dashed line represents the position of the compensating charge plate, and the blue dashed line corresponds to the dipole correction. A schematic structure plot of the testing interface model is aligned below the average electrostatic energy curves. Gray, red, and white spheres correspond to platinum, oxygen, and hydrogen atoms, respectively.

laxation in the field-effect configuration.

We output the electrostatic energy of an electron along the direction (z) perpendicular to the Pt surface for a testing system with an added electron number $N_e^{\text{extra}} = 0.2$ in the simulation cell. The testing system is a (3×3) Pt (111) surface slab composed of three atomic layers illustrated in Fig. 11. The modeled electrode surface contains 27 Pt atoms with one monolayer hydrogen coverage and six explicit water molecules. We place a compensating charge plate in the vacuum region above the water layer, and a dipole correction is also included in DFT calculations. We can see from Fig. 11 that the electrostatic energy results from ABACUS are in perfect agreement with those computed from Quantum ESPRESSO[11].

IV. METHODS IN PLANE WAVE BASIS

A. Kohn-Sham Equation in Plane Wave Basis

In the system with periodic boundary conditions, the electronic wave functions can be expanded on the basis of plane waves, which are written as

$$\psi_{n\mathbf{k}}(\mathbf{r}) = \sum_{\mathbf{G}} c_{n\mathbf{k}}(\mathbf{G}) e^{i(\mathbf{k}+\mathbf{G})\cdot\mathbf{r}}, \tag{34}$$

where $\mathbf{G}$ and $\mathbf{k}$ represent the wave vectors of plane waves and sampling points in the Brillouin zone, respectively, n denotes the band index, and $\{c_{n\mathbf{k}}(\mathbf{G})\}$ are the expansion coefficients of plane wave basis. The k-point sampling can be chosen such as the Monkhorst-Pack scheme[48].

The Kohn-Sham equation described with plane wave basis takes the form of

$$\sum_{\mathbf{G}'}\left[\frac{1}{2}(\mathbf{k}+\mathbf{G})^2\delta_{\mathbf{G}\mathbf{G}'}+\tilde{V}_{\mathrm{KS}}(\mathbf{G}-\mathbf{G}')\right]c_{n\mathbf{k}}(\mathbf{G}')=\varepsilon_{nk}c_{n\mathbf{k}}(\mathbf{G}),\tag{35}$$

where $\tilde{V}_{\mathrm{KS}}(\mathbf{G}-\mathbf{G}')$ is the plane wave represenation of the Kohn-Sham potential $\hat{V}_{\mathrm{KS}}$, ε_{nk} is the eigenvalue of the Kohn-Sham equation, and $\delta_{\mathbf{G}\mathbf{G}'}$ is the Kronecker delta function.

The total energy can be calculated as

$$E_{\mathrm{tot}}=\sum_{\mathbf{k}n}f(\varepsilon_{n\mathbf{k}})\varepsilon_{n\mathbf{k}}-\frac{1}{2}\int\int\frac{\rho(\mathbf{r})\rho(\mathbf{r}')}{|\mathbf{r}-\mathbf{r}'|}d\mathbf{r}d\mathbf{r}'$$
$$-\int v_{\mathrm{xc}}(\mathbf{r})\rho(\mathbf{r})d\mathbf{r}+E_{\mathrm{xc}}[\rho(\mathbf{r})]+E_{\mathrm{II}},\tag{36}$$

where $f(\varepsilon_{n\mathbf{k}})$ is the Fermi-Dirac distribution function, $\rho(\mathbf{r})$ is the electron density, v_{xc} is the exchange-correlation potential, E_{xc} is the exchange-correlation energy, and E_{II} is the ionic energy calculated by the Ewald method[47].

According to the Hellmann-Feynman theorem[117,118], the force acting on atom I is defined as Eq. 23 and the stress is defined as Eq. 25. Consequently, when including a non-local part in the norm-conserving pseudopotential, the force on atom I of type τ can be divided into three parts, namely

$$\mathbf{F}_{I\tau}=\mathbf{F}_{I\tau}^{\mathrm{Ewald}}+\mathbf{F}_{I\tau}^{\mathrm{L}}+\mathbf{F}_{I\tau}^{\mathrm{NL}},\tag{37}$$

where $\mathbf{F}_{I\tau}^{\mathrm{Ewald}}$ is the Ewald force. $\mathbf{F}_{I,\tau}^{\mathrm{L}}$ is the force contributed by the local part of the pseudopotential, and $\mathbf{F}_{I,\tau}^{\mathrm{NL}}$ is from the non-local part. The local potential term is given by

$$\mathbf{F}_{I\tau}^{\mathrm{L}}=-i\Omega\sum_{\mathbf{G}}\mathbf{G}e^{i\mathbf{G}\cdot\mathbf{R}_I}v_{\tau}^{\mathrm{L}}(\mathbf{G})\rho^*(\mathbf{G}),\tag{38}$$

where Ω is the cell volume and $\rho(\mathbf{G})$ is the electron density in the plane wave basis, which is computed as

$$\rho(\mathbf{G})=\frac{1}{\Omega}\int\rho(\mathbf{r})e^{-i\mathbf{G}\cdot\mathbf{r}}d\mathbf{r}.\tag{39}$$

The non-local potential term is written as

$$\mathbf{F}_{I,\tau}^{\mathrm{NL}}=-2i\sum_{\mathbf{k},n}W(\mathbf{k})\sum_{\mathbf{G},\mathbf{G}'}f(\varepsilon_n;\mu)c_{n\mathbf{k}}^*(\mathbf{G})c_{n\mathbf{k}}(\mathbf{G}')$$
$$\times\left[e^{i(\mathbf{G}'-\mathbf{G})\cdot\mathbf{R}_I}(\mathbf{G}'-\mathbf{G})v_{\tau}^{\mathrm{NL}}(\mathbf{k}+\mathbf{G},\mathbf{k}+\mathbf{G}')\right],\tag{40}$$

where v_{τ}^{L} is the local potential of atom type τ, $W(\mathbf{k})$ represents the weight of the k point (k).

The stress tensor is decomposed into Ewald term $\sigma_{\alpha\beta}^{\mathrm{Ewald}}$, Hartree term $\sigma_{\alpha\beta}^{\mathrm{H}}$, exchange-correlation term $\sigma_{\alpha\beta}^{\mathrm{xc}}$, kinetic energy term $\sigma_{\alpha\beta}^{\mathrm{T}}$, local pseudopotential term $\sigma_{\alpha\beta}^{\mathrm{L}}$, and non-local pseudopotential term $\sigma_{\alpha\beta}^{\mathrm{NL}}$, expressed as

$$\sigma_{\alpha\beta}=\sigma_{\alpha\beta}^{\mathrm{Ewald}}+\sigma_{\alpha\beta}^{\mathrm{Hartree}}+\sigma_{\alpha\beta}^{\mathrm{xc}}+\sigma_{\alpha\beta}^{\mathrm{T}}+\sigma_{\alpha\beta}^{\mathrm{L}}+\sigma_{\alpha\beta}^{\mathrm{NL}},\tag{41}$$

where

$$\sigma_{\alpha\beta}^{\mathrm{Hartree}}=-2\pi\sum_{\mathbf{G}\neq0}\frac{|\rho(\mathbf{G})|^2}{G^2}\left[2\frac{\mathbf{G}_{\alpha}\mathbf{G}_{\beta}}{G^2}-\delta_{\alpha\beta}\right],\tag{42}$$

$$\sigma_{\alpha\beta}^{\mathrm{xc}}=-\delta_{\alpha\beta}\sum_{\mathbf{G}}[\varepsilon_{\mathrm{xc}}(\mathbf{G})-v_{\mathrm{xc}}(\mathbf{G})]\rho^*(\mathbf{G}),\tag{43}$$

$$\sigma_{\alpha\beta}^{\mathrm{T}}=\frac{2}{\Omega}\sum_{\mathbf{k},n}W(\mathbf{k})\sum_{\mathbf{G},\mathbf{G}'}f(\varepsilon_n;\mu)$$
$$c_{n\mathbf{k}}^*(\mathbf{G})(\mathbf{k}+\mathbf{G})_{\alpha}\delta(\mathbf{G},\mathbf{G}')(\mathbf{k}+\mathbf{G}')_{\beta}c_{n\mathbf{k}}(\mathbf{G}'),\tag{44}$$

$$\sigma_{\alpha\beta}^{\mathrm{L}}=\sum_{\mathbf{G},\tau}S_{\tau}(\mathbf{G})\left[\frac{\partial v_{\tau}^{L}(\mathbf{G})}{\partial(G^2)}2\mathbf{G}_{\alpha}\mathbf{G}_{\beta}+v_{\tau}^{L}(\mathbf{G})\delta_{\alpha\beta}\right]\rho^*(\mathbf{G}),\tag{45}$$

and

$$\sigma_{\alpha\beta}^{\mathrm{NL}}=-\frac{2}{\Omega}\sum_{\mathbf{k}n}W(\mathbf{k})\sum_{\mathbf{G}\mathbf{G}'\tau}f(\varepsilon_n;\mu)c_{n\mathbf{k}}^*(\mathbf{G})c_{n\mathbf{k}}(\mathbf{G}')$$
$$\times S_{\tau}(\mathbf{G}'-\mathbf{G})\frac{\partial v_{\tau}^{\mathrm{NL}}(\mathbf{k}+\mathbf{G},\mathbf{k}+\mathbf{G}')}{\partial\varepsilon_{\alpha\beta}},\tag{46}$$

where the structure factor is

$$S_{\tau}(\mathbf{G})=\sum_{I\in\tau}e^{i\mathbf{G}\cdot\mathbf{R}_I}.\tag{47}$$

B. Iterative Diagonalization Methods

With the plane wave basis set, the KS equation is routinely solved using iterative diagonalization methods, such as Conjugate Gradient (CG) and Davidson (Dav) methods, because the basis number is typically large. In general, diagonalization of given Hamiltonian is the most time-consuming part in most KS-DFT calculations, so efficient methods with high-performance-computing devices are required.

Heterogeneous computing devices, such as graphics processing units (GPUs) and deep computing units (DCUs), have significantly advanced the computational capabilities of modern scientific applications, especially in computational chemistry and materials science[11,119,120]. The ABACUS software harnesses these advancements to enhance the efficiency and scalability of its plane-wave basis set calculations.

As an example, the CG's procedure is shown in detail in Fig. 12. The implementation fully leverages the heterogeneous framework of ABACUS, running the same code set across different devices through the abstraction layer. Operators like gemv and vecdiv are encapsulated under a unified interface for various platforms, including CPUs, GPUs, and DCUs. This allows the algorithm to enjoy cross-platform high performance without focusing on the underlying implementation details of these basic operations.

ABACUS utilizes a heterogeneous framework to execute diverse code efficiently. The framework consists of two primary components: Math Libraries and Kernel Operators.

```
for m = 0 to n do
    Ψ ← [ψ₀ … ψ_{m−1}]
    L ← Ψ^T ψ_m                                    gemv
    ψ_m ← ψ_m − ΨL
    HP ← Hψ_m                               FFT & Nonlocal
    λ ← ⟨ψ_m|H|ψ_m⟩                                 dot
    repeat
        g ← K(HP − λψ_m)                 vecdiv, dot, vecadd
        Ψ ← [ψ₀ … ψ_m]
        L ← Ψ^T g                                  gemv
        g ← g − ΨL
        d ← g + γ d_old                   dot, vecmul, vecadd
        h ← Hd                               FFT & Nonlocal
        ψ_m ← ψ_m cos θ + d sin θ               dot, vecadd
        HP ← HP cos θ + h sin θ                     vecadd
        λ ← ⟨ψ_m|H|ψ_m⟩                             dot
    until convergence
end for
```

FIG. 12: Preconditioned conjugate gradient algorithm in ABACUS. Here, ψ_i represents the current approximation of the eigenvector being updated, and λ denotes the corresponding eigenvalue, known as the Rayleigh quotient. To enhance computational efficiency, we employ a preconditioner K to approximate the inverse of the Hamiltonian matrix H. Adjacent to each step of the algorithm are the numerical kernels.

Math Libraries provide a unified interface for linear algebra calculations and fast Fourier transforms (FFT) across various accelerators. These libraries include CUDA-accelerated implementations like cuBLAS, cuSolver, and cuFFT; ROCm-accelerated implementations such as hipBLAS, hipSolver, and hipFFT; and CPU libraries like Intel Math Kernel Library. Kernel Operators serve as an abstraction layer that simplifies the execution of custom kernels and memory management across different heterogeneous frameworks, including NVIDIA CUDA, AMD ROCm, and Intel oneAPI. This abstraction enables ABACUS to write code independent of specific accelerators, eliminating redundant code for different processor types and enabling execution on CPUs. Consequently, this framework enhances code portability and fully leverages the strengths of various hardware architectures to improve computational performance. In summary, this framework allows us to write code once and execute it on multiple hardware platforms.

The allocation (explicit memory requests) and deallocation (release of memory) of GPU memory are time-consuming processes. Therefore, minimizing these operations in performance-critical sections of the code is crucial. A naive approach is extending the lifespan of variables or making them global, which can compromise the program's architecture. Instead, ABACUS introduces another abstraction layer by using custom memory allocators optimized for specific use patterns. These allocators recycle large memory chunks across different objects, avoiding the costly system-level memory release. According to our benchmarks, 90% of the execution time and memory usage occur on the accelerators during the SCF loop, with minimal control flow on the Host CPU.

Additionally, our PW GPU code supports fully single-precision calculations during the SCF loop, maximizing the use of common hardware. Single-precision calculations significantly reduce memory usage and computational load, making them particularly advantageous for large-scale simulations. This feature not only accelerates the SCF loop but also ensures compatibility with a broader range of GPUs, including those with limited double-precision capabilities. ABACUS achieves higher efficiency and performance by optimizing resource utilization and facilitating more extensive and detailed scientific computations.

To evaluate the efficiency of heterogeneous acceleration in ABACUS, we performed SCF calculations using plane-wave basis sets on diverse hardware platforms for systems with varying numbers of atoms. We compared CPU and DCU hardware from the Bohrium cloud platform[121] with roughly the same compute time cost for a relatively fair comparison. In Fig. 13, we choose the Davidson method since the Davidson method is generally faster than the Conjugate Gradient method. By analyzing the computation times for the different test cases, we discovered that the acceleration ratio achieved by the DCU computations increases as the number of atoms in the system rises. For instances with approximately 50 atoms, the acceleration ratio achieved on the DCU platform can be up to 5-fold, significantly reducing the computational cost.

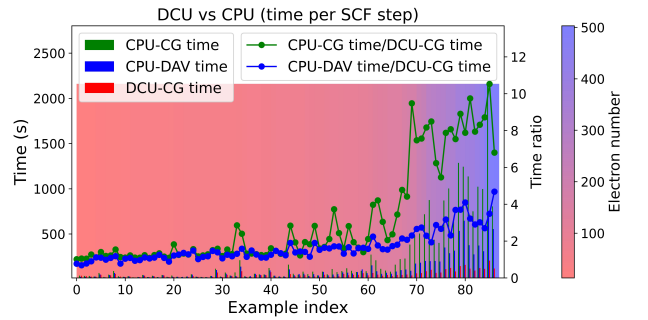FIG. 13: For a collection of examples with different numbers of atoms, the Bar charts represent the calculation time per iteration by using the CG method on DCU (Red), the Davison method on CPU (Blue), and the CG method on CPU (Green) respectively. The line chart shows their ratio. One can download the examples from the link[122]. We choose the hardware c32_m64 for CPU calculations and 4*DCU for DCU calculations.

C. Stochastic DFT

1. Formulas

The stochastic density functional theory (sDFT)[123] was proposed to circumvent the $O(N^3)$ scaling of KS-DFT calculations. In this method, by introducing stochastic orbitals and the Chebyshev expansion scheme, the electron density can be evaluated by tracing operators, bypassing the diagonalization of the Hamiltonian. Since the computational costs of tracing operations scale linearly with system size, this approach significantly enhances computational efficiency for large systems. Later, the finite-temperature sDFT[124] defines the Fermi-Dirac operator at finite temperature as

$$\hat{f}_H = \frac{1}{1 + \exp\left(\frac{\hat{H} - E_\mu}{k_B T}\right)}, \tag{48}$$

where $\hat{H}$ is the KS Hamiltonian operator and E_μ represents the chemical potential. In fact, the order of expansion decreases with increasing temperature, thereby enhancing the computational efficiency of sDFT at high temperatures.

However, the use of stochastic orbitals inevitably introduces stochastic errors. To achieve higher accuracy, a large number of stochastic orbitals are typically required, which substantially increases the computational time despite its linear scaling property. For instance, fragmentation approaches have been developed to compute molecular systems[125] and covalent materials[126,127], while stochastic "embedding" methods have been used to calculate p-nitroaniline in water[128]. Additionally, the energy window method proposed by Chen *et al.*[129] decomposes the electron density into different components based on orbital energies to reduce stochastic errors, demonstrating good generality and robustness. For simulations of materials at extremely high temperatures, mixed stochastic-deterministic Density Functional Theory (mDFT) was proposed[130]. The method combines the advantages of traditional KS-DFT and sDFT. The mDFT method retains the computational efficiency of sDFT for high-temperature systems while reducing stochastic errors using some of the deterministic Kohn-Sham orbitals.

In sDFT, the electron density is directly computed using the Hamiltonian operator as

$$\begin{aligned} \rho(\mathbf{r}) &= 2\mathrm{Tr}\left[\hat{f}_H \delta(\hat{\mathbf{r}} - \mathbf{r})\right] \\ &= 2\mathrm{Tr}\left[\hat{f}_H |\mathbf{r}\rangle\langle\mathbf{r}|\right] \\ &= 2\mathrm{Tr}\left[\hat{f}_H^{1/2} |\mathbf{r}\rangle\langle\mathbf{r}| \hat{f}_H^{1/2}\right], \end{aligned} \tag{49}$$

where the chemical potential μ in $\hat{f}_H$ is determined by solving the conservation of electron number via

$$N = \mathrm{Tr}\left[\hat{f}_{H\mu}\right]. \tag{50}$$

By adopting the self-consistent field method, the electron density can be self-consistently computed. The total energy can similarly be computed via

$$\begin{aligned} E_{\mathrm{tot}} =& 2\mathrm{Tr}\left[\hat{f}_H \hat{H}\right] - \frac{1}{2}\iint \frac{\rho(\mathbf{r})\rho(\mathbf{r}')}{|\mathbf{r} - \mathbf{r}'|} \mathrm{d}\mathbf{r}\mathrm{d}\mathbf{r}' \\ & - \int v_{\mathrm{xc}}(\mathbf{r})\rho(\mathbf{r})\mathrm{d}\mathbf{r} + E_{\mathrm{xc}}[\rho(\mathbf{r})] + E_{\mathrm{II}}. \end{aligned} \tag{51}$$

2. Stochastic Orbitals

In detail, the sDFT defines a set of stochastic orbitals. For any orthogonal complete basis $\{\phi_j\}$, the stochastic orbitals $\{\chi_a\}$ are defined as

$$\langle\phi_j|\chi_a\rangle = \frac{1}{\sqrt{N_\chi}}\exp\left(i2\pi\theta_j^a\right), \tag{52}$$

where $\{\theta_j^a\}$ are stochastic numbers uniformly distributed over $(0,1)$, and N_χ is the number of stochastic orbitals. In addition, stochastic orbitals can also be defined[127,129,131,132] as

$$\langle\phi_j|\chi_a\rangle = \pm\frac{1}{\sqrt{N_\chi}}, \tag{53}$$

each with a probability of 1/2. Notably, Baer *et al.*[133] demonstrated that both definitions yield the same expected values and similar variance for Hermitian matrices with comparable magnitudes of real and imaginary parts. As $N_\chi \to +\infty$, the stochastic orbitals form a complete basis with the relation of

$$\lim_{N_\chi \to +\infty} \sum_{a=1}^{N_\chi} \langle\phi_i|\chi_a\rangle\langle\chi_a|\phi_j\rangle = \delta_{ij}, \tag{54}$$

and

$$\lim_{N_\chi \to +\infty} \sum_{a=1}^{N_\chi} |\chi_a\rangle\langle\chi_a| = \hat{I}. \tag{55}$$

To enhance the accuracy of stochastic orbitals, mDFT introduces a set of deterministic, orthogonal but not complete Kohn-Sham orbitals φ_i, along with stochastic orbitals $\tilde{\chi}_a$, where the stochastic orbitals are required to be orthogonal to the deterministic ones

$$|\tilde{\chi}_a\rangle = |\chi_a\rangle - \sum_{i=1}^{N_\varphi} \langle\varphi_i|\chi_a\rangle |\varphi_i\rangle, \tag{56}$$

where N_φ is the number of deterministic orbitals. The mixed orbitals composed of deterministic and orthogonal stochastic orbitals also form a complete basis set as

$$\lim_{N_\chi \to +\infty} \sum_{a=1}^{N_\chi} |\tilde{\chi}_a\rangle\langle\tilde{\chi}_a| + \sum_{i=1}^{N_\varphi} |\varphi_i\rangle\langle\varphi_i| = \hat{I}. \tag{57}$$

Therefore, the trace of any operator $\hat{O}$ is given by

$$\mathrm{Tr}\left[\hat{O}\right] = \lim_{N_\chi \to +\infty} \sum_{a=1}^{N_\chi} \langle\tilde{\chi}_a|\hat{O}|\tilde{\chi}_a\rangle + \sum_{i=1}^{N_\varphi} \langle\varphi_i|\hat{O}|\varphi_i\rangle. \tag{58}$$
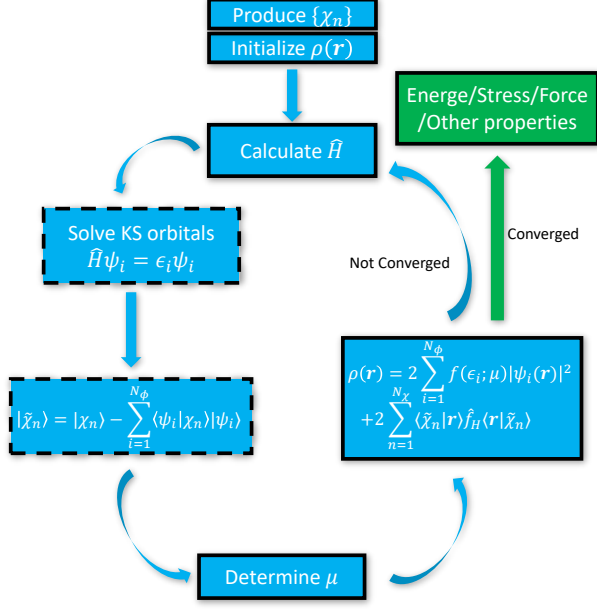
The stochastic orbitals based on the plane-wave basis can be defined as

$$|\chi_{a\mathbf{k}}\rangle = \frac{1}{\sqrt{N_\chi}} \sum_{\mathbf{G}} \exp\left(i2\pi\theta_{\mathbf{k},\mathbf{G}}^a\right) |\mathbf{k}+\mathbf{G}\rangle, \qquad (60)$$

where $\theta_{\mathbf{k},\mathbf{G}}^a$ are independent stochastic numbers uniformly distributed in $(0,1)$, and N_χ is the number of stochastic orbitals. Besides the sum of stochastic orbitals, the sum of $\mathbf{k}$-point should also be done. In plane-wave-based sDFT, the electron density can be computed as

$$\rho(\mathbf{r}) = 2\sum_{\mathbf{k}} W(\mathbf{k}) \sum_{a,\mathbf{G}} \left| \langle\mathbf{r}|\mathbf{k}+\mathbf{G}\rangle \left\langle \mathbf{k}+\mathbf{G} \left| \hat{f}_H^{1/2} \right| \chi_{a\mathbf{k}} \right\rangle \right|^2. \quad (61)$$

If we define

$$\gamma_{a\mathbf{k}}(\mathbf{G}) = \left\langle \mathbf{k}+\mathbf{G} \left| \hat{f}_H^{1/2} \right| \chi_{a\mathbf{k}} \right\rangle, \qquad (62)$$

the electron density can be written as

$$\rho(\mathbf{r}) = 2\sum_{\mathbf{k}} W(\mathbf{k}) \sum_{a\mathbf{G}} \left| \gamma_{a\mathbf{k}}(\mathbf{G}) e^{i(\mathbf{k}+\mathbf{G})\cdot\mathbf{r}} \right|^2. \qquad (63)$$

For the force, only the nonlocal potential part is different from the traditional Kohn-Sham method, which is given by

$$
\begin{aligned}
\mathbf{F}_{I,\tau}^{\mathrm{NL}} =\ & 2\mathrm{Tr}\Big[-i\hat{f}_H \sum_{\mathbf{GG'}} (\mathbf{G'}-\mathbf{G}) e^{i(\mathbf{G'}-\mathbf{G})\cdot\mathbf{R}_I} \\
& v_\tau^{\mathrm{NL}}(\mathbf{k}+\mathbf{G},\mathbf{k}+\mathbf{G'})|\mathbf{k}+\mathbf{G}\rangle\langle\mathbf{k}+\mathbf{G'}| \Big] \\
=\ & -2i\sum_{\mathbf{k}} W(\mathbf{k}) \sum_{a\mathbf{G},\mathbf{G'}} \gamma_{a\mathbf{k}}(\mathbf{G})\gamma_{a\mathbf{k}}(\mathbf{G'}) \\
& \times (\mathbf{G'}-\mathbf{G}) e^{i(\mathbf{G'}-\mathbf{G})\cdot\mathbf{R}_I} v_\tau^{\mathrm{NL}}(\mathbf{k}+\mathbf{G},\mathbf{k}+\mathbf{G'}).
\end{aligned}
\qquad (64)
$$

Additionally, the stress tensor for the kinetic part and the nonlocal part are evaluated differently in sDFT and mDFT when compared to the traditinoal Kohn-Sham method. Specifically, the kinetic part is given by

$$
\begin{aligned}
\sigma_{\alpha\beta}^T =\ & \frac{2}{\Omega}\mathrm{Tr}\Big[\hat{f}_H \sum_{\mathbf{GG'}} (\mathbf{k}+\mathbf{G})_\alpha(\mathbf{k}+\mathbf{G'})_\beta|\mathbf{k}+\mathbf{G}\rangle\delta(\mathbf{GG'})\langle\mathbf{k}+\mathbf{G'}| \Big] \\
=\ & \frac{2}{\Omega}\sum_{\mathbf{k}} W(\mathbf{k}) \sum_{a,\mathbf{GG'}} \gamma_{a\mathbf{k}}(\mathbf{G})(\mathbf{k}+\mathbf{G})_\alpha\delta(\mathbf{GG'})(\mathbf{k}+\mathbf{G'})_\beta\gamma_{a\mathbf{k}}(\mathbf{G'}),
\end{aligned}
\qquad (65)
$$

and the nonlocal part is given by

FIG. 14: Flowchart of mDFT and sDFT in ABACUS. When the number of KS orbitals N_ϕ is larger than 0, it is the flowchart of mDFT. When the number of KS orbitals N_ϕ reduces to 0, indicating that the dashed box does not exist, it degenerates into the flowchart of sDFT.

For example, in mDFT, the formula for electron density is

$$\rho(\mathbf{r}) \approx 2\sum_{a=1}^{N_\chi} \left| \left\langle \tilde{\chi}_a \left| \hat{f}_H^{1/2} \right| \mathbf{r} \right\rangle \right|^2 + 2\sum_{i=1}^{N_\varphi} f(\varepsilon_i)|\psi_i(\mathbf{r})|^2. \quad (59)$$

Note that here we use a finite number of stochastic orbitals N_χ, which introduces stochastic errors.

3. Plane-Wave-Based Implementation

We have implemented sDFT and mDFT methods based on plane wave basis[134] and periodic boundary conditions in ABACUS. Furthermore, both methods can be use with the k-point sampling method. The flowchart of sDFT and mDFT is shown in Fig. 14.

$$
\begin{aligned}
\sigma_{\alpha\beta}^{\mathrm{NL}} =\ & -\frac{2}{\Omega}\mathrm{Tr}\Big[\hat{f}_H \sum_{\mathbf{GG'}\tau} S_\tau(\mathbf{G'}-\mathbf{G})\frac{\partial v_\tau^{\mathrm{NL}}(\mathbf{G}+\mathbf{k},\mathbf{G'}+\mathbf{k})}{\partial\varepsilon_{\alpha\beta}}|\mathbf{k}+\mathbf{G}\rangle\langle\mathbf{k}+\mathbf{G'}| \Big] \\
=\ & -\frac{2}{\Omega}\sum_{a\mathbf{GG'},\tau} \gamma_{a\mathbf{k}}(\mathbf{G}) S_\tau(\mathbf{G'}-\mathbf{G})\frac{\partial v_\tau^{\mathrm{NL}}(\mathbf{G}+\mathbf{k},\mathbf{G'}+\mathbf{k})}{\partial\varepsilon_{\alpha\beta}}\gamma_{a\mathbf{k}}(\mathbf{G'}).
\end{aligned}
\qquad (66)
$$

Fig. 15(a) shows the parallel efficiency of sDFT and mDFT. sDFT demonstrates excellent scalability as all stochas-
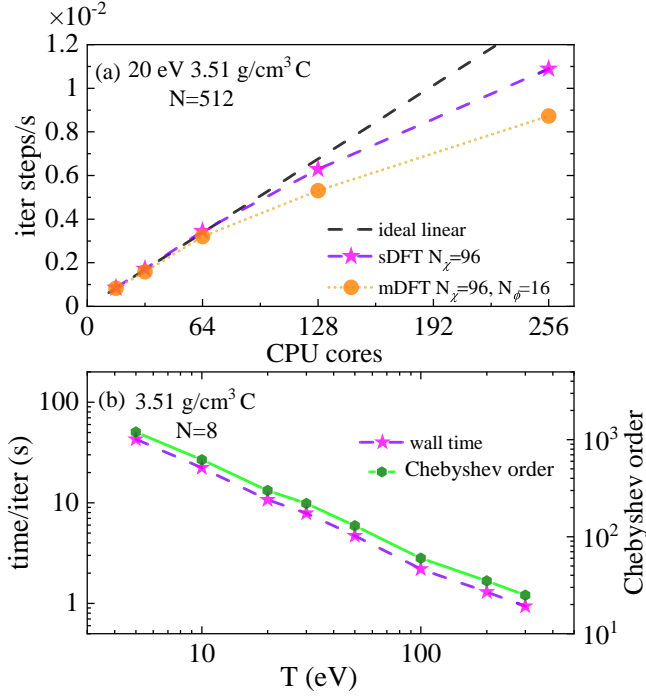
FIG. 15: Efficiency tests of the sDFT and mDFT methods. (a) Parallel efficiency of sDFT and mDFT for a C system (N=512) at the temperature of 20 eV. (b) Averaged wall time for an electronic iteration step of the sDFT method when calculating a C system (N=8) at a temperature range of 5-300 eV. All CPU cores are in Intel(R) Xeon(R) Platinum 9242 CPU @ 2.30GHz nodes.

tic orbitals are independently evaluated, while mDFT involves calculating KS orbitals and additional data communication among CPU cores, reducing its efficiency compared to sDFT. Fig. 15(b) compares the operational efficiency at different temperatures by recording the average time per electronic iteration for the sDFT method. The temperature ranges from 5 to 300 eV, and 96 stochastic orbitals was adopted. In sDFT, the order of Chebyshev polynomial expansions was selected to ensure an electron error less than 1e-9. Specifically, for temperatures of 5, 10, 20, 30, 50, 100, 200, and 300 eV, Chebyshev orders of 1200, 620, 300, 220, 130, 60, 35, and 25 were used, respectively. As the temperature increases, the number of Chebyshev orders decreases, causing the wall time to drop exponentially. The sDFT and mDFT methods implemented in ABACUS has been successfully applied to study warm dense matter.[99,134]

D. Orbital-Free DFT

1. Formulas

An alternative method of KS-DFT is Orbital free density functional theory (OF-DFT)[135,136], which achieves a more affordable computational complexity of $O(N\ln N)$ or $O(N)$ by calculating the non-interacting kinetic energy directly via charge density instead of Kohn-Sham orbitals. In OF-DFT, once the kinetic energy density functional (KEDF) is defined, the total energy is a pure functional of charge density, taking the form of

$$E_{\text{OF}}[\rho] = T_{\text{s}}[\rho] + E_{\text{ext}}[\rho] + E_{\text{H}}[\rho] + E_{\text{xc}}[\rho] + E_{\text{II}}, \quad (67)$$

so that the ground state energy can be obtained by directly minimizing the total energy functional with optimization algorithms,[137] such as the truncated Newton method[138] and the conjugate gradient method[139,140].

In practice, to guarantee the conservation of electrons, we define a Lagrangian as

$$L_{\text{OF}}[\rho] = E_{\text{OF}}[\rho] - \mu(\int \rho(\mathbf{r})\mathrm{d}^3\mathbf{r} - N), \quad (68)$$

where μ is the Lagrangian multiplier and the chemical potential. Then, the minimum of $L_{\text{OF}}[\rho]$ is found by optimizing $\phi(\mathbf{r}) \equiv \sqrt{\rho(\mathbf{r})}$, which guarantees the non-negativity of $\rho(\mathbf{r})$, and the variation of $L_{\text{OF}}[\rho]$ to $\phi(\mathbf{r})$ gives

$$\begin{aligned}\frac{\delta L}{\delta \phi} &= \frac{\delta E_{\text{OF}}[\rho]}{\delta \phi} - 2\mu\phi \\ &= 2(V_s + V_{\text{ext}} + V_{\text{H}} + V_{\text{xc}} - \mu)\phi.\end{aligned} \quad (69)$$

OF-DFT has been implemented in ABACUS using plane wave basis sets. Up to now, there are five available KEDFs in ABACUS, which are Thomas-Fermi (TF)[141,142], von Weizsäcker (vW)[143], TFλvW[144], Wang-Teter (WT)[145], Luo-Karasiev-Trickey (LKT)[146] KEDFs. Besides, due to the absence of Kohn-Sham orbitals, the commonly used norm-conserving pseudopotentials are usually unavailable in the field of OF-DFT unless special treatment is being used[147]. As a result, we use local pseudopotential (LPS) instead, and bulk-derived local pseudopotential (BLPS)[148], as well as high-quality local pseudopotential[149], are supported by ABACUS.

2. Kinetic Energy Density Functional

Given that T_s is of comparable magnitude to the total energy, the accuracy of OF-DFT is heavily dependent on the form of the KEDF. Nevertheless, the development of an accurate KEDF has remained a significant challenge in the field of OF-DFT for several decades.

Several analytical KEDFs have been proposed over the past few decades,[136,150] and they can be categorized into two main classes. First, the local and semilocal KEDFs are characterized by their kinetic energy density as a function of the charge density, its gradient, the Laplacian of the charge density, or even higher-order derivatives thereof.[141–143,146,151,152] Second, the nonlocal KEDFs define the kinetic energy density at each point in real space as a functional of the nonlocal charge density.[145,153–158] Semilocal KEDFs are generally more computationally efficient, while nonlocal KEDFs tend to provide greater accuracy. However, a universally applicable

KEDF that effectively describes both simple metal and semiconductor systems remains elusive, and a systematic approach to its construction has yet to be established.

Although the exact formula of the non-interacting kinetic energy T_s remains unknown, a rigorous lower bound is provided by the von Weizsäcker (vW) KEDF,[143] which is expressed as

$$T_{\mathrm{vW}} = \frac{1}{8} \int \frac{|\nabla \rho(\mathbf{r})|^2}{\rho(\mathbf{r})} \, d^3 \mathbf{r}. \tag{70}$$

The remaining part of the non-interacting kinetic energy, known as the Pauli energy,[159] is defined as

$$T_\theta = T_s - T_{\mathrm{vW}}. \tag{71}$$

This Pauli energy can be generally written as

$$T_\theta = \int \tau_{\mathrm{TF}} F_\theta \, d^3 \mathbf{r}, \tag{72}$$

where τ_{TF} is the Thomas-Fermi (TF) kinetic energy density[141,142], which is accurate for free electron gas (FEG),

$$\tau_{\mathrm{TF}} = \frac{3}{10} (3\pi^2)^{2/3} \rho^{5/3}. \tag{73}$$

Here, F_θ represents the enhancement factor. The corresponding Pauli potential is then given by

$$V_\theta(\mathbf{r}) = \delta E_\theta / \delta \rho(\mathbf{r}). \tag{74}$$

Notably, in a spin-degenerate system, the Pauli kinetic energy density can be expressed analytically using Kohn-Sham orbitals $\psi_i(\mathbf{r})$ and corresponding occupation numbers f_i,[159]

$$\tau_\theta^{\mathrm{KS}} = \sum_{i=1}^{M} f_i |\nabla \psi_i|^2 - \frac{|\nabla \rho|^2}{8\rho}, \tag{75}$$

where i indexes the Kohn-Sham orbitals. The Pauli potential is then defined by

$$V_\theta^{\mathrm{KS}} = \rho^{-1} \left(\tau_\theta^{\mathrm{KS}} + 2 \sum_{i=1}^{M} f_i (\varepsilon_M - \varepsilon_i) \psi_i^* \psi_i \right), \tag{76}$$

where ε_i represents the eigenvalue associated with the Kohn-Sham orbital $\psi_i(\mathbf{r})$. Additionally, M denotes the highest occupied state, and ε_M is the eigenvalue of $\psi_M(\mathbf{r})$, which corresponds to the chemical potential μ.

3. Machine Learning Based Kinetic Energy Density Functional

In recent years, machine learning (ML) techniques have breathed new life into the development of KEDF.[160–166] For example, Sun *et al.* imposed a machine learning based physical-constrained nonlocal (MPN) KEDF and implemented it in ABACUS.[166] The MPN KEDF is designed to satisfy three exact physical constraints: the scaling law of
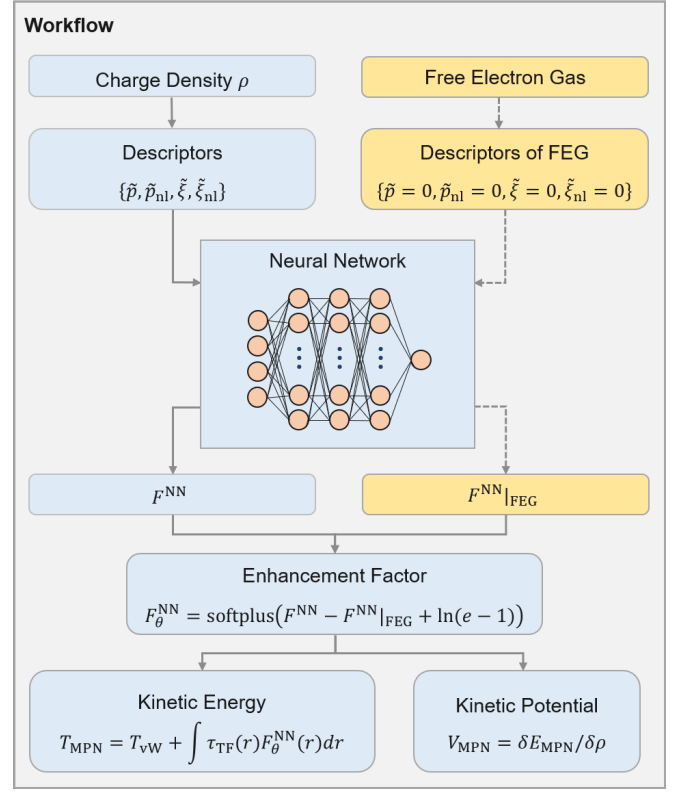

FIG. 16: Workflow of the MPN KEDF. (Adapted with permission from Phys. Rev. B, 109(11): 115135 (2024). Copyright 2024 American Physical Society.)

electron kinetic energy $T_\theta[\rho_\lambda] = \lambda^2 T_\theta[\rho], \rho_\lambda = \lambda^3 \rho(\lambda \mathbf{r})$, the free electron gas (FEG) limit, and the non-negativity of Pauli energy density.

As illustrated by Fig. 16, the core structure of the MPN KEDF is a neural network (NN). The output of the NN, denoted as $F^{\mathrm{NN}}(\mathbf{r})$, represents the enhancement factor F_θ for each real-space grid point $\mathbf{r}$. To ensure that the calculated Pauli energy and potential adhere to the FEG limit and the non-negativity of the Pauli energy density, the enhancement factor for the Pauli energy is defined as:

$$F_\theta^{\mathrm{NN}} = \mathrm{softplus}\left(F^{\mathrm{NN}} - F^{\mathrm{NN}}|_{\mathrm{FEG}} + \ln(e - 1) \right), \tag{77}$$

where $\mathrm{softplus}(x) = \ln(1 + e^x)$ is an activation function commonly used in machine learning, which satisfies $\mathrm{softplus}(x) \geq 0$ and $\mathrm{softplus}(x)|_{x=\ln(e-1)} = 1$. By construction, the non-negativity constraint is satisfied:

$$F_\theta^{\mathrm{NN}} \geq 0, \tag{78}$$

and the FEG limit, where the enhancement factor should be 1, is also met:

$$F_\theta^{\mathrm{NN}}|_{\mathrm{FEG}} = \mathrm{softplus}\left(F^{\mathrm{NN}}|_{\mathrm{FEG}} - F^{\mathrm{NN}}|_{\mathrm{FEG}} + \ln(e - 1) \right) \\ = 1. \tag{79}$$

Furthermore, the selection of the kernel function and descriptors ensures that once the FEG limit of the Pauli energy is
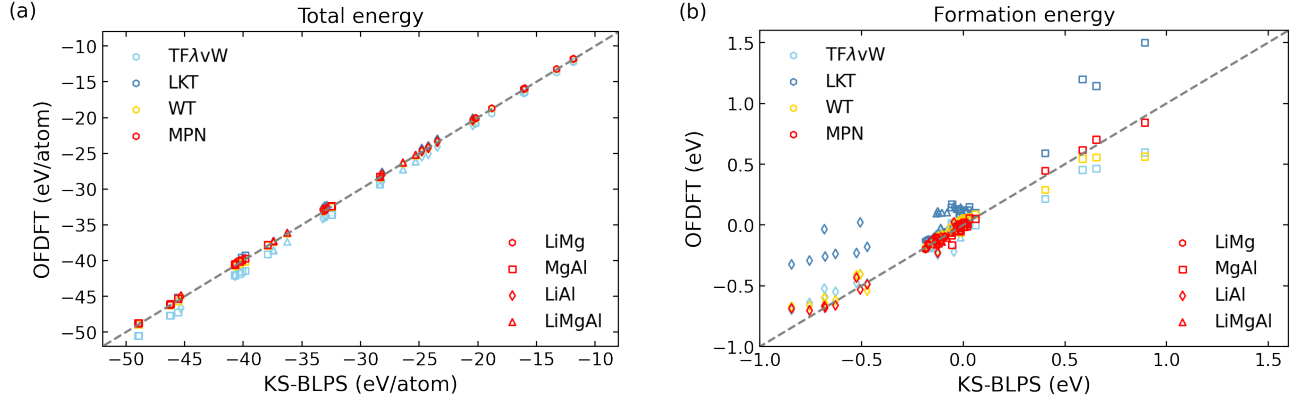
FIG. 17: (a) Total energies (in eV/atom) and (b) formation energies (in eV) of 59 alloys, including 20 Li-Mg alloys, 20 Mg-Li alloys, 10 Li-Al alloys, and 9 Li-Mg-Al alloys. Different colors indicate the formation energies from different KEDFs (TFλvW, LKT, WT, and MPN), while different shapes of markers indicate different alloys. (Adapted with permission from Phys. Rev. B, 109(11): 115135 (2024). Copyright 2024 American Physical Society.)

satisfied, the FEG limit of the Pauli potential is automatically fulfilled. The scaling law is ensured by the definition of the descriptors, which will be introduced subsequently.

As displayed in Fig. 16, the NN for the MPN KEDF uses four descriptors four descriptors $\{\tilde{p}, \tilde{p}_{nl}, \tilde{\xi}, \tilde{\xi}_{nl}\}$ as inputs. First, the semilocal descriptor $\tilde{p}$ is defined as the normalized dimensionless gradient of the charge density:

$$\tilde{p}(\mathbf{r}) = \tanh\left(0.2 p(\mathbf{r})\right), \tag{80}$$

where the parameter $p(\mathbf{r})$ is given by:

$$p(\mathbf{r}) = |\nabla\rho(\mathbf{r})|^2 / \left[2(3\pi^2)^{1/3}\rho^{4/3}(\mathbf{r})\right]^2. \tag{81}$$

The corresponding nonlocal descriptor $\tilde{p}_{nl}$ is defined as

$$\tilde{p}_{nl}(\mathbf{r}) = \int w(\mathbf{r}-\mathbf{r}')\tilde{p}(\mathbf{r}')\mathrm{d}^3\mathbf{r}', \tag{82}$$

where $w(\mathbf{r}-\mathbf{r}')$ is a kernel function similar to the WT kernel function[145]. This kernel function is defined in reciprocal space as:

$$w(\eta) = \left(\frac{1}{2} + \frac{1-\eta^2}{4\eta}\ln\left|\frac{1+\eta}{1-\eta}\right|\right)^{-1} - 3\eta^2 - 1, \tag{83}$$

where $\eta = \frac{k}{2k_F}$ is a dimensionless reciprocal space vector, and $k_F = (3\pi^2\rho_0)^{1/3}$ is the Fermi wave vector, with ρ_0 representing the average charge density.

The third and fourth nonlocal descriptors $\tilde{\xi}$ and $\tilde{\xi}_{nl}$ represent the distribution of charge density. These descriptors are defined as

$$\tilde{\xi}(\mathbf{r}) = \tanh\left(\frac{\int w(\mathbf{r}-\mathbf{r}')\rho^{1/3}(\mathbf{r}')\mathrm{d}^3\mathbf{r}'}{\rho^{1/3}(\mathbf{r})}\right), \tag{84}$$

and

$$\tilde{\xi}_{nl}(\mathbf{r}) = \int w(\mathbf{r}-\mathbf{r}')\tilde{\xi}(\mathbf{r}')\mathrm{d}^3\mathbf{r}'. \tag{85}$$

Here, $w(\mathbf{r}-\mathbf{r}')$ is the same kernel function used in the definition of the other nonlocal descriptors.

The loss function for the MPN KEDF is defined as

$$L = \frac{1}{N}\sum_{\mathbf{r}}\left[\left(\frac{F_\theta^{\mathrm{NN}} - F_\theta^{\mathrm{KS}}}{\bar{F}_\theta^{\mathrm{KS}}}\right)^2 + \left(\frac{V_\theta^{\mathrm{MPN}} - V_\theta^{\mathrm{KS}}}{\bar{V}_\theta^{\mathrm{KS}}}\right)^2\right]$$
$$+ \left[F^{\mathrm{NN}}|_{\mathrm{FEG}} - \ln(e-1)\right]^2, \tag{86}$$

where N is the total number of grid points, and $\bar{F}_\theta^{\mathrm{KS}}$ ($\bar{V}_\theta^{\mathrm{KS}}$) represents the mean value of F_θ^{KS} (V_θ^{KS}). The first term in the loss function accounts for the discrepancy between the predicted Pauli energy enhancement factor F_θ^{NN} and the reference KS Pauli energy enhancement factor F_θ^{KS}. The second term ensures that the predicted Pauli potential V_θ^{MPN} closely matches the KS Pauli potential V_θ^{KS}. This term is crucial because the Pauli potential plays a significant role in determining the optimization direction and step size during OF-DFT calculations. The final term is a penalty term designed to minimize the magnitude of the FEG correction, thereby enhancing the stability of the MPN KEDF.

The training set for the MPN KEDF includes eight metallic structures, specifically bcc Li, fcc Mg, fcc Al, as well as five alloys: Li_3Mg (mp-976254), LiMg (mp-1094889), Mg_3Al (mp-978271), β'' $MgAl_3$[167], $LiAl_3$ (mp-10890). The numbers in parentheses correspond to the Materials Project IDs.[168]

To evaluate the precision and transferability of the MPN KEDF, a test set was constructed using 59 alloys from the Materials Project database.[168] This testing set includes 20 Li-Mg alloys, 20 Mg-Li alloys, 10 Li-Al alloys, and 9 Li-Mg-Al alloys. The total energies and formation energies of 59 alloys as calculated by various KEDFs in OF-DFT are presented in Fig. 17. As depicted in Fig. 17(a), the TFλvW KEDF systematically underestimates the total energies compared to the results from KS-DFT, leading to a substantial mean absolute error (MAE) of 0.934 eV/atom. In contrast, the LKT KEDF demonstrates improved performance with a reduced MAE of 0.145 eV/atom. The nonlocal WT KEDF further enhances ac-

curacy, achieving an MAE of 0.043 eV/atom. Although the MPN KEDF has a higher MAE of 0.123 eV/atom compared to the WT KEDF, it still outperforms both the TFλvW and LKT KEDFs.

Fig. 17(b) illustrates the formation energies. The LKT KEDF consistently overestimates the values compared to those obtained by KS-DFT and yields a high MAE of 0.166 eV. This is significantly larger than the MAEs achieved by the TFλvW KEDF (0.051 eV) and the WT KEDF (0.035 eV). Notably, the MPN KEDF demonstrates superior performance with an even lower MAE of 0.028 eV, outperforming the WT KEDF.

In conclusion, the MPN KEDF exhibits promising potential in accurately predicting the energies of complex alloy systems. The high accuracy achieved by the MPN KEDF suggests its capability to provide reliable energy predictions for a wide range of materials.

V. METHODS IN NUMERICAL ATOMIC ORBITAL BASIS

A. Numerical Atomic Orbitals

The efficiency and accuracy first-principles are largely determined by the basis sets. Although the accuracy of plane-wave basis mentioned in Sec. IV can be systematically improved by increasing the kinetic energy cutoff, its computational costs are formidable for systems of hundreds or thousands of atoms. On the other hand, the atomic orbital basis sets often provide more efficient description and room for optimization (like linear-scaling methods) at the cost of minor accuracy loss.

In the past two decades, numerical atomic orbitals (NAOs) have become a competitive option for basis set types, especially for simulating large systems. The NAO basis sets are favorable for their flexibility, excellent balance between accuracy and efficiency, the capability of supporting linear scaling algorithms via their strict locality, etc. Over the past several decades, several methods have been proposed[51,169–173] to perform numerical integrations for NAOs more efficiently, thus efficient computation of large systems on the NAO basis can be achieved.

Unlike plane-wave basis, there is no unique way to construct NAOs. For example, a popular class of methods involves solving isolated atoms subject to confining potentials[173–177]. Based on confining potentials, Blum $et\ al$[51] proposed to generate NAOs by iteratively picking up basis functions one by one from a pool of predefined candidates, to seek the best improvement of a target energy. Alternatively, Ozaki[178,179] suggests that eigenfunctions of isolated atoms in confining potentials serve as "primitive orbitals" in terms of which NAOs are expanded, and expansion coefficients can be optimized alongside self-consistent cycles.

Apart from the above energy-based methods, another class of methods constructs NAOs towards some reference states. For example, Sanchez-Portal $et\ al$[180,181] proposed to optimize

the following "spillage"

$$\mathscr{S} = \sum_{n\mathbf{k}} \langle \psi_n(\mathbf{k})|(1-\hat{P}(\mathbf{k})|\psi_n(\mathbf{k})\rangle \tag{87}$$

$$= \sum_{n\mathbf{k}} \left\| (1-\hat{P}(\mathbf{k})) |\psi_n(\mathbf{k})\rangle \right\|^2, \tag{88}$$

where $\{\psi_n(\mathbf{k})\}$ denotes reference states from plane-wave calculations, $\hat{P}(\mathbf{k})$ is the projection operator onto the subspace of Bloch functions characterized by $\mathbf{k}$ and spanned by atomic orbitals:

$$P(\mathbf{k}) \equiv \sum_{\mu\nu} \left| \phi_\mu(\mathbf{k}) \right\rangle S_{\mu\nu}^{-1}(\mathbf{k}) \left\langle \phi_\nu(\mathbf{k}) \right| \tag{89}$$

and $S_{\mu\nu}(\mathbf{k}) \equiv \langle \phi_\mu(\mathbf{k})|\phi_\nu(\mathbf{k}) \rangle$ is the overlap matrix. In their original scheme, NAOs are chosen to be combinations of pseudo-atomic orbitals (eigenfunctions of isolated atoms with pseudo-potentials) or Slater-type orbitals, and reference systems are ordinary solids. Based on the spillage formalism, Chen, Guo, and He (CGH)[20] proposed to construct NAOs with localized spherical waves[182], and reference systems are chosen to be a series of isolated dimers/trimers of variable bond lengths. The CGH basis set turns out to have a very small eggbox effect[22] and has been successfully applied to several studies[100,105,183]. Recently, Lin, Ren, and He (LRH)[26] show that the CGH basis set can be further improved by introducing a gradient term to the original spillage ($\hat{p}$ is the momentum operator):

$$\mathscr{S}^{\text{LRH}} = \mathscr{S} + \sum_{n\mathbf{k}} \left\| \hat{p}(1-\hat{P}(\mathbf{k})) |\psi_n(\mathbf{k})\rangle \right\|^2. \tag{90}$$

CGH and LRH basis sets paired with SG15 pseudopotentials[184] are publicly available[185] and have been extensively tested (see Sec. V B). In ABACUS, the implementation of NAO basis relies on CGH and LRH basis.

B. Kohn-Sham Equation in NAO Basis

With the usage of localized basis set, the Kohn-Sham equation for a given $\mathbf{k}$ point in the Brillouin zone becomes a generalized eigenvalue problem that takes the form of

$$H(\mathbf{k})C(\mathbf{k}) = S(\mathbf{k})C(\mathbf{k})E(\mathbf{k}), \tag{91}$$

in which $H(\mathbf{k}), C(\mathbf{k})$, and $S(\mathbf{k})$ are the Hamiltonian matrix, the electronic wave function coefficients of NAOs, and overlap matrix, respectively. The $E(\mathbf{k})$ is a diagonal matrix with KS eigenvalues.

In general, the terms in Hamiltonian matrix $H(\mathbf{k})$ are constructed in two ways, i.e., the two-center integrals and the grid integral techniques. Given an operator $\hat{O}$, the two-center integral calculates

$$O_{\mu\nu}(\mathbf{R}) = \int \phi_\mu(\mathbf{r})\hat{O}\phi_\nu(\mathbf{r}-\mathbf{R})d\mathbf{r}, \tag{92}$$

in which functions ϕ (basis or any "projector") centered at atoms spaced by $\mathbf{R}$ are distinguished by μ and ν. The overlap

matrix $S_{\mu\nu}(\mathbf{R})$ and the kinetic energy matrix $T_{\mu\nu}(\mathbf{R})$ are evaluated directly with this form, while the representation of the non-local part of pseudopotential requires the calculation of

$$V_{\mu\nu}^{\mathrm{NL}}(\mathbf{R}) = \sum_{Iij} D_{ij}^{I} \langle \phi_{\mu\mathbf{0}} | \beta_i^I \rangle \langle \beta_j^I | \phi_{\nu\mathbf{R}} \rangle. \quad (93)$$

Equation 91 is solved independently for each $\mathbf{k}$. The representation of Hamiltonian or any operator within the momentum space is obtained via a "folding" operation

$$H_{\mu\nu}(\mathbf{k}) = \sum_{\mathbf{R}} H_{\mu\nu}(\mathbf{R}) e^{i\mathbf{k}\cdot\mathbf{R}}, \quad (94)$$

in which $\mathbf{R}$ always runs over all valid neighboring cells. Band energy can be obtained through the expectation of the Hamiltonian:

$$E_{\mathrm{band}} = \sum_{n\mathbf{k}} f_{n\mathbf{k}} \langle \psi_{n\mathbf{k}} | \hat{H} | \psi_{n\mathbf{k}} \rangle = \sum_{\mu\nu,\mathbf{k}} \rho_{\nu\mu}(\mathbf{k}) H_{\mu\nu}(\mathbf{k}) = \mathrm{Tr}(\rho H), \quad (95)$$

in which the density matrix is defined as

$$\rho_{\mu\nu}(\mathbf{k}) = \sum_{n} f_{n\mathbf{k}} C_{n\mu}(\mathbf{k}) C_{n\nu}^*(\mathbf{k}). \quad (96)$$

The spinor index is omitted here. Real-space density matrix $\rho_{\mu\nu}(\mathbf{R})$ is calculated through Fourier transform accordingly.

C. Forces and Stresses

To obtain the analytical expression for force and stress, one must start with the analytical expression for energy

$$E_{\mathrm{total}} = \sum_{\mu\nu,\mathbf{R}} \rho_{\nu\mu}(\mathbf{R}) \left[T_{\mu\nu}(\mathbf{R}) + V_{\mu\nu}^{NL}(\mathbf{R}) \right] + \int V_{\mathrm{local}}(\mathbf{r}) \rho(\mathbf{r}) \mathrm{d}\mathbf{r}$$
$$+ \frac{1}{2} \iint \frac{\rho(\mathbf{r})\rho(\mathbf{r}')}{|\mathbf{r} - \mathbf{r}'|} \mathrm{d}\mathbf{r}\mathrm{d}\mathbf{r}' + \int \varepsilon_{\mathrm{xc}}(\mathbf{r}) \rho(\mathbf{r}) \mathrm{d}\mathbf{r} + E_{\mathrm{II}}, \quad (97)$$

where the ionic energy is given by the Ewald method[47]. It should be noted that ABACUS uses Eq. 36 to calculate the total energy in practical computations. For more information about evaluating force and stress terms in ABACUS, we refer the readers to a recent review work in Ref. [32].

The atomic forces are obtained by direct differentiation with respect to atomic positions

$$\mathbf{F}_I = -\sum_{\mu\nu} \sum_{\mathbf{R}} \rho_{\nu\mu}(\mathbf{R}) \frac{\partial H_{\mu\nu}(\mathbf{R})}{\partial \mathbf{R}_I} - \sum_{\mu\nu} \frac{\partial \rho_{\nu\mu}(\mathbf{R})}{\partial \mathbf{R}_I} H_{\mu\nu}(\mathbf{R})$$
$$= \mathbf{F}_I^{\mathrm{HF}} + \mathbf{F}_I^{\mathrm{Pulay}} + \mathbf{F}_I^{\mathrm{Orth}} + \mathbf{F}_I^{\mathrm{Ewald}}. \quad (98)$$

According to the Hellmann-Feynman theorem[117,118], the HF force $\mathbf{F}_I^{\mathrm{HF}}$ describes the contribution of the partial derivatives of the operator. However, since the positions of the NAOs basis set change with the atomic positions, the partial derivatives of the basis set with respect to nuclear positions also contribute to the atomic forces, which are referred to as the Pulay forces $\mathbf{F}_I^{\mathrm{Pulay}}$. The orthogonal force $\mathbf{F}_I^{\mathrm{Orth}}$ is a correction term. The final term $\mathbf{F}_I^{\mathrm{Ewald}}$ represents the contribution of ionic interactions to atomic forces.
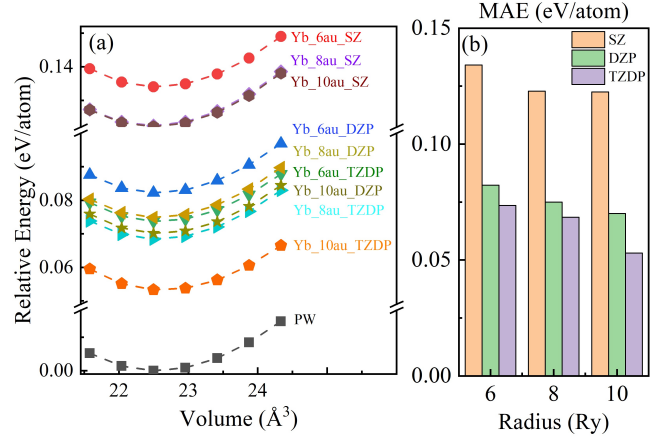
FIG. 18: (a) Comparison on energies calculated with NAO and PW basis set for the $\mathrm{Li}_{12}\mathrm{Yb}_4\mathrm{Cl}_{24}$ system calculated using Yb SZ/DZP/TZDP orbitals with different orbital cutoffs. (b) MAE is the mean absolute error of the energies between NAO and PW for different volumes, with the unit being eV/atom.

The stress tensor can be defined as the positive derivative of the total energy Eq.97 with respect to the strain tensor (Eq. 25). Taking advantage of the relation $\frac{\partial r_\gamma}{\partial \varepsilon_{\alpha\beta}} = \delta_{\gamma\alpha} r_\beta$, the stress calculation can be derived in a form very similar to that of force calculation through[32]

$$\frac{\partial H_{\mu\nu}}{\partial \varepsilon_{\alpha\beta}} = \sum_\gamma \frac{\partial H_{\mu\nu}}{\partial \mathbf{R}_{\mu\nu}^\gamma} \frac{\partial \mathbf{R}_{\mu\nu}^\gamma}{\partial \varepsilon_{\alpha\beta}} = \frac{\partial H_{\mu\nu}}{\partial \mathbf{R}_{\mu\nu}^\alpha} \mathbf{R}_{\mu\nu}^\beta, \quad (99)$$

where γ represent coordinate components x, y, z. In fact, atomic force and stress are computed at almost the same place in the code. We will not elaborate further here.

We verify the accuracy of the NAOs by comparing the results with the plane-wave method. We have generated a series of NAOs, including Single-ζ (SZ), Double-ζ plus polarization functions (DZP), and Triple-ζ plus double polarization functions (TZDP) with different cutoffs based on the Pseudo-Dojo v0.4 (3plus) pseudopotential for Yb and carried out self-consistent field calculations using these orbitals. The results are in Fig. 18. It is evident that including more atomic orbitals and utilizing larger cutoffs can effectively reduce the difference in total energy between NAO and PW calculations. For example, the total energy calculated using the TZDP orbitals with a cutoff of 10 a.u. is closest to the PW results, with a deviation of about 0.0053 eV/atom.

We have performed the finite difference tests for atomic forces using body-centered cubic (BCC) Fe (perturbing the position of one Fe atom so that the structure can deviate from the equilibrium position), which specifically involved moving one Fe atom in the positive and negative direction of the x-axis by a particular step size and calculating the energy. Fig. 19(a) shows the atomic forces calculated by the finite difference method (step size is 0.02 Bohr) and the analytical values at different positions of the Fe atom. The difference between

them is plotted in the zoom-in figure. It is apparent that for the Fe systems, this force discrepancy is around 0.002 eV/Å. This discrepancy can be affected by a few factors, including the precision of the finite difference method (step size) and the precision of the energy (including the accuracy of the SCF calculations and numerical errors). Fig. 19(b) shows the value of this discrepancy for different step sizes used in finite difference. As the differential step size decreases, the discrepancy gradually reduces and tends toward zero, indicating that the force in ABACUS LCAO implementation is sufficiently consistent with the energy. Stress can be verified similarly by slightly changing the lattice vectors.
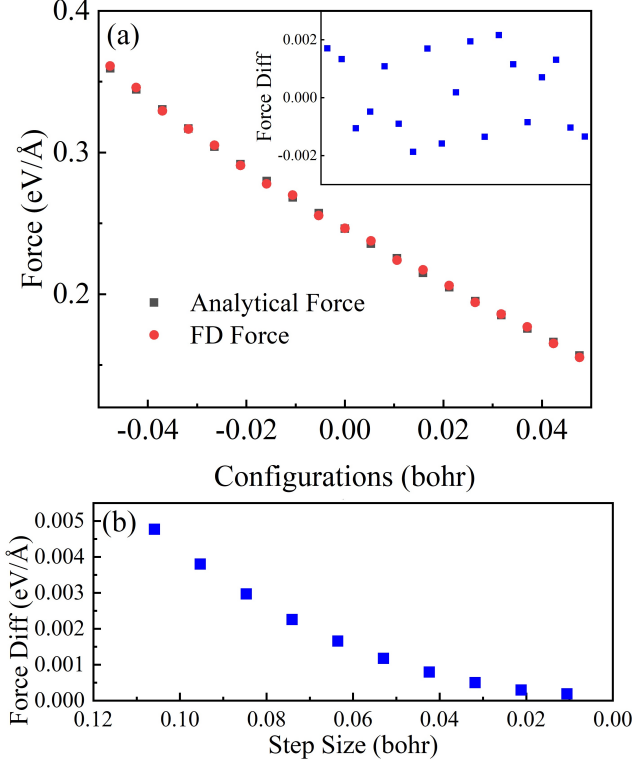

FIG. 19: By using the NAO basis set, the finite difference (FD) tests of atomic forces on the x-axis of BCC Fe. a) The analytical forces and the forces calculated by the finite difference method along the x-direction for different configurations. The zoom-in figure shows the difference between them; b) The deviations between FD values and analytical values along the Fe x-direction for different step sizes used in the finite difference method.

D. Diagonalization-Based Eigensolvers

In the SCF calculations using the NAO basis set of ABACUS, the combined computational time for grid integrals and generalized eigenvalue solving exceeds 90%. For the generalized eigenvalue and eigenvector solving, ABACUS invokes the libraries scalapack[186] and ELPA[187].

We have accelerated these computational loads using GPUs. ABACUS integrates GPU-supported libraries such as ELPA[188], cuSolvermp[189], and cuSolver. Although cuSolvermp demonstrates superior diagonalization performance on NVIDIA GPU clusters[189], we still recommend users to utilize ELPA as the diagonalization library for large-scale, multi-node, multi-GPU computations in most cases. This recommendation is based on three key factors related to performance and ease of use: 1) The generalized eigenvalue solving process in ABACUS using the NAO basis set does not require solving for all eigenvectors, and ELPA supports configuring the number of eigenvectors to be solved; 2) The self-consistent iterative calculations in ABACUS involve solving eigenvalues and eigenvectors multiple times, and ELPA can avoid repeated S-matrix decompositions; 3) ELPA provides broad support for various GPU computing stacks, including those from NVIDIA, AMD, and INTEL, reducing the barrier for users across different hardware platforms. Besides, ABACUS also provides a low-scaling solver PEXSI (see Sec. VII H).

E. Hybrid Funtional

Hybrid density functionals (HDFs) formulated within the generalized KS framework[190] belongs to the fourth rung of the Jacob's ladder[191]. It overcomes the drawbacks of the (semi-)local XC functionals, namely the self-interaction errors[192,193] related to the underestimation of the band gaps.

ABACUS supports pure exact exchange (EXX), namely Hartree-Fock (HF). Based on that, we implement various hybrid functionals, including HSE[60], PBE0[194,195] and SCAN0[196], which are mixtures of EXX and (semi-)local XC functionals. The local part is calculated with LibXC[197], while the exact (or Fock) exchange energy is given by the 2-electron integrals of the Kohn-Sham orbitals:

$$E_x^{EX} = \frac{1}{N_\mathbf{k}^2} \sum_{i\mathbf{k}} \sum_{j\mathbf{k}'} f_i f_j \int d\mathbf{r} \int d\mathbf{r}' \psi_{i\mathbf{k}}^*(\mathbf{r}) \psi_{j\mathbf{k}'}(\mathbf{r})$$
$$v(|\mathbf{r} - \mathbf{r}'|) \psi_{j\mathbf{k}'}^*(\mathbf{r}') \psi_{i\mathbf{k}}(\mathbf{r}'). \quad (100)$$

The exact exchange Hamiltonian under the representation of NAOs basis is given by

$$H_{U\mu,V\nu}^{EXX}(\mathbf{R}_{UV}) = \sum_{KL\mathbf{R}_{KL}} \sum_{kl} \sum_{\mathbf{R}'} D_{K\kappa,L\lambda}$$
$$(\mathbf{R}_{KL}) \langle \phi_{U\mu}^{\mathbf{0}} \phi_{K\kappa}^{\mathbf{R}'} | \hat{K} | \phi_{V\nu}^{\mathbf{R}_{UV}} \phi_{L\lambda}^{\mathbf{R}'+\mathbf{R}_{KL}} \rangle, \quad (101)$$

in which $\hat{K}$ is the exchange operator, the density matrix and the 4-center integrals are defined as

$$D_{K\kappa,L\lambda}(\mathbf{R}_{KL}) = \frac{1}{N_\mathbf{k}} \sum_{j\mathbf{k}} f_j c_{j\mathbf{k},K\kappa} c_{j\mathbf{k},L\lambda}^* e^{-i\mathbf{k}\cdot\mathbf{R}_{KL}}, \quad (102)$$

$$\langle \phi_{U\mu}^{\mathbf{R}_U} \phi_{K\kappa}^{\mathbf{R}_K} | \hat{K} | \phi_{V\nu}^{\mathbf{R}_V} \phi_{L\lambda}^{\mathbf{R}_L} \rangle = \int d\mathbf{r} \int d\mathbf{r}' \phi_{U\mu}^{\mathbf{R}_U}(\mathbf{r}) \phi_{K\kappa}^{\mathbf{R}_K}(\mathbf{r})$$
$$v(\mathbf{r} - \mathbf{r}') \phi_{V\nu}^{\mathbf{R}_V}(\mathbf{r}') \phi_{L\lambda}^{\mathbf{R}_L}(\mathbf{r}'), \quad (103)$$

with $v(\mathbf{r} - \mathbf{r}') = 1/|\mathbf{r} - \mathbf{r}'|$ for the bare Coulomb in PBE0 and HF and $v(\mathbf{r} - \mathbf{r}') = \mathrm{erfc}(\omega|\mathbf{r} - \mathbf{r}'|)/|\mathbf{r} - \mathbf{r}'|$ for short-range EXX in HSE.

1. Local Resolution of Identity

The $O(N^4)$ scaling EXX effective potential is much more consuming for both time and memory than the local ones. To address this, various types of algorithms have been developed, one of them is the resolution of identity (RI)[198–200] or density fitting[201] technique, reducing the 4-center integrals to 3- and 2-center ones by expanding the orbital products on a set of auxiliary basis functions (ABFs). Aiming at HDF calculations of large periodic systems, local resolution of identity (LRI)[23,202,203] can be employed to achieve linear-scaling EXX calculations due to the locality of the atomic orbitals (AOs) and ABFs. If the ABFs are well chosen, the LRI approximation can be adequately accurate for HDF calculations, as benchmark tested[23]. Most of the remaining differences in the obtained cohesive properties and band gaps result from the core–valence interaction treatment (pseudopotentials versus all-electron) rather than the basis set differences[204].

There are two types of ABFs used in ABACUS: the "on-site" ones to fit the products of orbitals on the same atoms, and the "opt" ones to improve the fitting of different-atom orbital products. Both of them have the same function type as AOs, i.e. a radial function times a spherical harmonics: $P_{A\alpha=\{nlm\}}(\mathbf{r}) = g_{nl}(r)Y_{lm}(\hat{\mathbf{r}})$. The radial part of "on-site" ABFs are generated by multiplying the radial part of each AO pair on the same atom: $g_{nl}(r) = f_{n_1 l_1}(r)f_{n_2 l_2}(r)$, $|l_1 - l_2| \le l \le l_1 + l_2$, and then orthogonalized and selected by principal component analysis (PCA). The "opt" ABFs are generated in the same way as AO-generation[205,206].

Due to the locality of the AOs and density matrix, the submatrices involved in calculations are close to zero on many occasions and can be prescreened by a given threshold respectively. There are two ways to distribute the 4-center-integral tasks. One is the greedy algorithm for multi-machine scheduling aiming at load balance, and the other is to distribute the ABFs-located atom pairs according to the K-means clustering result, so that the pairs on the same processor are as close as possible to each other, and the memory consumption in direct proportion to the union of their adjacent tables is minimized[25].

To minimize the copy of tensors between processors, the users are recommended to use thread-level parallelism (OpenMP) within one node and process-level parallelism (MPI) between nodes.

To set up the hybrid functional calculation with LRI-based EXX, the "on-site" ABFs are generated according to the read-in AOs and then orthogonalized and PCA-selected, and the "opt" ABFs are read in if provided. After that, the 2-center radial integral interpolation table between AOs and ABFs are constructed. The above steps are done only once at the beginning of the program.

For each configuration, or in each ion step, the position-dependent tensors C, V are calculated before the SCF iterations, and force and stress are calculated (if needed) after the

convergence of SCF iterations. The middle part is composed of at least two SCF iterations: The first one with PBE functional is to get the density matrix to initialize the EXX calculation. After that, there are two different modes to converge the hybrid functional SCF iterations:

Non-separate-loop mode In the second SCF iteration, the EXX energy and Hamiltonian are updated with the current density matrix in every electronic step. Compared to the separate-loop mode, each electronic step takes longer, but usually, fewer steps are needed to converge the SCF iteration.

Separate-loop mode In this mode, two layers of loops are used to converge the SCF iteration: The EXX energy and Hamiltonian are updated only at the beginning of the outer loop, which will be fixed and added to the total energy and Hamiltonian in the inner loop (where the density matrix and (semi-)local parts of Hamiltonian are updated). After the inner loop converges, the program checks the outer loop's convergence and returns to the EXX-update step if it has not converged. The whole workflow of hybrid functional implementation in ABACUS is shown in Fig. 20.

It is also worth mentioning that the LRI-based 4-center integration step has been individually packaged into a library named LibRI[207], which can be integrated into other DFT or beyond-DFT (such as RPA and GW) codes[208] to speed up the calculation of the two-electron Coulomb repulsion integrals.

2. Results

The EXX module of ABACUS has already been put into several works[23,209,210]. In 2024, Lin *et al.* studied the effect of exact exchange on some of the lead-free halide double perovskites (HDPs) $Cs_2BB'X_6$ (B=Ag$^+$, Na$^+$; B=In^{3+}, Bi^{3+}; X=Cl$^-$, Br$^-$)[209]. They found some local exchange-correlation functionals fail to capture the geometric and electronic structures of $Cs_2BB'X_6$, which can be traced back to the so-called delocalization error. To show the differences between these functionals, they calculated the band gap as a function of the B-X bond length using the functionals: PBE, PBEsol, SCAN, HSE, and HSE (0.4). Taking $Cs_2AgInCl_6$ as an example in Fig. 22, one can see the band gap obtained at Ag-Cl bond length (2.724 Å) is in much better agreement with the experimental value (3.3 eV), marked by the red triangle.

Generally speaking, hybrid functional calculations can only process systems of limited size due to the large computational demand of building the exact exchange Hamiltonian. By combining NAOs basis and LRI techniques, Fig. 21 shows the time consumption of this part increases almost linearly with the system size, enabling ABACUS to perform hybrid functional calculations for systems with thousands of atoms. In 2024, Tang *et al.* used hybrid functional data from ABACUS and trained a deep equivariant neural network approach for efficient hybrid density functional calculations[210]. Taking twisted bilayer graphene (TBG) as an example in Fig. 24, they performed the HSE band structure calculations of (17, 16) TBG (twist angle $\theta \approx 2.0046°$, 3,268 atoms/cell)[210].

We alo perform HSE calculations to obtain the band gaps of several semiconductors and compare them with the results
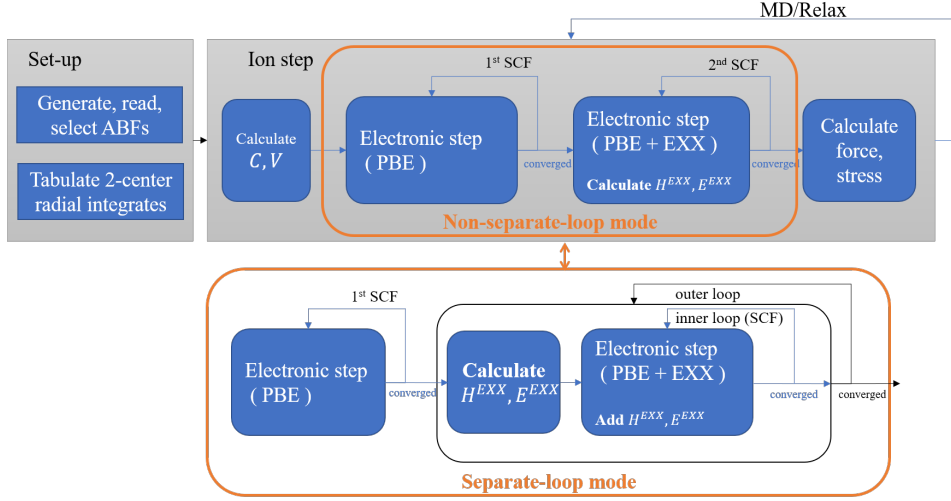
FIG. 20: Flowchart of the hybrid functional as implemented with numerical atomic orbitals and LRI-based exact exchange calculations in ABACUS.
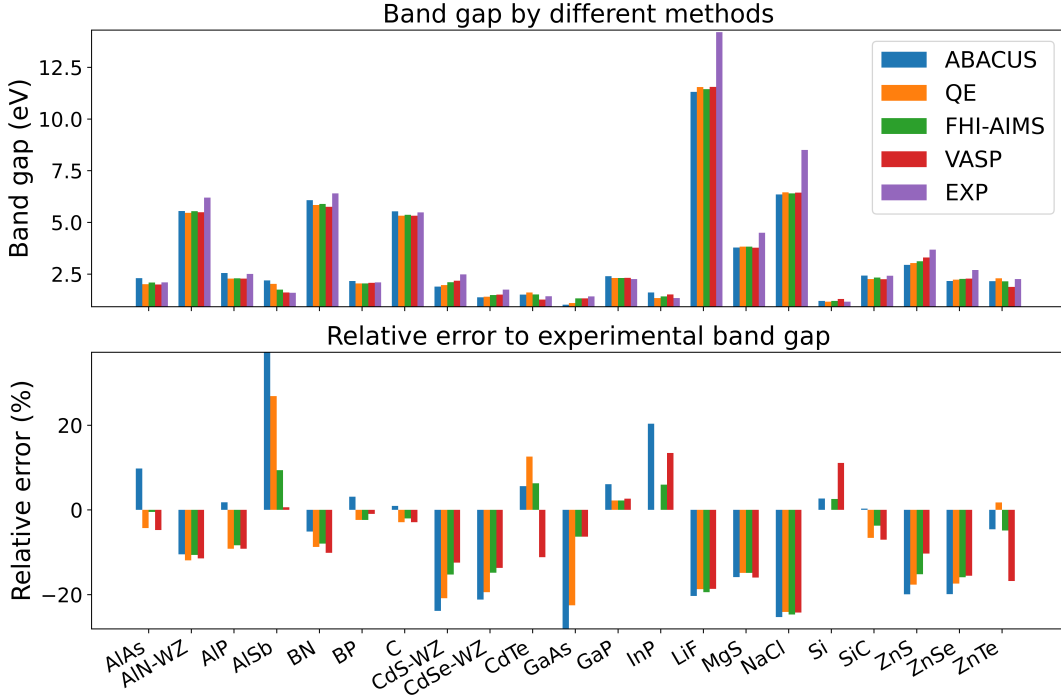

FIG. 21: The band gap of each system, calculated by ABACUS, along with the reference computed values from other software (QE/FHI-AIMS/VASP) and experimental values, is also presented online[122].

from other DFT packages (QE/VASP/FHI-AIMS) and the experimental values[23,211]. In these tests, ABACUS and QE employ the SG15-type norm-conserving PBE pseudopotentials (except for In is PSlibrary norm-conserving), VASP employs the PBE PAW potentials, whereas FHI-AMIS performs all-electron calculations[212]. Fig. 21 shows that the band gaps obtained by ABACUS HSE calculations are consistent with the results from other DFT packages, demonstrating satisfactory results when compared to the experimental values.

F. The DeePKS Method

Density functional theory has been widely used to calculate the electronic structural properties of molecules and condensed systems. The exchange-correlation functional plays a crucial role in determining the accuracy of DFT. However, when selecting different levels of XC functionals, there is a trade-off between accuracy and efficiency. A lower-level XC functional in the Jacob ladder[213] usually has higher computa-
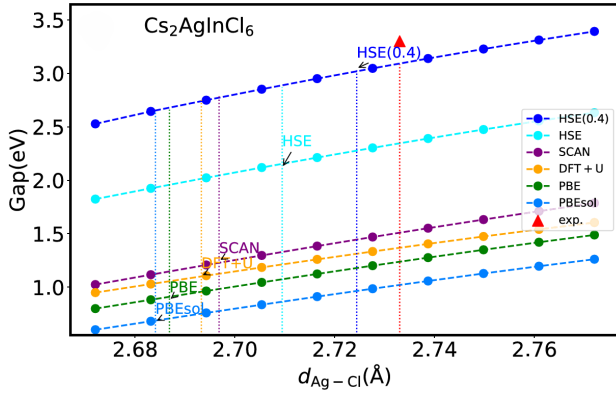
FIG. 22: Band gaps of $Cs_2AgInCl_6$ with a lattice constant of 10.481 Å predicted by HSE(0.4), HSE, SCAN, DFT+U, PBE, and PBEsol as a function of Ag-Cl bond length. (Adapted with permission from Phys. Rev. Research 6, 033172 (2024). Copyright 2024 American Physical Society.)

FIG. 24: The PBE and HSE06 band structures of twisted bilayer graphene with $\theta \approx 2.0046°$, 3268 atoms/cell computed by ABACUS. (Adapted with permission from Nat Commun 15, 8815 (2024). Copyright 2024 Springer Nature.)
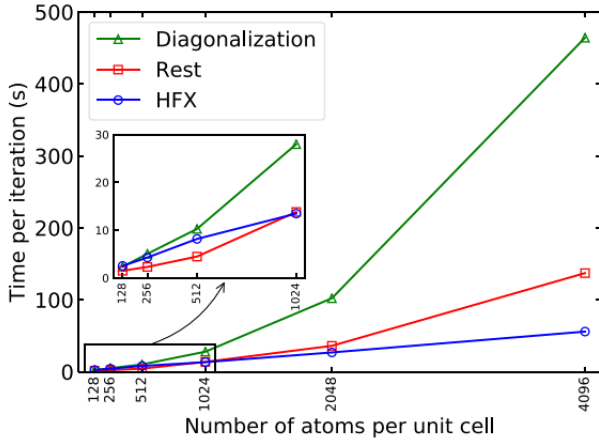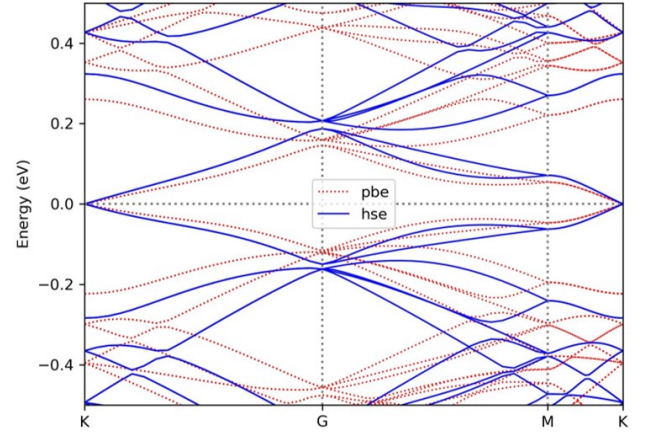

FIG. 23: Time consumption per iteration of three main parts in ABACUS SCF calculations using hybrid functional. Here HFX represents the HFX matrix construction, and Rest means the rest of time. (Adapted with permission from J. Chem. Theory Comput. 2021, 17, 1, 222–239. Copyright 2021 American Chemical Society.)

tional efficiency but lower accuracy, while a higher-level one has the opposite. With the rapid advancement of extensive computational resources and advanced algorithms, Artificial Intelligence assisted methods have the potential to help solve this problem[214,215].

Proposed in 2020, DeeP Kohn-Sham method (DeePKS)[36] employs a computationally efficient neural network-based functional model to represent the difference between a lower-level XC functional and a higher-level XC functional. The resulting model maintains translational, rotational, and permutational invariance and can be used in self-consistent field calculations. Together with DeePKS-kit[37] software, ABACUS supports the iterative training of DeePKS models[45]. It can be trained in molecular or periodic systems and supports training for properties such as energy, force, stress, and bandgap.

Based on the DeePKS model, ABACUS can achieve accuracy similar to that of the high-level XC functional on these specified properties, while the computational efficiency is similar to that of the low-level XC functional.

We divide the energy functional into two parts:

$$E_{\text{DeePKS}}[\{\psi_i\}|\omega] = E_{\text{baseline}}[\{\psi_i\}] + E_\delta[\{\psi_i\}|\omega], \quad (104)$$

where $\{\psi_i\}$ are single-particle orbitals, and E_δ is constructed as a neural network model with parameters ω.

The model input is constructed based on the projected density matrix:

$$D^I_{nlmm'} = \sum_{\mu\nu}\langle\alpha^I_{nlm'}|\phi_\nu\rangle\rho_{\mu\nu}\langle\phi_\mu|\alpha^I_{nlm}\rangle. \quad (105)$$

Here $\rho_{\mu\nu}$ represents the density matrix, and $|\alpha\rangle$ is a set of localized orbitals centered on atoms, identified by atomic index I, and quantum numbers nlm. The atomic-centered basis functions $|\alpha\rangle$ ensure the translational invariance. To maintain rotational invariance, we proceed to extract the eigenvalues of projected density matrix blocks with the same indices I, n, and l, resulting in a set of descriptors:

$$\mathbf{d}^I_{nlm} = \text{Eig}(D^I_{nlmm'}). \quad (106)$$

The descriptors are grouped into vectors based on the atomic index I, and E_δ is calculated as the sum of atomic contributions:

$$E_\delta = \sum_I F_{\text{NN}}(\mathbf{d}^I|\omega), \quad (107)$$

which guarantees the invariance under permutations. F_{NN} is the deep neural network.

Here, with the expression of the energy functional in mind, the Hamiltonian operator can be written as :

$$H = H_{\text{baseline}} + \hat{V}^\delta. \quad (108)$$

The matrix elements of the correction potential are as follows:

$$\hat{V}_{\mu\nu}^{\delta} = \frac{\partial E_{\delta}}{\partial \rho_{\mu\nu}}$$

$$= \sum_{Inlmm'} \frac{\partial E_{\delta}}{\partial D_{nlmm'}} \frac{\partial D_{nlmm'}^{I}}{\partial \rho_{\mu\nu}}$$

$$= \sum_{Inlmm'} \langle \chi_{\mu} | \alpha_{nlm}^{I} \rangle \frac{\partial E_{\delta}}{\partial D_{nlmm'}^{I}} \langle \alpha_{nlm'}^{I} | \chi_{\nu} \rangle. \qquad (109)$$

A trained DeePKS model provides the chance to perform KS-DFT calculations with high computational accuracy and efficiency at the same time. It can be applied to precisely predict various properties for a family of systems and potentially facilitate the discovery and design of novel materials.

For instance, Ou *et al.*[216] established a general DeePKS model that can be utilized for a plethora of halide perovskites, including different combinations of ABX_3 (A=FA, MA, Cs; B=Sn, Pb; X=Cl, Br, I), the organic-inorganic hybrid alternatives and the Ruddlesden-Popper (RP) perovskites. Halide perovskites (ABX_3, X=halogen anion) have shown great promise as a cost-effective alternative to current commercial photovoltaic technologies. One key benefit of halide perovskites is adjusting the absorption edge wavelength (band gap) by changing the ratio of different halide ions. Designing effective photovoltaic systems requires a precise yet efficient description of the electronic structure of halide perovskites.

They built an extensive DeePKS model upon 460 configurations spanning seven types of halide perovskites, with HSE06 accuracy and satisfactory predictions for the band gap. Based on an iterative training process with ABACUS and DeePKS-kit, they showed that the resulting DeePKS model can accurately replicate forces, stress, band gaps, and density of states (DOS) near the Fermi energy for all types of halide perovskites, including RP structures, and hybrid compositions, when compared to HSE06. For example, they show the band gaps predicted by DeePKS and PBE, with respect to those by HSE06, over 30 tested systems. As depicted in Fig. 25, The DeePKS model demonstrated precise predictions of band gaps for all perovskites examined, closely aligning with the HSE06 findings and yielding an average absolute error (MAE) of 0.0350 eV. PBE significantly underestimated the band gap values, with a large MAE of 0.5222 eV.

In addition to providing an accurate yet efficient description of the electronic structure, DeePKS also serves as a "bridge" between expensive quantum mechanical (QM) models and machine learning (ML)-based potentials. While the ML-based potentials such as the Deep Potential Molecular Dynamics (DeePMD)[34,35] have emerged as powerful tools for mitigating the high computational costs associated with ab initio molecular dynamics (AIMD), training these potentials demands a significant number of QM-labeled frames. DeePKS offers a solution to further save the computational cost by reducing the required QM-labeled frames, owing to its significantly better transferability as compared to DeePMD.

Li *et al.*[45] examined DeePKS and DeePMD's training curves with respect to training samples in systems with 64 water molecules at the accuracy of hybrid functional SCAN0.
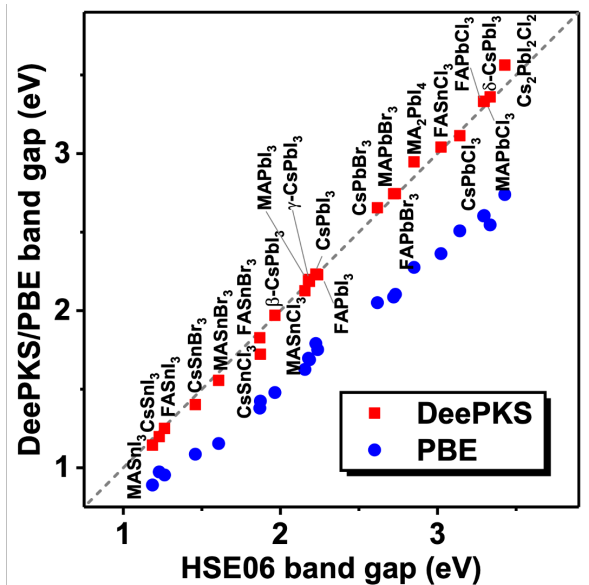

FIG. 25: Band gaps predicted by DeePKS and PBE with respect to the HSE06 results for all tested perovskites.[216] All tested non-hybrid perovskites are cubic phase except for those indicated by Greek letters. (Adapted with permission from J. Phys. Chem. C 127, 18755–18764 (2023). Copyright 2023 American Chemical Society.)

Evidently, the DeePKS model outperforms the DeePMD model with fewer frames as shown in Fig. 26. Additionally, the DeePKS model has a smaller generalization gap than the DeePMD model. Also, the DeePKS model can accurately replicate the SCAN0 SCF result for 64 water molecules in just fifteen minutes, significantly improving from the original time of over a day[45].

The work[45] also showed that excellent agreement can be achieved between the ABACUS-DeePKS-DeePMD results and the ones from SCAN or SCAN0-based DeePMD simulations. By labeling fewer than 200 frames in the training set with hybrid meta-GGA SCAN0 or meta-GGA SCAN functionals, they have shown that the GGA-based DeePKS model can effectively reproduce the energies and forces for pure and salt water systems, with considerable time savings. SCF calculations with trained DeePKS models were carried out and utilized as labels for DeePMD training. Liquid water's structural properties, such as radial distribution function (RDF), bulk density, H-bonds, and dynamic properties like diffusion coefficient, were found to be excellently matched with those obtained by the SCAN0 AIMD and DeePMD methods. For example, for systems consisting of 64 water molecules, they trained a DeePKS model with 180 training samples at the accuracy of SCAN0. Then, they used it to quickly develop 1000 data for training DeePMD potential and performed MD of 512 water molecules. As shown in Fig. 27, various radial distribution functions (RDFs) derived from DeePKS-DeePMD simulations exhibit remarkable consistency with both the SCAN0-AIMD and SCAN0-DeePMD results, including a marked decrease in overstructured peaks.
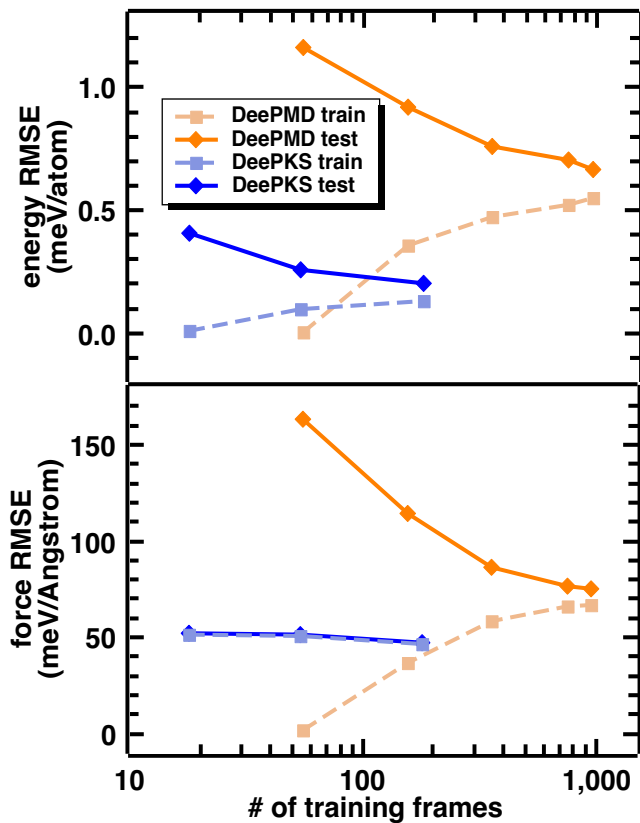
FIG. 26: Learning curves for energy (upper panel) and force (lower panel) given by DeePMD (orange) and DeePKS (blue) with respect to the number of training frames.[45] Dashed line with squares indicates train set error; solid line with diamonds indicates test set error. (Adapted with permission from J. Phys. Chem. A 2022, 126, 49, 9154–9164. Copyright 2022 American Chemical Society.)

Zhang *et al.*[217] investigated the tautomeric equilibria of glycine in water with the DeePMD model at the accuracy of M06-2X[218]. To avoid expensive computational cost for directly generating dataset at M06-2X level, they utilized the DeePKS method as implemented in ABACUS and DeePKS-kit, together with on-the-fly probability enhanced sampling (OPES)[219] method, to construct the dataset for training the DeePMD model. With this DeePMD potential and OPES, they performed MD and got a converged free energy surface (FES). They observed that glycine can undergo tautomerism, transitioning between its neutral and zwitterionic forms through intramolecular and intermolecular proton transfers. In[220], Zhang *et al.* adopted a similar strategy to study the propensity of water self-ions at air(oil)-ater interface. They found that the trained DeePKS model can decrease calculation time by about nine times compared to regular M06-2X calculations. With the resulting DeePMD model for an efficient MD process, they demonstrated the stable ionic double-layer distribution near the interface for both air-water and oil-water interface systems.

G. DFT+U

While DFT employing LDA or GGA functionals can often predict ground-state properties of various systems with reasonable accuracy, it falls short for strongly correlated materials, such as transition metal oxides and rare-earth compounds. In these cases, the simplified exchange-correlation functional does not adequately represent complex electron interactions, resulting in inaccuracies in predicted properties such as energy band gaps, magnetic moments, and orbital polarization, etc. The DFT+U method[74–78] improves the description for strongly correlated electronic systems by adding a Hubbard-U term with computational expenses comparable to those of LDA or PBE functionals.

ABACUS incorporates two distinct implementations of the DFT+U methods with NAOs basis. The primary distinction between these two methodologies lies in the way to project the electron density onto localized states, which is a critical step in accurately capturing the effects of strong electron-electron interactions within certain atomic orbitals.

The general energy functional that forms the foundation of the DFT+U method within ABACUS is initiated as

$$E_{\text{LDA+U}}[\rho] = E_{\text{LDA}}[\rho] + E_{\text{Hub}}\left[\left\{n_m^{I\sigma}\right\}\right] - E_{\text{DC}}\left[\left\{n^{I\sigma}\right\}\right], \tag{110}$$

and the fully-localized-limit (FLL)[77] double-counting scheme assumes that the on-site Coulomb interactions of localized electrons are fully accounted for by the Hubbard-U term, subtracting a mean-field average to avoid overestimating these interactions:

$$E_U\left[\left\{n_{mm'}^{I\sigma}\right\}\right] = \frac{U}{2}\sum_{I}\sum_{m,\sigma}\left\{n_{mm}^{I\sigma} - \sum_{m'}n_{mm'}^{I\sigma}n_{m'm}^{I\sigma}\right\}, \tag{111}$$

where the U value represents an empirically adjusted Coulomb penalty specifically applied to localized electrons, aiming to correct the underestimation of electron-electron repulsion within standard DFT calculations. The most critical quantity in the above expression is the on-site density occupancy matrix $n_{mm'}^{I\sigma}$, whose implementation is different among DFT software packages. In general, it can be expressed by introducing a local projection operator $\hat{P}_{\alpha mm'}^{\sigma} = |\alpha_m^I\sigma\rangle\langle\alpha_m^I\sigma|$ with orbital α at the site I and density matrix $\hat{\rho}$

$$n_{\alpha mm'}^{I\sigma} = \langle\alpha m\sigma|\hat{\rho}|\alpha'm\sigma\rangle = \text{Tr}(\hat{\rho}\hat{P}_{\alpha mm'}^{I\sigma}). \tag{112}$$

1. Dual Projection Method

The dual project method implemented in ABACUS[27] adopts the Mulliken charge projector to construct the on-site density occupancy matrix[221]. This projector transforms the Kohn-Sham orbital space into a localized and correlated subspace by utilizing the NAO basis, such as the d or f orbitals. The Mulliken charge projector meets the sum rule, ensuring the conservation of total electronic charges when summing over all projected channels.
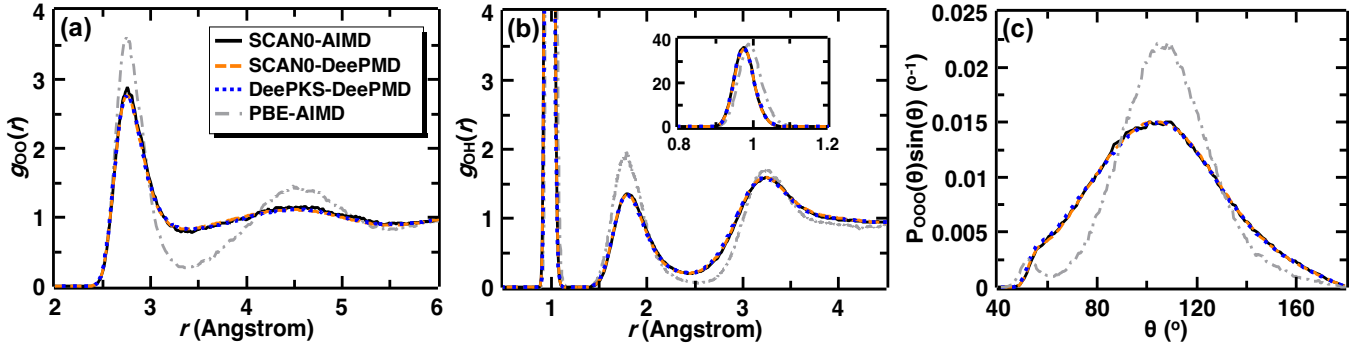
FIG. 27: Radial distribution functions (RDFs) **(a)** $g_{OO}(r)$, **(b)** $g_{OH}(r)$, and **(c)** bond angle distribution $P_{OO}(\theta)$ given by DeePKS-DeePMD (blue dotted line), SCAN0-AIMD (black solid line), SCAN0-DeePMD (orange dashed line), and PBE-AIMD (gray dotted-dashed line).(Adapted with permission from J. Phys. Chem. A 2022, 126, 49, 9154–9164. Copyright 2022 American Chemical Society.)

The Mulliken charge projector is defined as

$$
\begin{aligned}
\hat{P}^{\sigma}_{I,mm'} = \frac{1}{4N_k}\sum_{\mathbf{k}} \big(& |\tilde{\phi}_{\mathbf{k},\beta m'\sigma}\rangle\langle\phi_{\mathbf{k},\beta m\sigma}| + |\phi_{\mathbf{k},\beta m'\sigma}\rangle\langle\tilde{\phi}_{\mathbf{k},\beta m\sigma}| \\
& + |\tilde{\phi}_{\mathbf{k},\beta m\sigma}\rangle\langle\phi_{\mathbf{k},\beta m'\sigma}| + |\phi_{\mathbf{k},\beta m\sigma}\rangle\langle\tilde{\phi}_{\mathbf{k},\beta m'\sigma}| \big),
\end{aligned}
\tag{113}
$$

where N_k is the number of k points in the Brillouin zone. $\phi_{\mathbf{k},\beta m\sigma}$ and $\tilde{\phi}_{\mathbf{k},\beta m\sigma}$ are the original and dual orbitals, respectively. β groups the indices I,l,ζ with l and ζ belonging to the correlated channel of the correlated atom I.

This method is also referred to as the "dual" orbitals[221] approach due to its foundational reliance on the concept of dual orbitals, which are orthogonal to each other. This method introduces a set of dual orbitals mathematically derived from the original atomic orbitals, ensuring a biorthogonal relationship between them. The dual orbitals are defined in terms of the original atomic orbitals as

$$
\tilde{\phi}_{\mathbf{k}\mu}(\mathbf{r}) = \sum_{\nu} \phi_{\mathbf{k}\nu}(\mathbf{r})S^{-1}_{\nu\mu}(\mathbf{k}),
\tag{114}
$$

where μ is the index for dual orbital and $\mathbf{k}$ is wave vector. $\phi_{\mathbf{k}\nu}(\mathbf{r})$ is the original atomic orbital. $S_{\mu\nu}(\mathbf{k})$ is the overlap matrix in reciprocal space with $S^{-1}_{\nu\mu}(\mathbf{k})$ being its inverse.

The overlap matrix $S_{\mu\nu}(\mathbf{k})$ is given by

$$
S_{\mu\nu}(\mathbf{k}) = \langle\phi_{\mathbf{k}\mu}|\phi_{\mathbf{k}\nu}\rangle = \sum_{\mathbf{R}} e^{-i\mathbf{k}\cdot\mathbf{R}}\langle\phi_{\mathbf{R}\mu}|\phi_{0\nu}\rangle,
\tag{115}
$$

where $\mathbf{R}$ denotes the lattice vectors in the unit cell. $\phi_{\mathbf{R}\mu}(\mathbf{r})$ is a NAO centered on the a-th atom within the unit cell $\mathbf{R}$. The biorthogonality relation between the dual and original Bloch orbitals is

$$
\langle\phi_{q\mu}|\tilde{\phi}_{\mathbf{k}\nu}\rangle = \delta_{kq}\delta_{\mu\nu}.
$$

The spin-dependent on-site density occupancy matrix is defined by dual orbitals

$$
\begin{aligned}
n^{\sigma}_{I,mm'} = \frac{1}{4N_k}\sum_{\mathbf{k}} \bigg(& \sum_{S\beta m,\mu} S_{\beta m,\mu}(\mathbf{k})\rho^{\sigma}_{\mu,\beta m'}(\mathbf{k}) \\
& + \rho^{\sigma}_{\beta m,\mu}(\mathbf{k})S_{\mu,\beta m'}(\mathbf{k}) \\
& + S_{\beta m',\mu}(\mathbf{k})\rho^{\sigma}_{\mu,\beta m}(\mathbf{k}) \\
& + \rho^{\sigma}_{\beta m',\mu}(\mathbf{k})S_{\mu,\beta m}(\mathbf{k}) \bigg),
\end{aligned}
\tag{116}
$$

where the Kohn-Sham density matrix is

$$
\rho^{\sigma}_{\mu\nu}(\mathbf{k}) = \sum_{n} f_{\sigma n} c_{\sigma n,\mu} S_{\mu\nu}(\mathbf{k}) c^{*}_{\sigma n,\nu},
\tag{117}
$$

and the effective single-particle potential is

$$
\Delta V_{\sigma I,mm'} = \bar{U}_I \left(\frac{1}{2}\delta_{mm'} - n_{\sigma I,mm'}\right).
\tag{118}
$$

where $\bar{U}_I = U_I - J_I$ is the effective interaction parameter on the correlated atom I.

The Hamiltonian related to the DFT+U method is expressed by

$$
\begin{aligned}
\Delta V^{\mathbf{k}\sigma}_{\text{eff},\mu\nu} &= \langle\phi_{\mathbf{k}\mu}|\Delta\hat{V}^{\mathbf{k}\sigma}_{\text{eff}}|\phi_{\mathbf{k}\nu}\rangle \\
&= \frac{1}{4}\sum_{Imm'}\Delta V^{\sigma}_{Imm'}\Big(S^{(\mathbf{k})}_{\beta m,\nu}\delta_{\mu,\beta m'} + S^{(\mathbf{k})}_{\mu,\beta m'}\delta_{\beta m,\nu} + \\
& \quad S^{(\mathbf{k})}_{\beta m',\nu}\delta_{\mu,\beta m} + S^{(\mathbf{k})}_{\mu,\beta m}\delta_{\beta m',\nu}\Big),
\end{aligned}
\tag{119}
$$

$f_{\sigma n}$ is the occupation number, and $c_{\sigma n,\mu}$ are the Kohn-Sham eigenvectors. N_k is the number of kpoints in the Brillouin zone.

For the sake of simplicity, only the single-spin index case of collinear spin is mentioned. The detailed expressions for the corrections to atomic forces and stresses and the non-collinear spin cases can be found in Ref. 27.

2. Full Projection Method

The dual-orbitals method is a robust and efficient DFT+U method. However, using a subset of NAOs as projection operators in the DFT+U method may lead to a significant basis set dependence for the U term. For example, large radius cutoffs for may lead to inadvertently description for localized electron characteristics. An alternative method involves the modulation of NAOs to construct localized projection operators is proposed and has been integrated in ABACUS since v3.6.

In the demarcation of atomic localized information, it is common practice to employ spherical truncation via the empirical setting of atomic radius. This approach systematically transforms the problem into one of modulating orbitals from NAOs relative to a predetermined atomic radius. Concurrently, this must conform to three imperative criteria: first, close correspondence with the original numerical orbitals must be ensured; second, the orbitals must satisfy the normalization condition; and third, sufficient smoothness at the cutoff of the atomic radius must be ensured.

We apply a direct truncation for the tail of the radial function $\chi(r)$ of original NAOs, followed by a normalization procedure. The parameter σ controls the smoothing interval. A normalized function truncated at r_c can be expressed in the following form

$$
\alpha(r) = \left. \frac{\chi(r)g(r;\sigma)}{\langle \chi(r)g(r;\sigma)|\chi(r)g(r;\sigma)\rangle} \right|_{\frac{\partial \langle \alpha | \chi \rangle}{\partial \sigma} = 0}
$$

$$
g(r;\sigma) = \begin{cases} 1 - \exp\left(-\frac{(r-r_c)^2}{2\sigma^2}\right) & r < r_c \\ 0 & r \geq r_c \end{cases}. \quad (120)
$$

Iteratively determining the value of σ to solve for the modulation of orbitals such that the two-center integral results of the modulated $\alpha(r)$ and original $\chi(r)$ orbitals are maximized, σ_0 is thus ascertained to generate the target orbitals $\alpha_0(r)$.

The expression for the on-site density occupancy matrix is obtained through the full projection operator $\mathbf{P}$ in real space[221] using Kohn-Sham density matrix in real space $\rho_{\mu\nu}^{\mathbf{R}\sigma}$ as follows

$$
n_{mm'}^{I\sigma} = \sum_{\mathbf{RR}'} \sum_{\mu\nu} \rho_{\mu\nu}^{\mathbf{R}\sigma} \langle \phi_\mu^0 | \alpha_m^{I\mathbf{R}'} \rangle \langle \alpha_{m'}^{I\mathbf{R}'} | \phi_\nu^{\mathbf{R}} \rangle. \quad (121)
$$

The contribution of the DFT+U method to the real-space Hamiltonian takes the form of

$$
\begin{aligned}
V_{\mu\nu}^{U\sigma}(\mathbf{R}) &= \frac{\partial E_U \left[\{ n_{mm'}^{I\sigma} \} \right]}{\partial \rho_{\mu\nu}(\mathbf{R})} \\
&= \sum_I \sum_{mm'} \frac{\partial E_U \left[\{ n_{mm'}^{I\sigma} \} \right]}{\partial n_{mm'}^{I\sigma}} \frac{\partial n_{mm'}^{I\sigma}}{\partial \rho_{\mu\nu}(\mathbf{R})} \\
&= \sum_I \sum_{mm'} \Delta V_{Imm'}^{\sigma} \sum_{\mathbf{R},\mathbf{R}'} \langle \phi_\mu^0 | \alpha_m^{I,\mathbf{R}'} \rangle \langle \alpha_{m'}^{I,\mathbf{R}'} | \phi_\nu^{\mathbf{R}} \rangle.
\end{aligned} \quad (122)
$$

The full projection DFT+U method based on modulated atomic orbitals enables a focused approach to localized charges, offering enhanced numerical stability, while the adjustable projection orbital radii provide users with the flexibility to tailor the method for various application scenarios.

We provide benchmarks of the DFT+U with full projection method for the MnO, CoO, FeO, and NiO systems. All calculations are utilized by ABACUS v3.8 with the optimized norm-conserving Vanderbilt (ONCV) pseudopotentials with SG15-v1.0 version, in conjunction with an advanced double-ζ plus polarization (DZP) atomic basis. This basis set incorporates a radial cutoff of 9.0 bohr for transition metal (TM) elements and 7.0 bohr for oxygen atoms. For these calculations, the Brillouin zone discretization kspacing is 0.15 bohr^{-1} and the energy cutoff is 100 Ry.

TABLE I: Band gaps (in eV) and atomic magnetism (in μ_B) with format "value of band gap (value of atomic magnetic of Mn/Co/Fe/Ni)" of MnO, FeO, CoO, and NiO as a function of effective on-site Coulomb energy $\bar{U}$ (in eV). The experimental values are presented in the last row.

$\bar{U}$ (eV)	MnO	CoO	FeO	NiO
0.0	0.00 (4.64)	1.04 (2.46)	0.00 (3.54)	0.83 (1.33)
1.0	0.54 (4.71)	1.30 (2.56)	0.00 (3.61)	1.37 (1.44)
2.0	1.31 (4.76)	1.52 (2.62)	1.01 (3.68)	1.83 (1.52)
3.0	2.01 (4.80)	1.71 (2.67)	1.38 (3.74)	2.25 (1.58)
4.0	2.45 (4.84)	1.86 (2.72)	1.93 (3.78)	2.63 (1.63)
5.0	2.63 (4.87)	1.99 (2.76)	2.28 (3.82)	3.01 (1.67)
6.0	2.77 (4.90)	2.10 (2.79)	2.48 (3.86)	3.23 (1.71)
Exp.	$3.6 - 3.8$ (4.58)	2.4 (3.8)	2.4 (3.32)	4.0/4.3 (1.90)

a) MnO: $3.6 - 3.8$ eV (Ref. 222) and 4.58 μ_B (Ref. 223)
b) CoO: 2.4 eV (Ref. 224) and 3.8 μ_B (Ref. 225)
c) FeO: 2.4 eV (Ref. 226) and 3.32 μ_B (Ref. 227)
d) NiO: 4.0 eV (Ref. 228)/4.3 eV (Ref. 229) and 3.32 μ_B (Ref. 230)

Table I shows the band gap and atomic magnetism of TMOs with different values of $\bar{U}$. It is specified that all four TMOs manifest a rhombohedral unit cell embracing a type-II antiferromagnetic structure. Lattice parameters for MnO, FeO, CoO, and NiO are used from Ref 231, namely 4.445 Å, 4.334 Å, 4.254 Å, and 4.171 Å, respectively. The antiferromagnetic (AFM) state is postulated to align along the [111] direction. We perform these calculations by Perdew-Burke-Ernzerhof functional[58] with a Hubbard U correction, while neglecting the spin-orbit coupling (SOC) effect. Comparative results are utilized by various DFT softwares[27], including VASP, Wien2k, and Quantum ESPRESSO. As is shown in Fig. 28, the effect of U correction in ABACUS is notably consistent with other softwares. The agreement of our results with experimental ones proves the method's validity and its applicability in condensed matter physics and material sciences.

H. Real-Time Time-Dependent DFT

Density functional theory effectively predicts ground-state properties, like bond lengths, but struggles with excited states. For instance, DFT often underestimates semiconductor band gaps compared to experimental values due to insufficient treatment of electron-hole interactions and screening effects.[232]
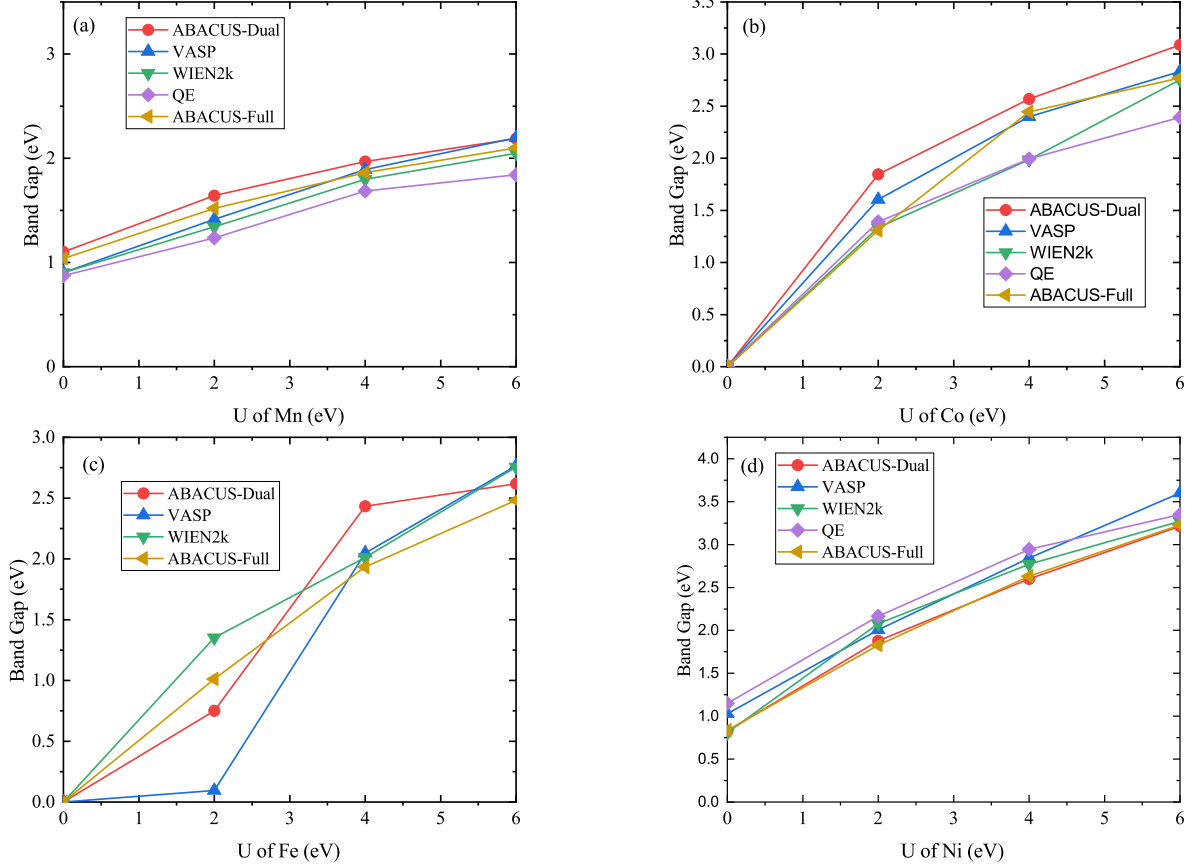
FIG. 28: The band gaps of transition metal monoxide MnO (a), FeO (b), CoO (c), and NiO (d) as influenced by the Hubbard U parameter, utilizing a rhombohedral unit cell with a type-II antiferromagnetic structure. "ABACUS-Full" presents results from the full projection method. For comparative analysis, PBE+U results for other computational methods are from Ref. 27.

A more accurate theory for simulating excited states was developed by Runge and Gross[233], which is named time-dependent density functional theory (TDDFT). Real-time TDDFT (rt-TDDFT) can investigate electron dynamics, such as optical absorption spectra[234], stopping power[235], photo-catalysis[236], and field-induced transitions. However, its computational intensity makes it challenging for large systems. Thus, employing numerical atomic orbital basis sets is advantageous, as they significantly reduce the computational burden while allowing for detailed analysis of excited-state phenomena and their intricate behaviors.[237]

The propagation of electrons obeys the time-dependent Kohn-Sham (TD-KS) equation:

$$i \frac{\partial}{\partial t} \psi_j(\mathbf{r},t) = \hat{H}_{KS}[n(\mathbf{r},t)] \psi_j(\mathbf{r},t). \quad (123)$$

The adiabatic approximation is applied, so the Hamiltonian depends only on the instantaneous charge density. For numerical atomic orbitals, the TD-KS equation can be expressed in matrix form[238]:

$$i \frac{\partial \mathbf{c}}{\partial t} = S^{-1} H \mathbf{c}. \quad (124)$$

where S represents the overlap matrix, and $\mathbf{c}$ is the column vector of coefficients for the local basis. For simplicity, the subscripts denoting the band index and $\mathbf{k}$-points have been omitted.

In ABACUS, we use the Crank-Nicolson method to approximate the propagator:

$$\mathbf{c}(t+\mathrm{d}t) = \frac{S(t+\mathrm{d}t/2) - i\hbar H(t+\mathrm{d}t/2)\mathrm{d}t/2}{S(t+\mathrm{d}t/2) + i\hbar H(t+\mathrm{d}t/2)\mathrm{d}t/2} \mathbf{c}(t), \quad (125)$$

where $S(t+\mathrm{d}t/2)$ and $H(t+\mathrm{d}t/2)$ are calculated using a linear approximation. Since $H(t+\mathrm{d}t/2)$ depends on $\mathbf{c}(t+\mathrm{d}t)$, a self-consistent procedure is needed to perform the propagation.

Ehrenfest dynamics is adopted for ion-electron coupled systems. The Verlet algorithm is employed to calculate the ionic velocities and positions at each time step. Fig. 29 shows a basic procedural flowchart of the rt-TDDFT algorithm in ABACUS.

The intensity of optical absorption spectra can be expressed as the imaginary part of the dielectric function:

$$S(\omega) = \frac{2\omega}{3\pi} \mathrm{Im}\{\mathrm{tr}(\alpha_{\mu,\mu}(\omega))\}, \quad (126)$$
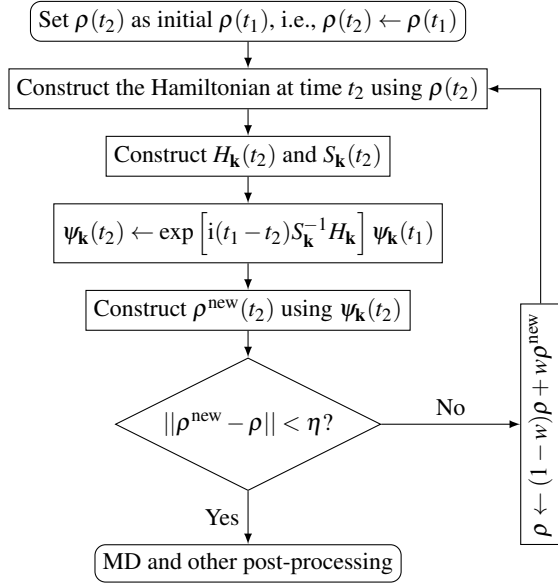
FIG. 29: Flowchart of the rt-TDDFT algorithm in ABACUS. It is worth noting that the self-consistent iteration of the electron density $\rho(t)$ ensures stability, with convergence criteria $||\rho^{\text{new}} - \rho|| < \eta$. The final stage involves post-processing, calculating quantities like total energy using Harris functional, and extracting physical observables.

and the dielectric function can be calculated through the change in the dipole moment P_μ induced by the external laser field:

$$\alpha_{\mu,\nu}(\omega) = \frac{\int P_\mu(t) e^{i\omega t}\, dt}{\int E_\nu(t) e^{i\omega t}\, dt}. \tag{127}$$

Different electric fields in the time domain are provided in ABACUS, such as the Heaviside step function and Gaussian function. A Gaussian-type electric field is often used:

$$E(t) = E_0 \cos(2\pi f t + \phi) \exp\left(-\frac{(t - t_0)^2}{2\sigma^2}\right). \tag{128}$$

The Hamiltonian, including electric fields, has two forms: length gauge and velocity gauge. Within the length gauge, the extra Hamiltonian term is V_{ext}:

$$V_{\text{ext}} = e\mathbf{E}(t) \cdot \mathbf{r}. \tag{129}$$

However, due to the periodic nature of the unit cell, this method will break the translational invariance of the electric potential. To address this, a sawtooth field in the spatial domain is used:

$$E_\mu(x_\mu, t) = \begin{cases} E_\mu(t), & \varepsilon < x_\mu < L_\mu - \varepsilon, \\ -E_\mu(t)(L_\mu - 2\varepsilon)/2\varepsilon, & -\varepsilon < x_\mu < \varepsilon, \end{cases} \tag{130}$$

where $\mu = x, y, z$, L_μ is the length of the unit cell along μ, and $\varepsilon \to 0$. To avoid divergence, the charge density must vanish in the region $-\varepsilon < x_\mu < \varepsilon$. Ideally, this region should be set as
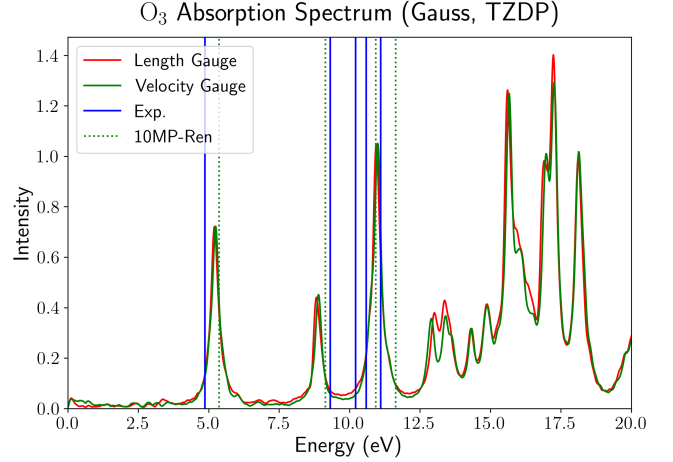

FIG. 30: Optical absorption spectra of the ozone molecule calculated using real time TDDFT in ABACUS. The results obtained using the length gauge and velocity gauge are consistent with each other and show reasonable agreement with experimental data[239] and ab initio results from SIESTA[234].

a vacuum layer. Therefore, the length gauge can only be used for finite systems theoretically.

Another method is the velocity gauge, which introduces a vector potential to simulate the laser field:

$$\mathbf{A} = -c \int \mathbf{E}\, dt. \tag{131}$$

Therefore, the kinetic term of the velocity-gauge Hamiltonian becomes

$$H_{\mathbf{k}} = \frac{1}{2m}\left(\hbar\mathbf{k} - \frac{e}{c}\mathbf{A}\right)^2. \tag{132}$$

Below, we had a benchmark calculation for the optical absorption spectra of an ozone molecule (O_3). The results are shown in Fig. 30.

Under normal temperature and pressure conditions, the electronic excitation energy is much smaller than the semiconductor band gap or chemical bond dissociation energy. The conventional Born-Oppenheimer molecular dynamics can be used in such cases. However, when electrons are excited by high-energy photons or extremely high temperatures, there is a strong coupling between electron motion and atomic nucleus motion, causing the Born-Oppenheimer approximation no longer valid. Typical applications include light-matter interactions and warm dense matter. TDDFT as an excitation state calculation method, can achieve high computational accuracy by choosing appropriate exchange-correlation potentials. It is widely used in areas such as light-controlled material phase transitions[240], time-dependent evolution of excited-state quasi-particles[241], and photochemical reaction mechanism analysis[242].

In photocatalysis, the timescale of electron motion typically ranges from femtoseconds (fs) to picoseconds (ps). For example, the lifetime of hot electrons captured by wet electron

states on TiO_2 surfaces, where water molecules are adsorbed, is usually less than 15 fs[243]. Correspondingly, the chemical reactions driven by photogenerated carriers also occur within the fs to ps timescale. Photocatalysis can also induce localized hotspot effects, significantly impacting product selectivity and efficiency. The interaction among photons, phonons, and molecules at single-atom sites is crucial for understanding energy conversion efficiency and molecular reaction selectivity in practical photocatalytic systems.

Focusing on the photocatalysis, Liu *et al.*[236] studied the dissociation process of water molecules under thermal and photoexcitation conditions using Ni single atoms supported on CeO_2, based on the TDDFT functionality of ABACUS, as shown in Fig. 31. The ground-state electronic density shows that when water molecules adsorb on Ni single atoms, due to the presence of oxygen-rich defects, the anti-bonding state formed by the hybridization of the Ni atom d orbitals and H_2O molecular orbitals is occupied (Fig. 31a), leading to weak adsorption strength of H_2O and a correspondingly low dissociation barrier. Under thermal excitation at 600 K, H_2O dissociates into H and OH, causing the oxygen vacancies near the Ni exposure site to be covered by OH, which in turn deactivates the catalyst. However, under photoexcitation, the Ni atom site accumulates holes transferred to the H_2O molecule, weakening the adsorption between Ni and H_2O. As a result, the dissociation of H_2O to form O does not fill the oxygen vacancies around the Ni site, ensuring the stability of the catalyst. This mechanism has also been confirmed experimentally.

In another study, Liu *et al.*[244] compared the dissociation of CO_2 driven directly by hot carriers generated via plasmonic excitation in metal clusters with the thermochemical reduction of CO_2 by H species. They used TDDFT to elucidate the mechanisms and characteristic timescales of both processes and provided experimental evidence from in situ infrared spectroscopy. Additionally, TDDFT is suitable for analyzing charge transfer pathways, proton-coupled electron transfer (PCET), plasmonic processes, and other phenomena in photocatalytic reactions.

FIG. 31: TDDFT applications on photocatalysis[236]. (a) Projected density of states for H_2O on Ni single atom site load on CeO_2. (b) Bond length of thermal dissociation of H_2O under 600 K. (c-d) Bond length of light-induced dissociation of H_2O. (Adapted with permission from Nat. Commun. 15, 4675 (2024). Copyright 2024 Springer Nature.)

VI. ABACUS IN THE OPENLAM PROJECT

As the collection of quantum mechanical data progressively encompasses the entire periodic table, the Deep Potential team has launched an ambitious project named the Large Atomic Model (LAM) based on the practice of DPA pre-training model[245,246]. Given its openness and the crucial role of transparency in its progress, we call it the OpenLAM project[46].

While extensive ab initio data repositories are available, precise sampling for specific application scenarios remains vital for the pursuit of the model's accuracy and transferability. To support the development of OpenLAM, the ABACUS team has launched the NOVA (Nourishing OpenLAM via ABACUS) project. This project is dedicated to supplying OpenLAM with affordable, high-precision first-principles data across diverse practical contexts. To this end, the ABACUS team help the users choose highly accurate pseudopotentials for various scenarios of OpenLAM through sys-
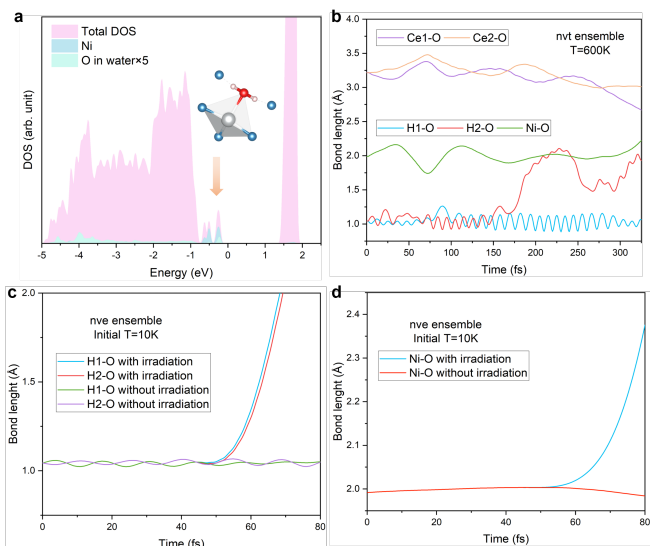
tematic precision testing, which will be introduced below in Sec. VI A. By implementing heterogeneous acceleration (Sec. IV B) and aggressively optimizing memory usage, along with economical hardware, the ABACUS team has significantly reduced the overall cost of data production. ABACUS has thus far generated a wealth of data in multiple application fields such as semiconductors, alloys, and Superhydrides to facilitate the ongoing refinement of OpenLAM within these sectors.

A. APNS Project

Advanced computational solid-state datasets developed in recent decades—such as Materials Project[247], Materials Cloud[248], and Computational Materials Repository[249]—extensive literature has clarified correct DFT practices and explored ways to fine-tune the balance between precision and efficiency. In recent years, professional discussions on how to validate DFT code implementations are becoming more prevalent[105,169,171,250]. A comprehensive and systematic verification of ABACUS remains essential. This measure is imperative to maintain efficient and reliable software development and, by extension, to guarantee optimal efficiency and precision in high-throughput computations.

Technically, contemporary DFT codes for periodic system calculations have greatly benefited from the pseudopotential formulation and the collaborative nature of open-source pseudopotential development. Numerous open-source codes for generating pseudopotentials have been released,

enabling users to tailor pseudopotentials to their specific requirements[184,251]. This customization also extends to the numerical atomic orbitals used in ABACUS for LCAO calculations. However, in practical DFT calculations, basis sets are ubiquitously employed to approximate physically acceptable functions—ranging from wavefunctions and charge densities to any function transitioning between real space and its Fourier-transformed counterpart. Thus, it is crucial to validate the size of basis as well as the quality of pseudopotentials and orbitals for particular systems before practical application, as those latter encapsulate atomic characteristics that indirectly influence critical physical properties of interest, such as elastic modulus and band gap, while the former controls the level describing atomic characters. We initiated the "ABACUS Pseudopotential Numerical Atomic Orbital Square" (APNS) project. This suite of workflows facilitates automated, high-throughput, and even user-interactive extended testings. It encompasses tests for pseudopotentials and numerical atomic orbitals across ideal, practical, or user-defined systems, accommodating both PW and LCAO calculations. Additionally, APNS is designed to offer a database where users can review test outcomes and download the appropriate pseudopotential and orbital files.

The systematic test workflow is depicted in Fig. 32. An additional front-end interface of this workflow is currently in development, the established back-end workflow has been employed to conduct efficiency and precision tests on a variety of norm-conserving pseudopotential sets. These pseudopotential sets include SG15[252], PseudoDojo[253], PD03[254], PD04[254] (along with their versions and semi-core configurations, where available), as well as certain Goedecker-Teter-Hutter pseudopotentials[255] utilized in CP2K, and three widely-used types of ultrasoft pseudopotentials (pslibrary 0.3.1 and 1.0.0[256], GBRV v1.5[257,258]). This workflow has also played a role in developing various ABACUS features, such as DFT+U and support for ultrasoft pseudopotentials.

As mentioned, the kinetic energy cutoff in plane-wave (PW) calculations is a major determinant of result precision, yet excessively high cutoff values are impractical for routine calculations. Therefore, tests were designed to find the best balance between efficiency and accuracy for each pseudopotential construction, family, and version. Technically, this involves conducting convergence tests on various parameters and performing Equation-of-States (EOS) tests using the converged cutoff values.

The kinetic cutoff energy of plane wave basis convergence tests are done on the most stable crystal phases collected from Materials Project[248], Crystallography Open Database (COD)[260], Optimade[259], etc. Keeping all other parameters unchanged, the value of cutoff varies from 20 to 300 Ry. For various kinds of pseudopotentials, the convergence of the PW kinetic energy cutoff is tested on three properties: Kohn-Sham energy, lattice pressure (trace of stress tensor) and a simplified version of band structure similarity[263]

$$\eta_v(A,B) = \sqrt{\frac{\sum_{n\mathbf{k}} \tilde{f}_{n\mathbf{k}}(e_{n\mathbf{k}}^A - e_{n\mathbf{k}}^B)^2}{\sum_{n\mathbf{k}} \tilde{f}_{n\mathbf{k}}}}, \qquad (133)$$
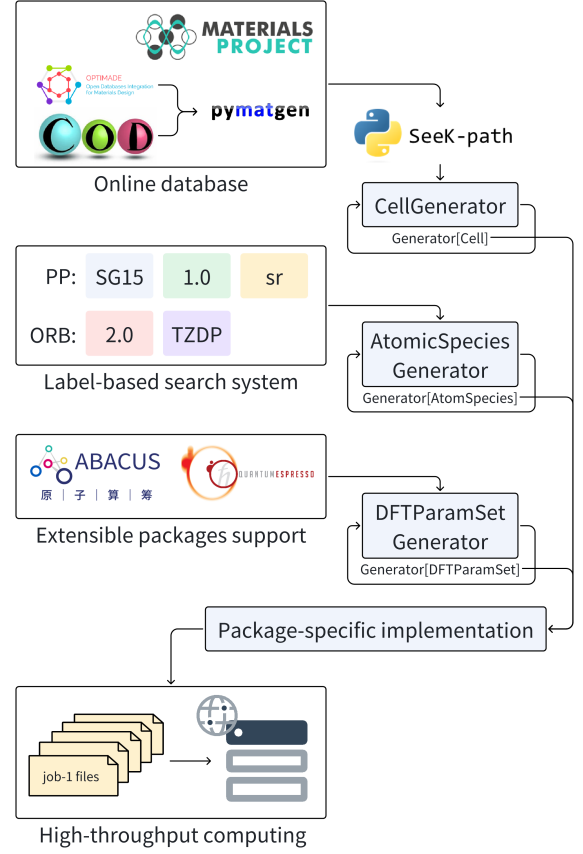

FIG. 32: Workflow-chart of ABACUS Pseudopotential-Numerical atomic orbital Square automatic, high-throughput workflow incorporating structure generation, download and management (interfaced with online open crystal structure databases Materials Project[247], Optimade[259], Crystallography Open Database (COD)[260], etc.), symmetry analysis (interfaced with SeeK-path[261,262]), modular and extensible software input generation (ABACUS and Quantum ESPRESSO[11]) and remote high-throughput computing support.

where $e_{n\mathbf{k}}^A$ is the energy of the n-th band at kpoint $\mathbf{k}$ of calculation with DFT setup A (so as for B), $\tilde{f}_{n\mathbf{k}} = \sqrt{f_{n\mathbf{k}}^A f_{n\mathbf{k}}^B}$, is the geometrical average occupation between calculation with two cutoff values.

EOS tests are done not-spin-polarized, with k-point being sampled with spacing 0.06 Bohr^{-1} in Brillouin zone for all elements. Volumes of crystal vary from 94% to 106% with step-size 2%. The kinetic energy cutoff of the PW basis is taken as the maximum among converged values of all elements involved in the system tested. Δ value[264], which is defined as,

$$\Delta(a,b) = \sqrt{\frac{1}{V_M - V_m} \int_{V_m}^{V_M} [E_a(V) - E_b(V)]^2 dV} \qquad (134)$$

is used as a scalar to indicate the difference between the EOS profile calculated by pseudopotential calculation and the all-electron one. The continuous integral in Eq. (134) is done on

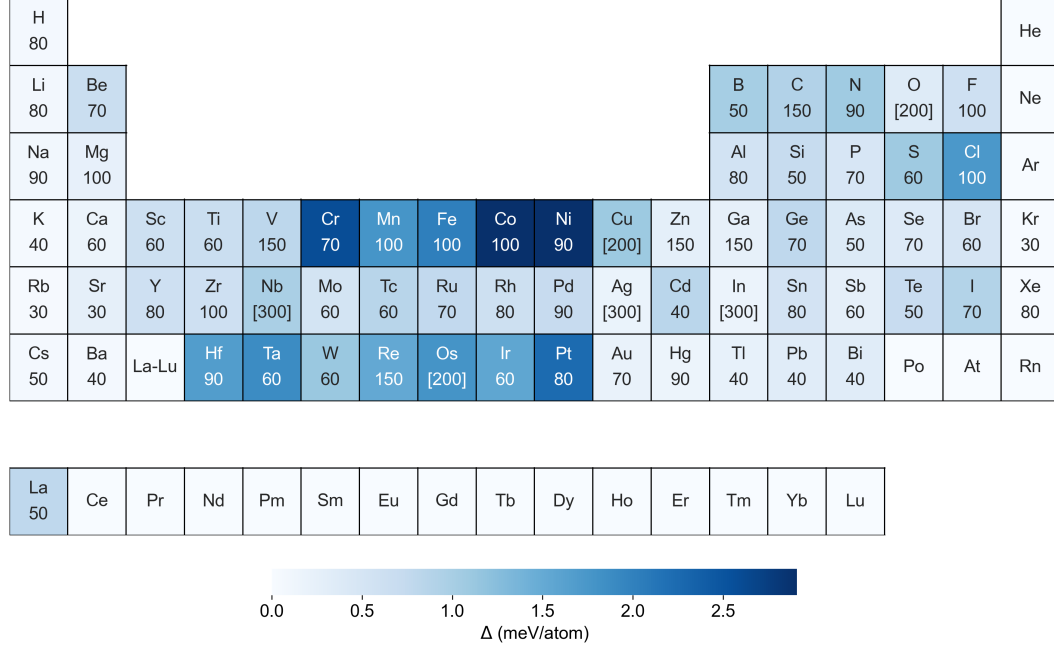Efficiency and precision test on SG15-1.0 pseudopotentials

FIG. 33: ABACUS PW calculation efficiency and precision tests on SG15 1.0 pseudopotentials. Number below the element symbol labels the converged kinetic energy cutoff (E_c^{kin}) under three thresholds: Kohn-Sham energy (< 1 meV/atom), pressure (< 0.1 kbar) and band similarity (< 10 meV). Large E_c^{kin} which are enclosed by brackets are result from the oscillation or slow convergence of pressure. Color of each block indicates the Δ value calculated with converged E_c^{kin} averaged over Bravais lattices BCC, FCC and Diamond. Blocks of elements whose pseudopotentials are not available are left empty.

the Birch-Murnaghan equation[265]

$$E(V) = E_0 + \frac{9V_0 B_0}{16}\left\{ \left[(\frac{V_0}{V})^{2/3} - 1 \right]^3 B_0' \right.$$
$$\left. + \left[(\frac{V_0}{V})^{2/3} - 1 \right]^2 \left[6 - 4(\frac{V_0}{V})^{2/3} \right] \right\} \tag{135}$$

fitted curve. In practical tests, we build three Bravais lattices, including BCC (Body-Centered-Cubic), FCC (Faced-Centered-Cubic) and diamond for each element, representing different coordination environments, calculate E-V datasets and make comparisons with the all-electron results reported in the works of Giovanni P. *et al.*[105]. The converged kinetic energy cutoff and Δ value calculated with it for all available elements in SG15 1.0 pseudopotential[184] are shown in Fig.33.

We perform precision tests on different sets of NAO basis. Similar to PW calculations, the precision is indicated by EOS; additionally, the energy difference of the lowest points of the EOS profile can be an indicator for basis set completeness.

For ABACUS LCAO calculations, the reliability verification test on any given pseudopotential is often slowed by relatively complicated and time-consuming NAOs generation procedure, in which sophisticated experience and insights may be of need, a rapid and highly-automated orbital generation code then becomes necessary. Plus, the precision and efficiency

of NAOs are expected to be improved successively, a platform for orbital generation algorithm development with reliable implementation, clear and stable interfaces between modules, high code readability of codes is need. Therefore, an open-source sub-project "ABACUS-ORBGEN" is included as a developing part of APNS. The developing implementation now is still based on the algorithms proposed in Refs. [20] and [26], but supports orbital configuration automatic setting for pseudopotentials generated with ONCVPSP codes, automatic orbital transferability improving by performing series of bond length scan and potential curve fitting tasks and a quick orbital quality estimation functionality.

B. UniPero Model

Wu *et al.*[266] utilized "modular development of deep potential" (ModDP)[267] to create a universal interatomic potential for perovskite oxides (UniPero) using a deep neural network with a self-attention mechanism. This potential spans 26 types perovskite oxides involving 200 components and 14 metal elements. All DFT calculations were performed with ABACUS. As depicted in Fig. 34(a), they first used DP-GEN to obtain a converged DPA-1 model[245] for three-element systems such as $PbTiO_3$, $SrTiO_3$. Then, the con-

verged dataset served as a starting point for DP-GEN to improve DPA-1 for four-element perovskite systems such as $Pb_xSr_{1-x}TiO_3$ and $PbZr_xTi_{1-x}O_3$. Ultimately, the final DPA-1 model (UniPero) can describe six-element perovskite systems, including the ternary solid solution $Pb(In_{1/2}Nb_{1/2})O_3$-$Pb(Mg_{1/3}Nb_{2/3})O_3$–$PbTiO_3$ (PIN-PMN-PT). UniPero functions as a universal interatomic potential, effectively modeling a wide range of perovskites through molecular dynamics simulations.

The $PbTiO_3/SrTiO_3$(PTO/STO) superlattices serve as a model system for exploring real-space topological textures, including flux closures, vortices, skyrmions, and merons. They tested the DPA-1 model by simulating strain-driven topological evolution in the PTO/STO superlattice. Fig. 34(b) illustrates a $40 \times 20 \times 20$ supercell, containing 80,000 atoms, employed to model a $(PTO)_{10}/(STO)_{10}$ superlattice. At a strain state where the in-plane lattice constants $a_{IP} = 3.937$ Å and $a_{IP} = 3.930$ Å, the equilibrium state at 300 K obtained with DPMD simulations adopts an ordered polar vortex lattice with alternating vortex and antivortex (Fig. 34(c)). As the in-plane strain increases to $a_{IP} = 3.950$ Å, the vortex cores shift toward the PTO/STO interfaces (Fig. 34(b)). Finally, at a large tensile in-plane strain ($a_{IP} = 3.955$ Å), it becomes the periodic electric dipole waves characterized by head-to-tail connected electric dipoles in the form of a sine function (Fig. 34(e)). These results agree with the experimental observations[268] and previous MD simulations[267].

C. DPA-Semi Model

Liu *et al.*[269] generated first-principles data for 19 bulk semiconductors ranging from group IIB to VIA, namely, Si, Ge, SiC, BAs, BN, AlN, AlP, AlAs, InP, InAs, InSb, GaN, GaP, GaAs, CdTe, InTe, CdSe, ZnS, CdS. They used the ABACUS v3.2 package based on the numerical atomic orbitals basis set with the Perdew-Burke-Ernzerhof (PBE)[58] exchange-correlation functional generated atomic datasets to reduce the production cost of the data. The triple-zeta plus double polarization (TZDP) numerical atomic orbitals basis sets were used for all DFT calculations. The atomic datasets are adopted as training data to generate an attention-based deep potential model using the DPA-1 method[245], namely the DPA-Semi model. Fig. 35 shows the procedures for developing the DPA-Semi model.

The total number of data sets generated for 19 semiconductors is around 200k frame. The energy RMSEs of the BAs system are the smallest, which is 0.004 eV/atom, and the force RMSEs of the InSb system are the smallest, which is 0.11 eV/Å. Ref. 269 exhibits the lattice constants and elastic moduli of 19 semiconductors from group IIB to VIA. The results obtained from the DPA-Semi models are in excellent agreement with the DFT results calculated by ABACUS. These results offer reliable evidence that the DPA-Semi models can be employed to study the physical mechanisms of group IIB to VIA semiconductor systems with ab initio accuracy. The DPA-Semi results of bulk modulus are in excellent agreement with other DFT results[269] and available experimental data (Fig. 36). This work provided reliable evidence that the DPA-Semi model can be readily employed to study the scientific issues of group IIB to VIA semiconductor systems with ab initio accuracy.

D. DPA-1 and DPA-2

The Deep Potential team has successively proposed large interatomic potential models like DPA-1[245] and DPA-2[246] since 2022. The DPA-1 model is a novel atomic model designed for molecular and materials simulation based on attention mechanism, which is trained on the public OC20 dataset and the materials such as aluminum-magnesium-copper alloys, high entropy alloys, and solid electrolytes. It is applicable to systems containing 56 different elements, and employs a strategy of pretraining combined with fine-tuning to adapt to practical application scenarios.

DPA-2[246] adopts a multitask training strategy, capable of optimizing datasets from different DFT parameters sources simultaneously. This effectively reduces the model's requirement for data quality, allowing datasets obtained from different software to be used in the same training process. Moreover, the design of the DPA-2 model enables it to acquire knowledge about chemical composition and configurations during the pretraining phase, which significantly decreases the amount of fine-tuning data needed for specific downstream tasks. In the development of DPA-2, the ABACUS software plays a significant role. It is employed in the DFT calculations for multiple datasets, such as Alloy, FerroEle, SemiCond and high-pressure SuperHydrides.

Alloy Based on DFT calculations performed using ABACUS, we are developing general LAMs for alloys, covering 53 elements in the periodic table (Li, Na, K, Be, **Mg**, Ca, Sr, Sc, **Y**, La, **Ti**, **Zr**, **Hf**, V, **Nb**, **Ta**, **Cr**, **Mo**, **W**, **Cu**, Ag, Au, **Zn**, Cd, **Mn**, **Re**, **Fe**, **Co**, **Ni**, Os, Ir, Pt, Rh, Ru, Pd, Ce, Pr, Nd, Sm, Gd, Tb, Dy, Ho, Er, Tm, Lu, **Al**, Ga, In, Si, Ge, Sn, Pb (bold ones are commonly used in structural alloys)). The specific pseudopotentials utilized for these elements are listed in[270] and we leveraged the acceleration feature of ABACUS on the Deep Computing Unit (DCU) for all DFT calculations. The DPGEN and APEX workflows generated various structures[271,272], including perfect and perturbed crystal structures, vacancies, interstitials, and surfaces of metals and alloys. Some structures were selected through the concurrent learning workflow in DPGEN and then labeled by ABACUS, resulting in a training dataset of ~24,000 entries. By integrating previous training datasets from AIS Square and previous OpenLAM[46], the latest general LAM for alloys achieved a root mean square error (RMSE) of ~26 meV/atom for energies and ~0.20 eV/Å for atomic forces across the 53 metals and their alloys. This general LAM for alloys demonstrates superior performance in predicting various properties, including lattice parameters, elastic constants, point defects, and surface formation energies, compared to other LAMs[273]. ABACUS has proven to be a stable and reliable DFT workhorse for diverse structures covering 53 elements and is computationally efficient, particularly on DCU machines.
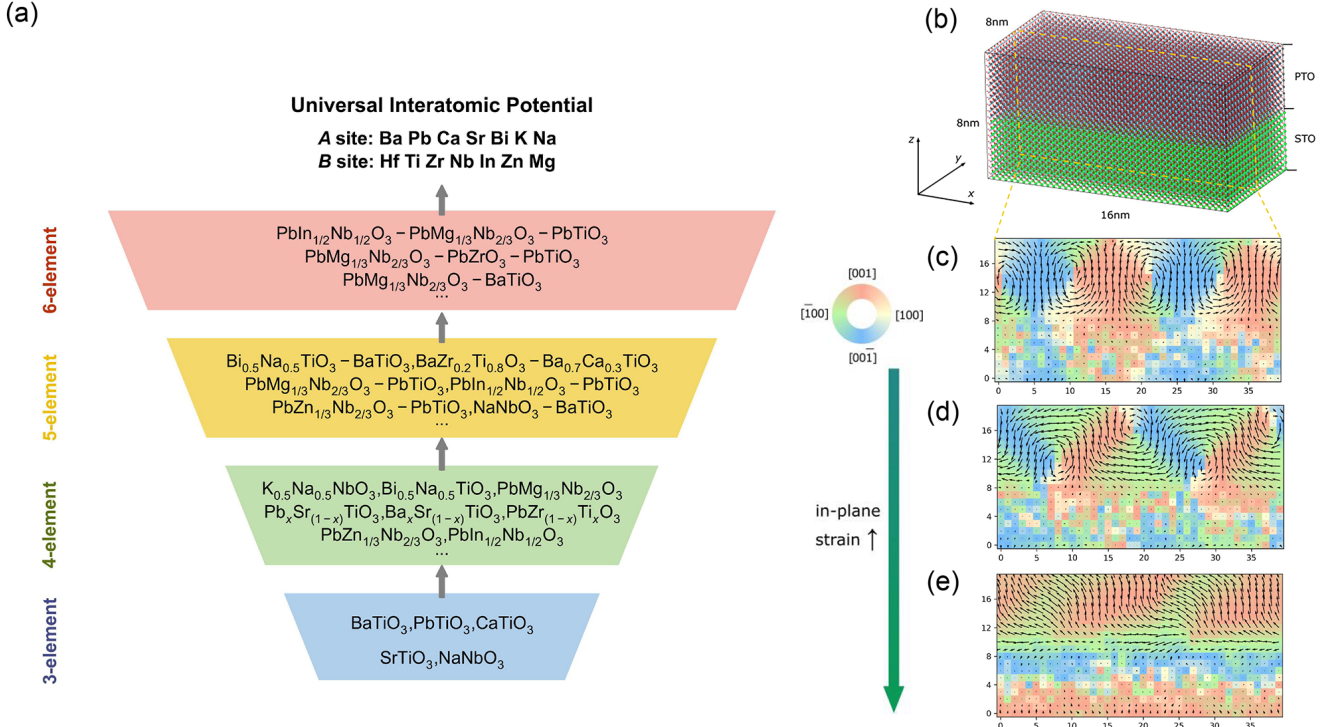
FIG. 34: (a) Workflow for developing a universal force field of perovskite oxides. (Adapted with permission from Phys. Rev. B 108, L180104 (2023). Copyright 2023 American Physical Society.) (b) $(PTO)_{10}/(STO)_{10}$ superlattices. Unipero predicts an in-plane strain-induced transition from (c) ordered polar vortex lattice to (d) shifted polar vortex lattice, and to (e) electric dipole waves.

high-pressure SuperHydrides During the construction of the dataset for the DPA-1 and DPA-2 models of high-pressure SuperHydrides, all labels were calculated using ABACUS software with plane-wave basis sets. The thermodynamic stability of the discovered structures was confirmed by their energy above the convex hull, which was determined through structure optimization results from ABACUS. Dynamic stability was assessed using the phonon dispersion spectrum calculated by phonopy[274,275], with all forces calculated by ABACUS. Our DFT calculations were performed on DCU clusters, significantly enhancing the efficiency of SCF calculations compared to traditional CPUs. We obtained a dataset comprising 218,349 data frames, covering 29 elements and a pressure range of 150-250 GPa. Utilizing this data, the DPA-1 model achieved a training Root Mean Square Error (RMSE) of 48.1 meV/atom for energy and 334.8 meV/Å for force. The DPA-2 model achieved a training Root Mean Square Error (RMSE) of 55.2 meV/atom for energy and 298.8 meV/Å for force. On the testing dataset, the DPA-1 model yielded an RMSE of 37.6 meV/atom for energy and 171.4 meV/Å for force, and the DPA-2 model yielded an RMSE of 37.4 meV/atom for energy and 122.1 meV/Å for force. Given the large dataset required for the Superhydrides model, ABACUS proved to be the most economical DFT software available. The high-quality training results further attest to the stable performance of ABACUS.

VII. INTERFACES TO OTHER PACKAGES

A. DeePKS-kit

The DeePKS-kit[36,37] is designed to train the DeePKS model and can be linked with ABACUS or PySCF[10]. In practice, the training of the DeePKS model is to optimize the following formula

$$\min_{\omega} \mathbb{E}_{\text{data}}[(E_{\text{label}} - \min_{\{\psi_i\}, \langle \psi_i | \psi_j \rangle = \delta_{ij}} E_{\text{DeePKS}}[\{\psi_i\}|\omega])^2].$$
(136)

Note that the energy functional E_{DeePKS} is determined by the parameters ω. When we want to calculate the difference between the label energy (E_{label}) and the ground state DeePKS energy at the specified parameters, we need to obtain it by minimizing the energy functional with respect to wave function $\{\psi_i\}$. In other words, every time the parameter is updated, we need to solve a SCF calculation, which is very time-consuming.

To avoid the above problem, we use the projection method to solve Eq. 136. We rewrite it as:

$$\min_{\omega} \mathbb{E}_{\text{data}}[(E_{\text{label}} - E_{\text{DeePKS}}[\{\psi_i\}|\omega])^2] \quad (137)$$
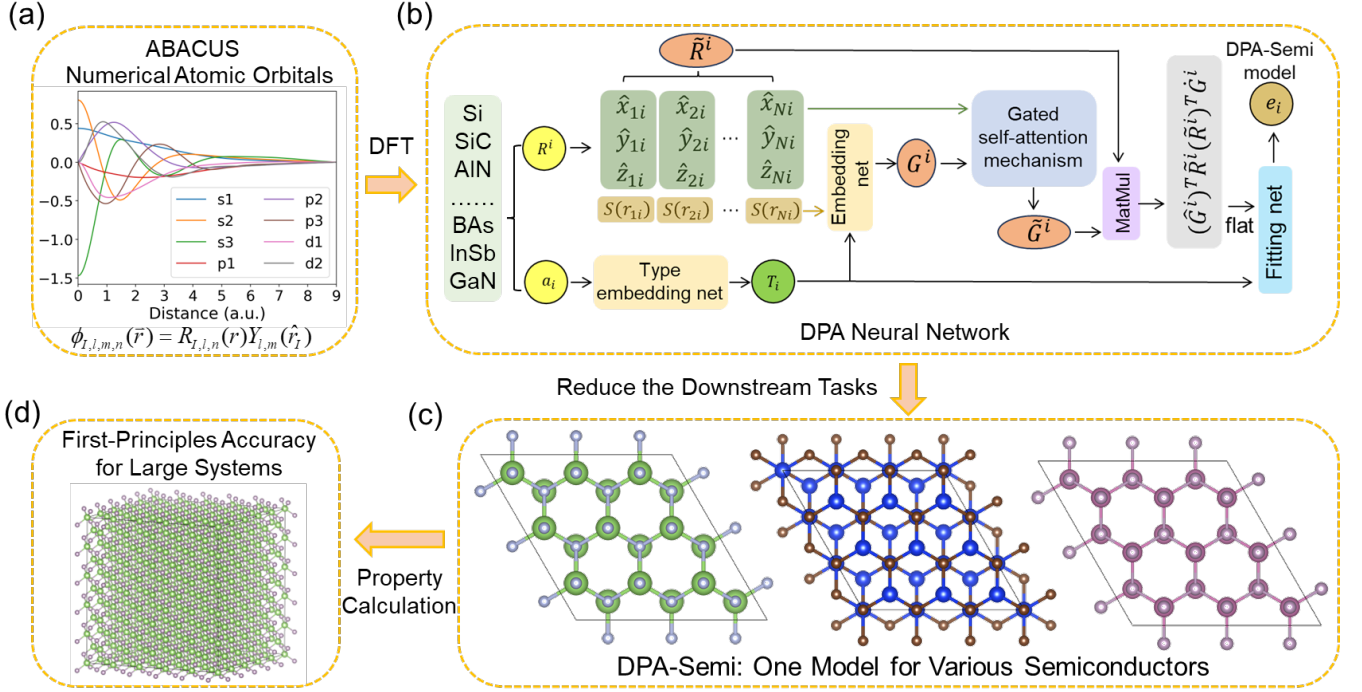
FIG. 35: Procedures for developing the DPA-Semi model. (a) Generate atomic datasets using the ABACUS package based on the numerical atomic orbitals as basis set; (b) Generate the DPA-Semi model via the Gated self-attention mechanism based on the DFT atomic datasets; (c) The DPA-Semi model can be used for various kinds of semiconductors, and reduce the computational costs of downstream tasks; (d) The DPA-Semi model is readily applied to calculate properties of large-systems with GGA quality accuracy. (Adapted with permission from J. Chem. Theory Comput. 2024, 20, 13, 5717–5731. Copyright 2024 American Chemical Society.)
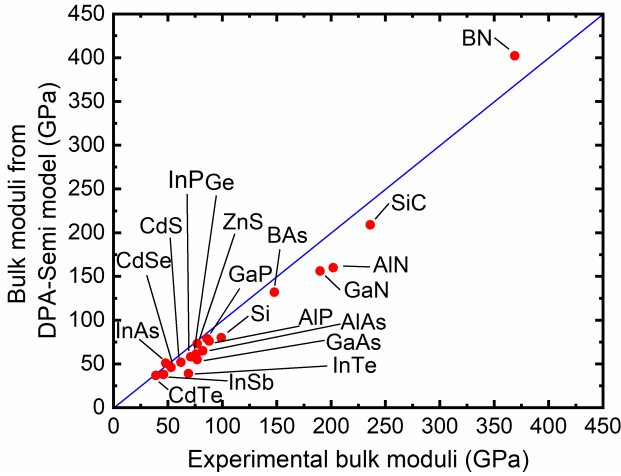

FIG. 36: Predicted bulk moduli of various semiconductors by the DPA-Semi model, and available experimental data. (Adapted with permission from J. Chem. Theory Comput. 2024, 20, 13, 5717–5731. Copyright 2024 American Chemical Society.)

$$\text{s.t. } \exists \varepsilon_i \leq \mu,$$
$$(H[\{\psi_i\}|\omega] - \varepsilon_i)|\psi_i\rangle = 0,$$
$$\langle \psi_i|\psi_j\rangle = \delta_{ij} \tag{138}$$
$$\text{for } i,j = 1...N.$$

In detail, we optimize the DeePKS model in two iterative steps. The first is the SCF step. Fix model parameters ω^*, and solve Kohn-Sham equation (Eq. 138) to get ground state $\{\psi_i^*\}$. We usually take ω^* as all zero when the whole training process starts. The second is TRAIN step. Fix orbitals $\{\psi_i^*\}$, and optimize model parameters ω following Eq. 137. This way, without the constraints, the optimization for neural network parameters ω can be carried out quickly. Then, we go back to the first step. We project the orbitals $\{\psi_i^*\}$ back to the subset that satisfies the constraints by solving the SCF equations. And then update ω. These two steps repeat until convergence is reached.[36]

We carry out TRAIN step in DeePKS-kit software[37], and SCF step in ABACUS. With periodic boundary conditions in ABACUS, we can train and apply DeePKS models in molecular systems and periodic systems. The iterative training process cooperated by DeePKS-kit and ABACUS is summarized in Fig. 37.
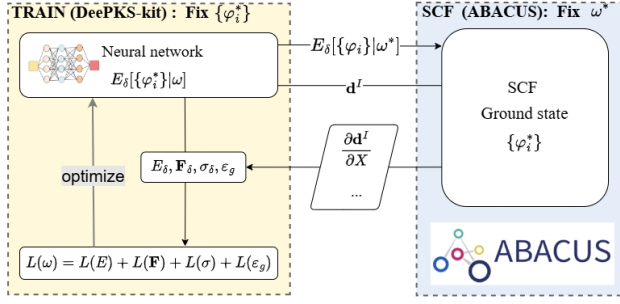
FIG. 37: Workflow of training a DeePKS model. The blue and yellow boxes represent the SCF step performed by the ABACUS software and the TRAIN step performed by the DeePKS-kit software, respectively. These two steps iterate over each other until convergence. The neural network can be optimized considering energy E, atomic force $\mathbf{F}$, stress σ and band gap ε_g.

In the TRAIN step, Eq. 137 corresponds to:

$$\min_{\omega} \mathbb{E}_{\text{data}}[L(\omega)],$$
$$L(\omega) = (E_{\text{label}} - E_{\text{DeePKS}}[\{\psi_i\}|\omega])^2. \qquad (139)$$

$L(\omega)$ is the so-called loss function. Loss function $L(\omega)$ can be composed of various energetic terms including the energy E, the atomic force $\mathbf{F}$, the stress tensor σ and the band gap ε_g of the interested system, as shown in Fig. 37.

We take atomic force as an example. Force predicted by DeePKS model can be expressed as:

$$\boldsymbol{F}_{\text{DeePKS}}[\{\psi_i\}|\omega]$$
$$= -\frac{\partial E_{\text{DeePKS}}[\{\psi_i\}|\omega]}{\partial \mathbf{R}}$$
$$= \boldsymbol{F}_{\text{baseline}}[\{\psi_i\}] - \frac{\partial E_{\delta}[\{\psi_i\}|\omega]}{\partial \mathbf{R}}$$
$$= \boldsymbol{F}_{\text{baseline}}[\{\psi_i\}] - \sum_{Inlmm'v} \frac{\partial E_{\delta}}{\partial \mathbf{d}^I_{nlv}} \frac{\partial \mathbf{d}^I_{nlv}}{\partial D^I_{nlmm'}} \frac{\partial D^I_{nlmm'}}{\partial \mathbf{R}}.$$
$$\qquad (140)$$

Note that in the TRAIN procedure, we fix orbitals $\{\psi_i\}$, so that $\frac{\partial \mathbf{d}^I_{nlv}}{\partial \mathbf{X}} = \frac{\partial \mathbf{d}^I_{nlv}}{\partial D^I_{nlmm'}} \frac{\partial D^I_{nlmm'}}{\partial \mathbf{X}}$ is also fixed, which is outputted in the SCF step. The term $\frac{\partial E_{\delta}}{\partial \mathbf{d}^I_{nlv}}$ can be easily calculated in TRAIN step. Once the $\mathbf{F}_{\text{DeePKS}}$ is calculated, the difference between the target force and the current DeePKS force can be optimized.

Similar to the force term, the stress term σ and the band gap term ε_g can be constructed and fed into the loss function. We refer readers to Ref. 216 for a detailed formula.

B. DeePMD-kit

DeePMD[34,276] is a widely-used[42] machine-learning molecular dynamics method based on the neural-network potential.

ABACUS has an interface with the DeePMD-kit package[35,92], allowing its deployment as a molecular dynamics engine in executing DeePMD simulations. Trained on system energy, atomic forces, and lattice stress derived from DFT calculations, this neural network potential enables DeePMD to replicate the potential energy surface with first-principle accuracy. Since the neural network potential is computationally much cheaper than the DFT method, DeePMD can simulate large systems at a long time scale, which is barely accessible for AIMD simulations.

Regarding training, DeePMD requires many atomic configurations with system energies, atomic forces, and optionally virial tensors calculated by the DFT software as the training data. Within ABACUS, these requisite data can be obtained either from the self-consistent calculation (section III B) or from the AIMD simulation (section III D). An atomic simulation data manipulation Python package **dpdata**[277] enables convenient data transfer to the DeePMD training data format.

C. DP-GEN

For more streamlined construction of the Deep Potential PES more efficiently, a recurrent, adaptive learning scheme, DP-GEN (Deep Potential Generator)[271,278], is frequently used to generate the training set for DeePMD and train the Deep Potential model. Starting from training with a small initial dataset, DP-GEN iteratively explores unknown configuration space with the trained models and selectively adds new candidate configurations to the training set. This training collection is periodically enriched, ensuring the continued refinement and improvement of the DeePMD models until a designated precision threshold is attained. Such a process indispensably mandates regular DFT-based first-principles computations on the selected candidate configurations, for which integration with ABACUS has been implanted in the DP-GEN package.

D. DeepH

The deep-learning density functional theory Hamiltonian (DeepH) method is a neural network approach based on equivariant graph neural networks for modeling the DFT Hamiltonian as a function of material structure[279]. Leveraging the sparsity of the Hamiltonian matrix under NAOs and its compatibility with Walter Kohn's "quantum nearsightedness principle"[280], the DeepH method can learn from training data of small structures to infer electronic Hamiltonians of large structures, achieving high prediction accuracy with linear-scaling computational cost. The predicted Hamiltonian may be subsequently utilized for post-processing to evaluate properties including band structures, optical properties, and response properties from density functional perturbation theory, etc[279,281,282].

The interface between ABACUS and DeepH was created in 2022, shortly after the invention of the DeepH approach in 2021. The interface ensures compatibility between ABACUS and various versions of DeepH, including DeepH-pack[279,283],

DeepH-E3[281,284], and DeepH-2[285]. Among these, DeepH-E3 stands out as the most stable open-source implementation to date and has been utilized with ABACUS in several example studies[210,284,286]. The ABACUS-DeepH interface is versatile, supporting spin-orbit coupling and magnetic systems, and facilitates ABACUS's integration with xDeepH– a specialized variant of DeepH for predicting the electronic structures of magnetic materials[287]. To address the modified sparsity patterns in hybrid DFT Hamiltonians, a dedicated toolkit, named DeepH-hybrid, has been developed, which verified DeepH's applicability to hybrid-functional Hamiltonians generated by ABACUS[210,288]. An interface between ABACUS and DeepH-DFPT (a generalization of the DeepH approach for deep-learning density functional perturbation theory) is currently under development to accelerate calculations of electron-phonon coupling[282]. In addition, a recently developed "Hamiltonian Projection and Reconstruction to atomic Orbitals" (H-PRO) method can transform the DFT Hamiltonian of plane-wave basis into localized basis, making the DeepH compatible with the plane-wave mode of ABACUS[289]. Very recently, a universal materials model (UMM) of DeepH, named DeepH-UMM, has been developed, demonstrating exceptional transferability across a wide range of material structures composed of various elements[290]. Given ABACUS's versatility, further development of DeepH-UMM in conjunction with ABACUS holds significant promise for advancing materials discovery.

The current ABACUS-DeepH interface is available on GitHub[283]. For data preparation, the keyword `out_mat_hs2=1` is mandatory in the ABACUS input file, enabling the formatted output of the Hamiltonian and overlap matrix in a sparse matrix (CSR) form. For inference with trained DeepH models, ABACUS's `get_S` function provides an efficient method for generating the overlap matrix, from which the Hamiltonian can be predicted by DeepH. It is important to note the overlap and Hamiltonian matrices are assumed to shared the same sparsity pattern in DeepH. To ensure clarity, fixing such sparsity pattern with tools provided in DeepH-hybrid is recommended[288]. Tutorials for the interface are available online, and four demo datasets with hybrid DFT Hamiltonians computed with ABACUS are publicly available on Zenodo[283,288].

E. DeePTB

DeePTB is an innovative open-source package that leverages deep learning to accelerate ab initio electronic simulations[291,292]. Its integration with ABACUS creates a powerful synergy, combining first-principles calculations with advanced machine learning techniques for efficient large-scale electronic structure predictions. Notably, it has demonstrated the capability to simulate systems containing up to millions of atoms[291], a scale previously unattainable with traditional methods.

Fig. 38 illustrates the ABACUS-DeePTB workflow. ABACUS performs DFT calculations on training structural data obtained from crystal databases or molecular dynamics sim-
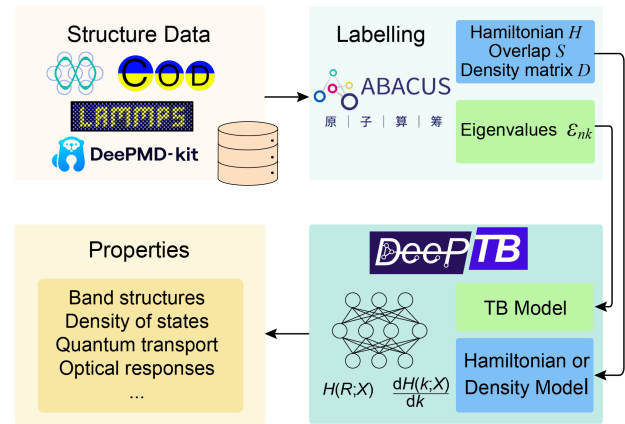

FIG. 38: Workflow-chart of ABACUS-DeePTB integration for deep learning-based TB and quantum operators (Hamiltonian, overlap, and density matrices) predictions.

ulations, generating essential quantum mechanical data as labels including energy eigenvalues, NAOs basis Hamiltonian, overlap, and density matrices. DeePTB utilizes this ABACUS-generated data to train two key models: the DeePTB-SK[291] and DeePTB-E3[292] models. The DeePTB-SK model uses energy eigenvalues to develop an improved Slater-Koster TB models for efficient electronic structure prediction, while the DeePTB-E3 model, based on the SLEM (Strictly Localized Equivariant Message-passing) approach, predicts quantum operators including the Hamiltonian, overlap, and density matrices.

This integrated approach significantly enhances the efficiency and scalability of electronic structure simulations, enabling the study of complex and large-scale material systems previously limited by computational constraints. For instance, recent work combining DeePTB with non-equilibrium Green's function (NEGF) methods has demonstrated unprecedented efficiency in quantum transport simulations of large-scale nanodevices[293]. The ABACUS-DeePTB collaboration demonstrates the potential of combining traditional DFT methods with cutting-edge machine learning in computational materials science, opening new avenues for high-throughput materials discovery and design.

F. PyATB

PYATB (Python ab initio tight-binding simulation package) is a Python package based on ab initio tight-binding Hamiltonian, designed as a tool for calculating and analyzing the electronic band structures of materials[294]. It can be viewed as a post-processing program for the ABACUS. When ABACUS completes the self-consistent electronic calculations and generates the tight-binding Hamiltonian, PYATB utilizes this Hamiltonian to perform electronic property calculations. This eliminates the need for the cumbersome construction of ML-WFs while strictly preserving the Hamiltonian's symmetry, making it particularly well-suited for high-throughput work-

flows in electronic structure calculations of various materials. Currently, PYATB mainly offers three functional modules: Bands, Geometric, and Optical. This allows ABACUS, in combination with PYATB, to compute basic band structures, fat bands, and projected density of states (PDOS). Additionally, it can analyze the Berry curvature and Chern number of topological materials[295,296], as well as compute first- and second-order optical responses such as optical conductivity, shift current, second harmonic generation[297–299] and Berry curvature dipole[300,301].

ABACUS standard self-consistent calculations can generate the Hamiltonian matrix $\mathbf{H}(\mathbf{k})$, the overlap matrix $\mathbf{S}(\mathbf{k})$, and the dipole matrix

$$\mathbf{A}_{\mu\nu}^{\mathbf{R}}(\mathbf{k}) = \sum_{\mathbf{R}} e^{i\mathbf{k}\cdot\mathbf{R}} \langle \phi_{\mu 0} | \mathbf{r} | \phi_{\nu\mathbf{R}} \rangle. \tag{141}$$

Using these input parameters, PYATB can solve the following generalized eigenvalue problem:

$$\mathbf{H}(\mathbf{k})\mathbf{C}_n(\mathbf{k}) = E_{n\mathbf{k}}\mathbf{S}(k)\mathbf{C}(\mathbf{k}), \tag{142}$$

where $\mathbf{C}_n(\mathbf{k})$ is the eigenvector of the n-th band, then obtain the band structure and Bloch wavefunctions information. Subsequently, based on the wavefunctions, the Berry curvature[295,302] can be calculated as:

$$\Omega_n(\mathbf{k}) = \nabla_{\mathbf{k}} \times i\langle u_{n\mathbf{k}} | \nabla_{\mathbf{k}} | u_{n\mathbf{k}} \rangle. \tag{143}$$

This allows for the calculation of various topological and optical properties of materials. One can refer to Ref. 294 for the implementation details.

G. Hefei-NAMD

Hefei Non-Adiabatic Molecular Dynamics (Hefei-NAMD) is an ab initio simulation suite for studying excited carrier dynamics in condensed matter systems. It combines real-time time-dependent density functional theory (TDDFT) with the fewest-switches surface hopping scheme and classical-path approximation. Hefei-NAMD has been used to investigate processes such as charge transfer, electron–hole recombination, spin dynamics and exciton dynamics[303–306]. It allows the study of excited carrier dynamics in energy, real, and momentum spaces, while also exploring interactions with phonons, defects, and molecular adsorptions, providing valuable insights into ultrafast dynamics at the atomic scale. Hefei-NAMD works by interfacing with other ab initio codes, e.g. VASP, ABACUS etc. Figure 39 shows the flowchart of the simulation using Hefei-NAMD interfaced with ABACUS. Detail documentations can be found on the ABACUS webcite[307].

H. PEXSI

PEXSI (Pole EXpansion and Selected Inversion)[308,309] provides an alternative method for solving the KS equation without using diagonalization methods. Given the generalized eigenvalue problem $H\Phi = \varepsilon S\Phi$ transferred from KS equation,
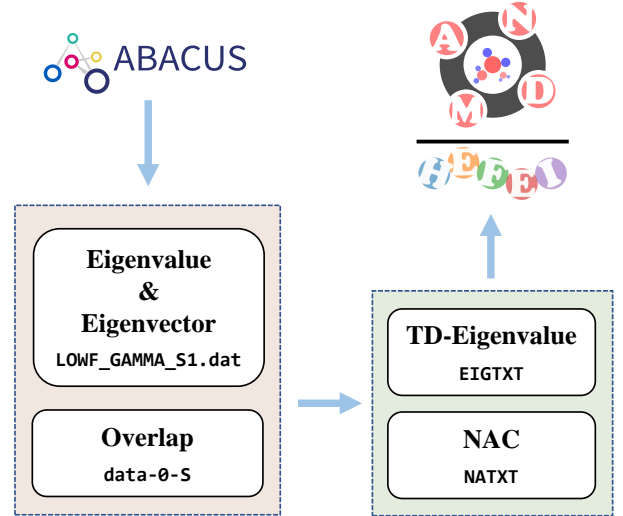

FIG. 39: Workflow-chart of Hefei-NAMD interfaced with ABACUS.

PEXSI directly calculates the real-space density matrix from H and S matrix.

We denote the collection of all atomic orbitals in the real space $\Phi(\mathbf{r})$ as $[\phi_1(\mathbf{r}), \cdots, \phi_M(\mathbf{r})]$, and the single particle real-space density matrix $\hat{\gamma}(\mathbf{r}, \mathbf{r}')$ can be formally expressed as

$$\hat{\gamma}(\mathbf{r}, \mathbf{r}') = \Phi(\mathbf{r}) f(H - \mu S)\Phi^*(\mathbf{r}'), \tag{144}$$

where f is the Fermi-Dirac distribution function and μ is the chemical potential. From the density matrix, we can get charge density in the following form:

$$\rho(\mathbf{r}) = \hat{\gamma}(\mathbf{r}, \mathbf{r}). \tag{145}$$

PEXSI expands the matrix Fermi-Dirac function using a P-term pole expansion:

$$f(H - \mu S) \approx \mathrm{Im} \sum_{l=1}^{P} \omega_l^{\rho} [H - (z_l + \mu)S]^{-1}, \tag{146}$$

where coefficients z_l and ω_l are chosen carefully and can be computed in advance. PEXSI uses selected inversion to calculate these inverse matrices effectively.

The computational cost of standard diagonalization methods scales as $\mathcal{O}(N^3)$, while PEXSI scales at most as $\mathcal{O}(N^2)$, where N is the dimension of the matrix. The PEXSI method has a two-level parallelism structure (pole expansion parallelism and selected inversion parallelism) and is designed to be of high scalability. The sequential version of PEXSI has been tested before with ABACUS[309]. Now, ABACUS has implemented an interface to the parallel version of PEXSI for solving the KS equation on NAO basis.

I. Others

The Atomic Simulation Environment (ASE) comprises a comprehensive suite of tools and Python modules designed for
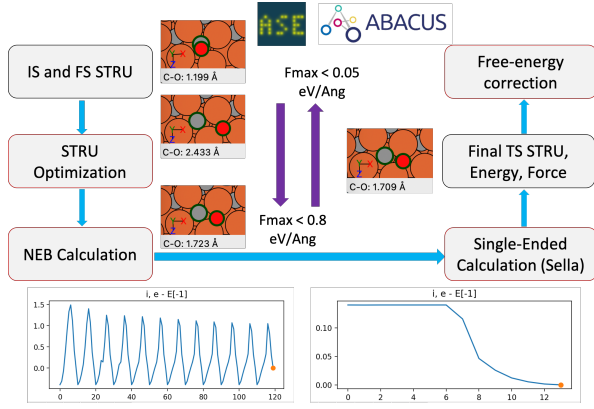
FIG. 40: Workflow-chart of NEB + Sella method for locating TS based on ASE and ABACUS, red block denotes the usage of ABACUS as calculator

setting up, manipulating, executing, visualizing, and analyzing atomic simulations[310]. In our framework, we have developed an ABACUS calculator[311] that interfaces with the latest version of ASE (3.23.0b1) and that enables seamless integration of ASE's robust functionalities for both pre-processing and post-processing tasks.

Regarding pre-processing capabilities, the interface facilitates tasks such as converting structural files a in various formats, generating uniform k-point grids tailored to specific simulation needs, and establishing high-symmetry paths essential for accurate calculations of electronic band structures and other properties. For post-processing, the integration with ASE empowers ABACUS users with advanced tools for visualizing and analyzing simulation results. This includes visualizing the structure and energy plot of the optimization process, plotting electronic band structures, and performing MD trajectory analyses.

Moreover, the collaboration between ABACUS and ASE extends beyond basic simulations to encompass complex computational tasks. The self-consistent calculations of ABACUS are combined with ASE's built-in optimization algorithms, facilitating structural relaxation procedures, conducting MD simulations under varying conditions, performing precise phonon calculations based on the finite displacement method, carrying-out global optimization by genetic algorithm (GA), locating transition states (TS) of reactions by saddle point refinement, and more.

For TS search, as an example, two most widely used methods, the nudged elastic band (NEB)[312–314] method and the Dimer[315–318] method, which represent double-ended TS searching methods and single-end TS methods respectively, are implemented in ASE. Besides, some other enhanced NEB methods are coded in the ASE package, such as dynamic NEB[319] and AutoNEB[320]. Furthermore, there are many other saddle point refinement algorithms implemented in ASE, and some of them show better performance, like Sella[321–323]. With the above-mentioned methods available in ASE, ABACUS can be used for searching for transition states.

Apart from directly using TS search tools in ASE, the co-operation of different TS search methods can be done due to ASE's coding flexibility, which leads to better TS locating functionality. One way is to first generate a rough TS by NEB, then utilize a single-ended method like Dimer or Sella to optimize the TS in the target threshold, which incorporates the advantage of both methods. As is shown in Fig. 40, ATST-Tools scripts suite[324] is prepared for handy usage of ABACUS and ASE in TS locating jobs.

Phonopy[274,275] is a versatile open-source software package designed for calculating phonon and related lattice dynamics properties from first-principles calculations. With the addition of the ABACUS interface in Phonopy version 2.19.1, users can now leverage the computational capabilities of ABACUS to compute the electronic structure and force constants that Phonopy requires for its phonon calculations.

The phonon dispersion relation describes the relationship between the energy of phonons (lattice vibrations) and their wave vector ($\mathbf{q}$) within a crystal. Under the harmonic approximation, the energy of a phonon mode at a given point, $\mathbf{q}$, and the polarization index ν can be calculated as follows:

$$\hbar\omega_{\mathbf{q}\nu} = \sqrt{\frac{\hbar^2}{2\mu}\sum_{i,j}M_iM_j|\mathbf{e}^*_{\mathbf{q}\nu,i}\cdot D_{ij}(\mathbf{q})\cdot\mathbf{e}_{\mathbf{q}\nu,j}|^2}, \qquad (147)$$

where $\omega_{\mathbf{q}\nu}$ is the angular frequency of the phonon mode; $D_{ij}(\mathbf{q})$ is the dynamical matrix element between atoms i and j at the $\mathbf{q}$-point; $\mathbf{e}_{\mathbf{q}\nu,i}$ is the eigenvector associated with atom i for the νth phonon mode at $\mathbf{q}$; M_i and M_j are the masses of atoms i and j; μ is the reduced mass, typically $M_iM_j/(M_i+M_j)$.

$D_{ij}(\mathbf{q})$ is derived from the force constants, which relate the forces on each atom to the displacements of other atoms in the crystal. ABACUS can provide the force constants through finite displacement methods, where small displacements are applied to atoms in the crystal. Recent research efforts[269,325] highlighted the success on the synergy between ABACUS and Phonopy to explore novel materials and optimize existing ones utilizing accurate phonon spectra.

TB2J[326] is an open-source Python package for automatic computation of magnetic interactions between atoms of magnetic crystals from density functional Hamiltonians based on Wannier functions or linear combinations of atomic orbitals. The program is based on Green's function method with the local rigid spin rotation treated as a perturbation[327]. The ABACUS interface has been added since TB2J version 0.8.0. With the Hamiltonian matrix $\mathbf{H}(\mathbf{k})$ and the overlap matrix $\mathbf{S}(\mathbf{k})$ obtained by an LCAO calculation, TB2J is able to compute the parameters of the Heisenberg Hamiltonian

$$H_{\mathrm{H}} = -\sum_{i\neq j}J^{iso}_{ij}\overrightarrow{S}_i\cdot\overrightarrow{S}_j - \sum_{i\neq j}\overrightarrow{S}_i\cdot\mathbf{J}^{ani}_{ij}\cdot\overrightarrow{S}_j - \sum_{i\neq j}\overrightarrow{D}_{ij}\cdot(\overrightarrow{S}_i\times\overrightarrow{S}_j),$$

$$(148)$$

where J^{iso}_{ij} represents the isotropic exchange, $\mathbf{J}^{ani}_{ij}$ represents the symmetric anisotropic exchange which is a 3×3 tensor, $\overrightarrow{D}_{ij}$ represents the Dzyaloshinskii-Moriya interaction (DMI). In addition, one can add the single-ion anisotropy (SIA) into the above Hamiltonian. In 2024, Zhang et al.[328] calculate

the J_{ij}^{iso}, $\mathbf{J}_{ij}^{ani}$ and $\overrightarrow{D}_{ij}$ for GeFe$_3$N by using ABACUS$-$TB2J, which help them study the short-range order and strong interplay between local and itinerant magnetism in GeFe$_3$N.

Wannier90[329] is a software package designed for calculating maximally-localized Wannier functions (MLWFs)[330], which facilitates cost-effective band structure calculations. MLWFs are often used to construct model Hamiltonians. The post-processing capabilities of Wannier90 enable the calculation of various properties, such as Berry curvature, Berry curvature dipole, and shift current[329]. Additionally, MLWFs generated by Wannier90 can be analyzed for material surface states and topological properties using the Wannier Tools[331].

According to the standard scheme for generating maximally localized Wannier functions in Wannier90, ABACUS has implemented an interface compatible with the Wannier90 software. This interface allows ABACUS to generate the necessary files for Wannier90, including overlap files (`*.mmn`) between the periodic parts of Bloch functions at neighboring **k**-points, projection files (`*.amn`) of Bloch functions onto trial localized orbitals, eigenvalue files (`*.eig`) of the energy bands, and real-space distribution files (`UNK.*`) of the periodic parts of Bloch functions.

In the numerical atomic orbitals basis calculation, the `*.mmn` files are calculated using radial Gauss–Legendre and angular Lebedev-Laikov quadrature grids[332]. The overlap matrix elements are computed as follows:

$$
\begin{aligned}
&\langle u_{n\mathbf{k}}|u_{m,\mathbf{k}+\mathbf{b}}\rangle \\
&= \sum_{\mu\nu} C_{n\mu}(\mathbf{k})^* C_{m\nu}(\mathbf{k}+\mathbf{b}) \sum_{\mathbf{R}} e^{i(\mathbf{k}+\mathbf{b})\cdot\mathbf{R}} \langle \phi_{\mu 0}|e^{-i\mathbf{b}\cdot\mathbf{r}}|\phi_{\nu\mathbf{R}}\rangle,
\end{aligned}
$$
(149)

where $u_{n\mathbf{k}}$ is the periodic part of the Bloch wave function $\psi_{n\mathbf{k}}$, **k** and $\mathbf{k}+\mathbf{b}$ are two neighboring points, and $C_{n\mu}$ represents the expansion coefficients of $\psi_{n\mathbf{k}}$ in terms of atomic orbitals ϕ_μ. This method ensures precise calculation of the overlap matrix elements, which are essential for constructing accurate MLWFs.

VIII. SUMMARY

In this comprehensive review, we have detailed the advancements and capabilities of the ABACUS software, a powerful open-source platform for first-principles electronic structure calculations and molecular dynamics simulations. ABACUS stands out for its versatility, supporting both plane-wave and numerical atomic orbital basis sets, and its compatibility with a range of electronic structure methods.

The methods based on the plane-wave basis in ABACUS have been continuously developed. Stochastic DFT has been implemented, offering an alternative approach to handle large systems with improved computational efficiency. Orbital-Free DFT has also been included, with different kinetic energy density functionals and optimization methods available. For calculations using the numerical atomic orbital basis, ABACUS provides efficient implementations. The methods such as hybrid functionals, DFT+U, and Real-Time TDDFT have been extended to this basis set. The integration of machine learn-

ing techniques in the form of the DeePKS method has shown great potential in achieving high accuracy at a reduced computational cost. These methods have been benchmarked and applied to various systems, demonstrating their accuracy and effectiveness.

ABACUS has actively participated in the OpenLAM project, generating high-precision first-principles data for different scenarios, including semiconductors, alloys, ferroelectric, and superhydrides. The APNS project has been initiated to ensure the reliability and accuracy of ABACUS. Systematic tests for pseudopotentials and numerical atomic orbitals have been conducted, providing a solid foundation for the software's performance. The software's ability to interface with other packages, such as DeePKS-kit, DeePMD, DP-GEN, DeepH, DeePTB, PyATB, Hefei-NAMD, ASE, Phonopy, TB2J, and Wannier90, further expands its functionality and applicability in multi-scale simulations and analysis.

In conclusion, ABACUS has established itself as a robust and flexible platform for electronic structure calculations, poised to meet the challenges of materials science, chemistry, and physics in the AI era. Its ongoing development and integration with AI technologies promise to further enhance its capabilities, making it an indispensable tool for researchers and scientists in the field.

DATA AVAILABILITY STATEMENT

The data that support the findings of this study are available from the corresponding author upon reasonable request.

REFERENCES

[1] P. Hohenberg and W. Kohn, "Inhomogeneous electron gas," Phys. Rev. **136**, B864 (1964).

[2] W. Kohn and L. J. Sham, "Self-consistent equations including exchange and correlation effects," Phys. Rev. **140**, A1133 (1965).

[3] P. Blaha, K. Schwarz, F. Tran, R. Laskowski, G. K. Madsen, and L. D. Marks, "WIEN2k: An APW+ lo program for calculating the properties of solids," J. Chem. Phys. **152** (2020).

[4] Y. Zhang, B. Suo, Z. Wang, N. Zhang, Z. Li, Y. Lei, W. Zou, J. Gao, D. Peng, Z. Pu, *et al.*, "BDF: A relativistic electronic structure program package," J. Chem. Phys. **152** (2020).

[5] A. H. Romero, D. C. Allan, B. Amadon, G. Antonius, T. Applencourt, L. Baguet, J. Bieder, F. Bottin, J. Bouchet, E. Bousquet, *et al.*, "ABINIT: Overview and focus on selected capabilities," J. Chem. Phys. **152** (2020).

[6] A. Nakata, J. S. Baker, S. Y. Mujahed, J. T. Poulton, S. Arapan, J. Lin, Z. Raza, S. Yadav, L. Truflandier, T. Miyazaki, *et al.*, "Large scale and linear scaling dft with the CONQUEST code," J. Chem. Phys. **152** (2020).

[7] T. D. Kühne, M. Iannuzzi, M. Del Ben, V. V. Rybkin, P. Seewald, F. Stein, T. Laino, R. Z. Khaliullin, O. Schütt, F. Schiffmann, *et al.*, "CP2K: An electronic structure and molecular dynamics software package-quickstep: Efficient and accurate electronic structure calculations," J. Chem. Phys. **152** (2020).

[8] N. Tancogne-Dejean, M. J. Oliveira, X. Andrade, H. Appel, C. H. Borca, G. Le Breton, F. Buchholz, A. Castro, S. Corni, A. A. Correa, *et al.*, "Octopus, a computational framework for exploring light-driven phenomena and quantum dynamics in extended and finite systems," J. Chem. Phys. **152** (2020).

[9] J. C. Prentice, J. Aarons, J. C. Womack, A. E. Allen, L. Andrinopoulos, L. Anton, R. A. Bell, A. Bhandari, G. A. Bramley, R. J. Charlton, *et al.*, "The ONETEP linear-scaling density functional theory program," J. Chem. Phys. **152** (2020).

[10] Q. Sun, X. Zhang, S. Banerjee, P. Bao, M. Barbry, N. S. Blunt, N. A. Bogdanov, G. H. Booth, J. Chen, Z.-H. Cui, *et al.*, "Recent developments in the PySCF program package," J. Chem. Phys. **153** (2020).

[11] P. Giannozzi, O. Baseggio, P. Bonfà, D. Brunato, R. Car, I. Carnimeo, C. Cavazzoni, S. De Gironcoli, P. Delugas, F. Ferrari Ruffino, *et al.*, "Quantum ESPRESSO toward the exascale," J. Chem. Phys. **152** (2020).

[12] A. García, N. Papior, A. Akhtar, E. Artacho, V. Blum, E. Bosoni, P. Brandimarte, M. Brandbyge, J. I. Cerdá, F. Corsetti, *et al.*, "Siesta: Recent developments and applications," J. Chem. Phys. **152** (2020).

[13] G. Kresse and D. Joubert, "From ultrasoft pseudopotentials to the projector augmented-wave method," Phys. Rev. B **59**, 1758 (1999).

[14] M. J. Frisch, G. W. Trucks, H. B. Schlegel, G. E. Scuseria, M. A. Robb, J. R. Cheeseman, G. Scalmani, V. Barone, G. A. Petersson, H. Nakatsuji, X. Li, M. Caricato, A. V. Marenich, J. Bloino, B. G. Janesko, R. Gomperts, B. Mennucci, H. P. Hratchian, J. V. Ortiz, A. F. Izmaylov, J. L. Sonnenberg, D. Williams-Young, F. Ding, F. Lipparini, F. Egidi, J. Goings, B. Peng, A. Petrone, T. Henderson, D. Ranasinghe, V. G. Zakrzewski, J. Gao, N. Rega, G. Zheng, W. Liang, M. Hada, M. Ehara, K. Toyota, R. Fukuda, J. Hasegawa, M. Ishida, T. Nakajima, Y. Honda, O. Kitao, H. Nakai, T. Vreven, K. Throssell, J. A. Montgomery, Jr., J. E. Peralta, F. Ogliaro, M. J. Bearpark, J. J. Heyd, E. N. Brothers, K. N. Kudin, V. N. Staroverov, T. A. Keith, R. Kobayashi, J. Normand, K. Raghavachari, A. P. Rendell, J. C. Burant, S. S. Iyengar, J. Tomasi, M. Cossi, J. M. Millam, M. Klene, C. Adamo, R. Cammi, J. W. Ochterski, R. L. Martin, K. Morokuma, O. Farkas, J. B. Foresman, and D. J. Fox, "Gaussian~16 Revision C.01," (2016), gaussian Inc. Wallingford CT.

[15] F. Gygi, E. W. Draeger, M. Schulz, B. R. De Supinski, J. A. Gunnels, V. Austel, J. C. Sexton, F. Franchetti, S. Kral, C. W. Ueberhuber, *et al.*, "Large-scale electronic structure calculations of high-z metals on the blue-gene/l platform," in *Proceedings of the 2006 ACM/IEEE conference on Supercomputing* (2006) pp. 45–es.

[16] O. Watanabe, A. Musa, H. Hokari, S. Singh, R. Mathur, and H. Kobayashi, "Performance evaluation of quantum espresso on nec sx-ace," in *2017 IEEE International Conference on Cluster Computing (CLUSTER)* (IEEE, 2017) pp. 701–708.

[17] P. Lucignano, D. Alfè, V. Cataudella, D. Ninno, and G. Cantele, "Crucial role of atomic corrugation on the flat bands and energy gaps of twisted bilayer graphene at the magic angle $\theta \sim 1.08°$," Phys. Rev. B **99**, 195419 (2019).

[18] X. Gonze, B. Amadon, G. Antonius, F. Arnardi, L. Baguet, J.-M. Beuken, J. Bieder, F. Bottin, J. Bouchet, E. Bousquet, *et al.*, "The ABINIT project: Impact, environment and recent developments," Comput. Phys. Commun. **248**, 107042 (2020).

[19] J. Feng, L. Wan, J. Li, S. Jiao, X. Cui, W. Hu, and J. Yang, "Massively parallel implementation of iterative eigensolvers in large-scale plane-wave density functional theory," Comput. Phys. Commun. **299**, 109135 (2024).

[20] M. Chen, G.-C. Guo, and L. He, "Systematically improvable optimized atomic basis sets for ab initio calculations," J. Phys. Condens. Matter **22**, 445501 (2010).

[21] M. Chen, G.-C. Guo, and L. He, "Electronic structure interpolation via atomic orbitals," J. Phys. Condens. Matter **23**, 325501 (2011).

[22] P. Li, X. Liu, M. Chen, P. Lin, X. Ren, L. Lin, C. Yang, and L. He, "Large-scale ab initio simulations based on systematically improvable atomic basis," Comput. Mater. Sci. **112**, 503–517 (2016).

[23] P. Lin, X. Ren, and L. He, "Accuracy of Localized Resolution of the Identity in Periodic Hybrid Functional Calculations with Numerical Atomic Orbitals," J. Phys. Chem. Lett. **11**, 3082–3088 (2020).

[24] D. Zheng, X. Ren, and L. He, "Accurate stress calculations based on numerical atomic orbital bases: Implementation and benchmarks," Comput. Phys. Commun. **267**, 108043 (2021).

[25] P. Lin, X. Ren, and L. He, "Efficient Hybrid Density Functional Calculations for Large Periodic Systems Using Numerical Atomic Orbitals," J. Chem. Theory Comput. **17**, 222–239 (2021).

[26] P. Lin, X. Ren, and L. He, "Strategy for constructing compact numerical atomic orbital basis sets by incorporating the gradients of reference wavefunctions," Phys. Rev. B **103**, 235131 (2021).

[27] X. Qu, P. Xu, H. Jiang, L. He, and X. Ren, "DFT+ U within the framework of linear combination of numerical atomic orbitals," J. Chem. Phys. **156** (2022).

[28] X. Qu, P. Xu, R. Li, G. Li, L. He, and X. Ren, "Density functional theory plus dynamical mean field theory within the framework of linear combination of numerical atomic orbitals: Formulation and benchmarks," J. Chem. Theory Comput. **18**, 5589–5606 (2022).

[29] Q. Liu and M. Chen, "Plane-wave-based stochastic-deterministic density functional theory for extended systems," Phys. Rev. B **106**, 125132 (2022).

[30] Z. Dai, G. Jin, and L. He, "First-principles calculations of the surface states of doped and alloyed topological materials via band unfolding method," Comput. Mater. Sci. **213**, 111656 (2022).

[31] R. Liu, D. Zheng, X. Liang, X. Ren, M. Chen, and W. Li, "Implementation of the meta-gga exchange-correlation functional in numerical atomic orbital basis: With systematic testing on SCAN, rSCAN, and r2SCAN functionals," J. Chem. Phys. **159** (2023).

[32] P. Lin, X. Ren, X. Liu, and L. He, "Ab initio electronic structure calculations based on numerical atomic orbitals: Basic fomalisms and recent progresses," Wiley Interdiscip. Rev. Comput. Mol. Sci. **14**, e1687 (2024).

[33] https://github.com/deepmodeling/abacus-develop (2024).

[34] L. Zhang, J. Han, H. Wang, R. Car, and W. E, "Deep Potential Molecular Dynamics: A Scalable Model with the Accuracy of Quantum Mechanics," Phys. Rev. Lett. **120**, 143001 (2018).

[35] H. Wang, L. Zhang, J. Han, and W. E, "Deepmd-kit: A deep learning package for many-body potential energy representation and molecular dynamics," Comput. Phys. Comm. **228**, 178–184 (2018).

[36] Y. Chen, L. Zhang, H. Wang, and W. E, "DeePKS: A Comprehensive Data-Driven Approach toward Chemically Accurate Density Functional Theory," J. Chem. Theory Comput. **17**, 170–181 (2021).

[37] Y. Chen, L. Zhang, H. Wang, and W. E, "DeePKS-kit: A package for developing machine learning-based chemically accurate energy and density functional models," Comput. Phys. Commun. **282**, 108520 (2022).

[38] J. Kirkpatrick, B. McMorrow, D. H. Turban, A. L. Gaunt, J. S. Spencer, A. G. Matthews, A. Obika, L. Thiry, M. Fortunato, D. Pfau, *et al.*, "Pushing the frontiers of density functionals by solving the fractional electron problem," Science **374**, 1385–1389 (2021).

[39] W. Jia, H. Wang, M. Chen, D. Lu, L. Lin, R. Car, E. Weinan, and L. Zhang, "Pushing the limit of molecular dynamics with ab initio accuracy to 100 million atoms with machine learning," in *SC20: International conference for high performance computing, networking, storage and analysis* (IEEE, 2020) pp. 1–14.

[40] J. Han, L. Zhang, and E. Weinan, "Solving many-electron schrödinger equation using deep neural networks," J. Comput. Phys. **399**, 108929 (2019).

[41] Y. Chen, L. Zhang, H. Wang, and W. E, "Ground state energy functional with Hartree–Fock efficiency and chemical accuracy," J. Phys. Chem. A **124**, 7155–7165 (2020).

[42] T. Wen, L. Zhang, H. Wang, W. E, and D. J. Srolovitz, "Deep potentials for materials science," Mater. Futures **1**, 022601 (2022).

[43] A. Paszke, S. Gross, F. Massa, A. Lerer, J. Bradbury, G. Chanan, T. Killeen, Z. Lin, N. Gimelshein, L. Antiga, *et al.*, "Pytorch: An imperative style, high-performance deep learning library," Adv. Neural Inf. Process. Syst. **32** (2019).

[44] M. Abadi, P. Barham, J. Chen, Z. Chen, A. Davis, J. Dean, M. Devin, S. Ghemawat, G. Irving, M. Isard, *et al.*, "TensorFlow: a system for large-scale machine learning," in *12th USENIX symposium on operating systems design and implementation (OSDI 16)* (2016) pp. 265–283.

[45] W. Li, Q. Ou, Y. Chen, Y. Cao, R. Liu, C. Zhang, D. Zheng, C. Cai, X. Wu, H. Wang, M. Chen, and L. Zhang, "DeePKS+ABACUS as a Bridge between Expensive Quantum Mechanical Models and Machine Learning Potentials," J. Phys. Chem. A **126**, 9154–9164 (2022).

[46] https://www.aissquare.com/openlam (2024).

[47] R. M. Martin, *Electronic structure: basic theory and practical methods* (Cambridge university press, 2020).

[48] H. J. Monkhorst and J. D. Pack, "Special points for brillouin-zone integrations," Phys. Rev. B **13**, 5188–5192 (1976).

[49] https://abacus.ustc.edu.cn/main.htm (2024).

[50] S. Boker, M. Neale, H. Maes, M. Wilde, M. Spiegel, T. Brick, J. Spies, R. Estabrook, S. Kenny, T. Bates, *et al.*, "OpenMx: an open source extended structural equation modeling framework," Psychometrika **76**, 306–317 (2011).

[51] V. Blum, R. Gehrke, F. Hanke, P. Havu, V. Havu, X. Ren, K. Reuter, and M. Scheffler, "Ab initio molecular simulations with numeric atom-centered orbitals," Comput. Phys. Commun. **180**, 2175–2196 (2009).

[52] J. R. Chelikowsky, N. Troullier, and Y. Saad, "Finite-difference-pseudopotential method: Electronic structure calculations without a basis," Phys. Rev. Lett. **72**, 1240–1243 (1994).

[53] L. E. Ratcliff, W. Dawson, G. Fisicaro, D. Caliste, S. Mohr, A. Degomme, B. Videau, V. Cristiglio, M. Stella, M. D'Alessandro, *et al.*, "Flexibilities of wavelets as a computational basis set for large-scale electronic structure calculations," J. Chem. Phys. **152** (2020).

[54] L. Kleinman, "Relativistic norm-conserving pseudopotential," Phys. Rev. B **21**, 2630 (1980).

[55] G. B. Bachelet and M. Schlüter, "Relativistic norm-conserving pseudopotentials," Phys. Rev. B **25**, 2103 (1982).

[56] L. Kleinman and D. Bylander, "Efficacious form for model pseudopotentials," Phys. Rev. Lett. **48**, 1425 (1982).

[57] G. Kresse and J. Hafner, "Norm-conserving and ultrasoft pseudopotentials for first-row and transition elements," J. Phys. Condens. Matter **6**, 8245 (1994).

[58] J. P. Perdew, K. Burke, and M. Ernzerhof, "Generalized gradient approximation made simple," Phys. Rev. Lett. **77**, 3865 (1996).

[59] J. Sun, A. Ruzsinszky, and J. P. Perdew, "Strongly constrained and appropriately normed semilocal density functional," Phys. Rev. Lett. **115**, 036402 (2015).

[60] J. Heyd, G. E. Scuseria, and M. Ernzerhof, "Hybrid functionals based on a screened Coulomb potential," J. Chem. Phys. **118**, 8207–8215 (2003).

[61] https://libxc.gitlab.io/ (2024).

[62] A. P. Bartók and J. R. Yates, "Regularized SCAN functional," J. Chem. Phys. **150** (2019).

[63] J. W. Furness, A. D. Kaplan, J. Ning, J. P. Perdew, and J. Sun, "Accurate and numerically efficient r2SCAN meta-generalized gradient approxima-

tion," J. Phys. Chem. Lett. **11**, 8208–8215 (2020).

[64] B. Miehlich, A. Savin, H. Stoll, and H. Preuss, "Results obtained with the correlation energy density functionals of Becke and Lee, Yang and Parr," Chem. Phys. Lett. **157**, 200–206 (1989).

[65] L. Hemstreet, C. Fong, and J. Nelson, "First-principles calculations of spin-orbit splittings in solids using nonlocal separable pseudopotentials," Phys. Rev. B **47**, 4238 (1993).

[66] G. Theurich and N. A. Hill, "Self-consistent treatment of spin-orbit coupling in solids using relativistic fully separable ab initio pseudopotentials," Phys. Rev. B **64**, 073106 (2001).

[67] P. Pulay, "Convergence acceleration of iterative sequences. the case of scf iteration," Chem. Phys. Lett. **73**, 393–398 (1980).

[68] P. Pulay, "Improved scf convergence acceleration," J. Comput. Chem. **3**, 556–560 (1982).

[69] D. D. Johnson, "Modified broyden's method for accelerating convergence in self-consistent calculations," Phys. Rev. B **38**, 12807–12813 (1988).

[70] G. Kresse and J. Furthmüller, "Efficient iterative schemes for ab initio total-energy calculations using a plane-wave basis set," Phys. Rev. B **54**, 11169–11186 (1996).

[71] https://github.com/deepmodeling/abacus-develop/pull/3133 (2024).

[72] Y. Zhou, H. Wang, Y. Liu, X. Gao, and H. Song, "Applicability of kerker preconditioning scheme to the self-consistent density functional theory calculations of inhomogeneous systems," Phys. Rev. E **97**, 033305 (2018).

[73] M. Heide and T. Ono, "Convergence of the broyden density mixing method in noncollinear magnetic systems," J. Phys. Soc. Jpn. **82**, 114706 (2013).

[74] M. Cococcioni and S. De Gironcoli, "Linear response approach to the calculation of the effective interaction parameters in the LDA+U method," Phys. Rev. B **71**, 035105 (2005).

[75] V. I. Anisimov, I. Solovyev, M. Korotin, M. Czyżyk, and G. Sawatzky, "Density-functional theory and NiO photoemission spectra," Phys. Rev. B **48**, 16929 (1993).

[76] V. I. Anisimov, F. Aryasetiawan, and A. Lichtenstein, "First-principles calculations of the electronic structure and spectra of strongly correlated systems: the LDA+U method," J. Phys. Condens. Matter **9**, 767 (1997).

[77] S. L. Dudarev, G. A. Botton, S. Y. Savrasov, C. Humphreys, and A. P. Sutton, "Electron-energy-loss spectra and the structural stability of nickel oxide: An LSDA+ U study," Phys. Rev. B **57**, 1505 (1998).

[78] H. Jiang, R. I. Gomez-Abal, P. Rinke, and M. Scheffler, "First-principles modeling of localized d states with the GW@LDA+U approach," Phys. Rev. B **82**, 045108 (2010).

[79] B. Meredig, A. Thompson, H. A. Hansen, C. Wolverton, and A. van de Walle, "Method for locating low-energy solutions within DFT+U," Phys. Rev. B **82**, 195128 (2010).

[80] B. Dorado, M. Freyss, B. Amadon, M. Bertolus, G. Jomard, and P. Garcia, "Advances in first-principles modelling of point defects in UO₂: f electron correlations and the issue of local energy minima," J. Phys. Condens. Matter **25**, 333201 (2013).

[81] M. A. Halcrow, "Jahn-teller distortions in transition metal compounds, and their importance in functional molecular and inorganic materials," Chem. Soc. Rev. **42**, 1784–1795 (2013).

[82] https://github.com/deepmodeling/abacus-develop/pull/3226 (2024).

[83] M. Methfessel and A. T. Paxton, "High-precision sampling for brillouin-zone integration in metals," Phys. Rev. B **40**, 3616–3621 (1989).

[84] E. Bitzek, P. Koskinen, F. Gähler, M. Moseler, and P. Gumbsch, "Structural relaxation made simple," Phys. Rev. Lett. **97**, 170201 (2006).

[85] Y. Liu, Y. Zhang, N. Xiao, X. Li, F.-Z. Dai, and M. Chen, "Investigating interfacial segregation of ω/Al in Al–Cu alloys: A comprehensive study using density functional theory and machine learning," Acta Mater. **279**, 120294 (2024).

[86] Y. Liu, X. Liu, and M. Chen, "Copper-doped beryllium and beryllium oxide interface: A first-principles study," J. Nucl. Mater. **545**, 152733 (2021).

[87] Y. Liu, X. Ding, M. Chen, and S. Xu, "A caveat of the charge-extrapolation scheme for modeling electrochemical reactions on semiconductor surfaces: an issue induced by a discontinuous fermi level change," Phys. Chem. Chem. Phys. **24**, 15511–15521 (2022).

[88] D. Chen, Y. Liu, Y. Zheng, H. Zhuang, M. Chen, and Y. Jiao, "Disordered hyperuniform quasi-one-dimensional materials," Phys. Rev. B **106**, 235427 (2022).

[89] Y. Liu and M. Chen, "Multihyperuniformity in high entropy MXenes," arXiv preprint arXiv:2410.13145 (2024).

[90] J. E. Jones and S. Chapman, "On the determination of molecular fields. -i. from the variation of the viscosity of a gas with temperature," Proc. R. Soc. Lond. **106**, 441–462 (1924).

[91] J. E. Jones and S. Chapman, "On the determination of molecular fields. -ii. from the equation of state of a gas," Proc. R. Soc. Lond. **106**, 463–477 (1924).

[92] J. Zeng, D. Zhang, D. Lu, P. Mo, Z. Li, Y. Chen, M. Rynik, L. Huang, Z. Li, S. Shi, Y. Wang, H. Ye, P. Tuo, J. Yang, Y. Ding, Y. Li, D. Tisi, Q. Zeng, H. Bao, Y. Xia, J. Huang, K. Muraoka, Y. Wang, J. Chang, F. Yuan, S. L. Bore, C. Cai, Y. Lin, B. Wang, J. Xu, J.-X. Zhu, C. Luo, Y. Zhang, R. E. A. Goodall, W. Liang, A. K. Singh, S. Yao, J. Zhang, R. Wentzcovitch, J. Han, J. Liu, W. Jia, D. M. York, W. E, R. Car, L. Zhang, and H. Wang, "DeePMD-kit v2: A software package for deep potential models," J. Chem. Phys. **159**, 054801 (2023).

[93] W. C. Swope, H. C. Andersen, P. H. Berens, and K. R. Wilson, "A computer simulation method for the calculation of equilibrium constants for the formation of physical clusters of molecules: Application to small water clusters," J. Chem. Phys. **76**, 637–649 (1982).

[94] D. J. T. Glenn J. Martyna, Mark E. Tuckerman and M. L. Klein, "Explicit reversible integrators for extended systems dynamics," Mol. Phys. **87**, 1117–1157 (1996).

[95] S. Nosé, "A unified formulation of the constant temperature molecular dynamics methods," J. Chem. Phys. **81**, 511–519 (1984).

[96] W. G. Hoover, "Canonical dynamics: Equilibrium phase-space distributions," Phys. Rev. A **31**, 1695–1697 (1985).

[97] G. J. Martyna, M. L. Klein, and M. Tuckerman, "Nosé–Hoover chains: The canonical ensemble via continuous dynamics," J. Chem. Phys. **97**, 2635–2643 (1992).

[98] T. Schneider and E. Stoll, "Molecular-dynamics study of a three-dimensional one-component model for distortive phase transitions," Phys. Rev. B **17**, 1302–1322 (1978).

[99] T. Chen, Q. Liu, Y. Liu, L. Sun, and M. Chen, "Combining stochastic density functional theory with deep potential molecular dynamics to study warm dense matter," Matter. Radiat. Extremes **9**, 015604 (2024).

[100] X. Liu, D. Zheng, X. Ren, L. He, and M. Chen, "First-principles molecular dynamics study of deuterium diffusion in liquid Tin," J. Chem. Phys. **147**, 064505 (2017).

[101] Q. Wang, D. Zheng, L. He, and X. Ren, "Cooperative effect in a graphite intercalation compound: Enhanced mobility of AlCl4 in the graphite cathode of Aluminum-Ion batteries," Phys. Rev. Appl. **12**, 044060 (2019).

[102] X. Liu, Y. Qi, D. Zheng, C. Zhou, L. He, and F. Huang, "Diffusion coefficients of mg isotopes in mgsio3 and Mg_2SiO_4 melts calculated by first-principles molecular dynamics simulations," Geochim. Cosmochim. Acta **223**, 364–376 (2018).

[103] Q. Wang, D. Zheng, L. He, and X. Ren, "Peculiar diffusion behavior of alcl4 intercalated in graphite from nanosecond-long molecular dynamics simulations," Chin. Phys. B **30**, 107102 (2021).

[104] D. Zheng, Z.-X. Shen, M. Chen, X. Ren, and L. He, "Retention and recycling of deuterium in liquid lithium-tin slab studied by first-principles molecular dynamics," J. Nucl. Mater. **543**, 152542 (2021).

[105] Q. Wang, D. Zheng, L. He, and X. Ren, "Cooperative Effect in a graphite intercalation compound: Enhanced Mobility of alcl4 in the Graphite Cathode of Aluminum-Ion Batteries," Phys. Rev. Appl. **12**, 044060 (2019).

[106] A. Blanchet, F. Soubiran, M. Torrent, and J. Clérouin, "Extended first-principles molecular dynamics simulations of hot dense boron: equation of state and ionization," Contributions to Plasma Physics **62**, e202100234 (2022).

[107] V. V. Karasiev, J. W. Dufty, and S. Trickey, "Nonempirical semilocal free-energy density functional for matter under extreme conditions," Phys. Rev. Lett. **120**, 076401 (2018).

[108] Y. Zhang, C. Gao, Q. Liu, L. Zhang, H. Wang, and M. Chen, "Warm dense matter simulation via electron temperature dependent deep potential molecular dynamics," Phys. Plasmas **27** (2020).

[109] C. Ma, M. Chen, Y. Xie, Q. Xu, W. Mi, Y. Wang, and Y. Ma, "Nonlocal free-energy density functional for a broad range of warm dense matter simulations," Phys. Rev. B **110**, 085113 (2024).

[110] W. Mi, X. Shao, C. Su, Y. Zhou, S. Zhang, Q. Li, H. Wang, L. Zhang, M. Miao, Y. Wang, *et al.*, "Atlas: A real-space finite-difference imple-mentation of orbital-free density functional theory," Comput. Phys. Comm. **200**, 87–95 (2016).

[111] K. Mathew, R. Sundararaman, K. Letchworth-Weaver, T. A. Arias, and R. G. Hennig, "Implicit solvation model for density-functional study of nanocrystal surfaces and reaction pathways," J. Chem. Phys. **140**, 9519–825 (2014).

[112] S. A. Petrosyan, A. A. Rigos, and T. A. Arias, "Joint density-functional theory: ab initio study of Cr_2O_3 surface chemistry in solution." J. Phys. Chem. B **109**, 15436–15444 (2005).

[113] K. Mathew, V. Kolluru, S. Mula, S. N. Steinmann, and R. G. Hennig, "Implicit self-consistent electrolyte model in plane-wave density-functional theory," J. Chem. Phys. **151** (2019).

[114] L. Bengtsson, "Dipole correction for surface supercell calculations," Phys. Rev. B **59**, 12301–12304 (1999).

[115] T. Brumme, M. Calandra, and F. Mauri, "Electrochemical doping of few-layer zrncl from first principles: Electronic and structural properties in field-effect configuration," Phys. Rev. B **89**, 245406 (2014).

[116] M. Sun, B. Jin, X. Yang, and S. Xu, "Proton tunneling: A new insight into proton-coupled electron transfer in electrocatalytic hydrogen evolution reactions," arXiv e-prints , arXiv–2407 (2024).

[117] H. Hellmann, "A combined approximation method for the energy calculation in the many-electron problem," Acta Physicochim. URSS **1**, 913 (1935).

[118] R. P. Feynman, "Forces in molecules," Phys. Rev. **56**, 340–343 (1939).

[119] W. Jia, J. Fu, Z. Cao, L. Wang, X. Chi, W. Gao, and L.-W. Wang, "Fast plane wave density functional theory molecular dynamics calculations on multi-GPU machines," J. Comput. Phys. **251**, 102–115 (2013).

[120] S. Maintz and M. Wetzstein, "Strategies to accelerate vasp with gpus using open acc," Proceedings of the Cray User Group (2018).

[121] https://bohrium.dp.tech/en-US (2024).

[122] https://deepmodeling-activity.github.io/abacus-test.github.io/index.html?pname=bda (2024).

[123] R. Baer, D. Neuhauser, and E. Rabani, "Self-averaging stochastic kohn-sham density-functional theory," Phys. Rev. Lett. **111**, 106402 (2013).

[124] Y. Cytter, E. Rabani, D. Neuhauser, and R. Baer, "Stochastic density functional theory at finite temperatures," Phys. Rev. B **97**, 115207 (2018).

[125] D. Neuhauser, R. Baer, and E. Rabani, "Communication: Embedded fragment stochastic density functional theory," J. Chem. Phys. **141**, 041102 (2014).

[126] E. Arnon, E. Rabani, D. Neuhauser, and R. Baer, "Equilibrium configurations of large nanostructures using the embedded saturated-fragments stochastic density functional theory," J. Chem. Phys. **146**, 224111 (2017).

[127] M. Chen, R. Baer, D. Neuhauser, and E. Rabani, "Overlapped embedded fragment stochastic density functional theory for covalently-bonded materials," J. Chem. Phys. **150**, 034106 (2019).

[128] W. Li, M. Chen, E. Rabani, R. Baer, and D. Neuhauser, "Stochastic embedding DFT: Theory and application to p-nitroaniline in water," J. Chem. Phys. **151**, 174115 (2019).

[129] M. Chen, R. Baer, D. Neuhauser, and E. Rabani, "Energy window stochastic density functional theory," J. Chem. Phys. **151**, 114116 (2019).

[130] A. J. White and L. A. Collins, "Fast and universal kohn-sham density functional theory algorithm for warm dense matter to hot dense plasma," Phys. Rev. Lett. **125**, 055002 (2020).

[131] M. Hutchinson, "A stochastic estimator of the trace of the influence matrix for laplacian smoothing splines," Comm. Stat. Sim. Comp. **18**, 1059–1076 (1989).

[132] W. Zhou and S. Yuan, "A time-dependent random state approach for large-scale density functional calculations," Chin. Phys. Lett. **40**, 027101 (2023).

[133] R. Baer, D. Neuhauser, and E. Rabani, "Stochastic vector techniques in ground-state electronic structure," Annu. Rev. Phys. Chem. **73** (2022).

[134] Q. Liu and M. Chen, "Plane-wave-based stochastic-deterministic density functional theory for extended systems," Phys. Rev. B **106**, 125132 (2022).

[135] Y. A. Wang and E. A. Carter, *Theoretical Methods in Condensed Phase Chemistry* (Springer, 2002) p. 117.

[136] V. V. Karasiev and S. B. Trickey, "Issues and challenges in orbital-free density functional calculations," Comput. Phys. Commun. **183**, 2519–2527 (2012).

[137] H. Jiang and W. Yang, "Conjugate-gradient optimization method for orbital-free density functional calculations," J. Chem. Phys. **121**, 2030–2036 (2004).

[138] J. Nocedal, "Updating quasi-newton matrices with limited storage," Math. Comput. **35**, 773–782 (1980).

[139] W. W. Hager and H. Zhang, "A new conjugate gradient method with guaranteed descent and an efficient line search," SIAM Journal on optimization **16**, 170–192 (2005).

[140] J. C. Gilbert and J. Nocedal, "Global convergence properties of conjugate gradient methods for optimization," SIAM Journal on optimization **2**, 21–42 (1992).

[141] L. H. Thomas, "The calculation of atomic fields," in *Mathematical proceedings of the Cambridge philosophical society*, Vol. 23 (Cambridge University Press, 1927) pp. 542–548.

[142] E. Fermi, "Statistical method to determine some properties of atoms," Rend. Accad. Naz. Lincei **6**, 5 (1927).

[143] C. v. Weizsäcker, "Zur theorie der kernmassen," Zeitschrift für Physik **96**, 431–458 (1935).

[144] A. Berk, "Lower-bound energy functionals and their application to diatomic systems," Phys. Rev. A **28**, 1908 (1983).

[145] L.-W. Wang and M. P. Teter, "Kinetic-energy functional of the electron density," Phys. Rev. B **45**, 13196 (1992).

[146] K. Luo, V. V. Karasiev, and S. Trickey, "A simple generalized gradient approximation for the noninteracting kinetic energy density functional," Phys. Rev. B **98**, 041111 (2018).

[147] Q. Xu, C. Ma, W. Mi, Y. Wang, and Y. Ma, "Nonlocal pseudopotential energy density functional for orbital-free density functional theory," Nat. Commun. **13**, 1385 (2022).

[148] C. Huang and E. A. Carter, "Transferable local pseudopotentials for magnesium, aluminum and silicon," Phys. Chem. Chem. Phys. **10**, 7109–7120 (2008).

[149] Y.-C. Chi and C. Huang, "High-quality local pseudopotentials for metals," J. Chem. Theory Comput. **20**, 3231–3241 (2024).

[150] W. C. Witt, G. Beatriz, J. M. Dieterich, and E. A. Carter, "Orbital-free density functional theory for materials research," J. Mater. Res. **33**, 777–795 (2018).

[151] L. A. Constantin, E. Fabiano, and F. Della Sala, "Semilocal pauli–gaussian kinetic functionals for orbital-free density functional theory calculations of solids," J. Phys. Chem. Lett. **9**, 4385–4390 (2018).

[152] D. Kang, K. Luo, K. Runge, and S. Trickey, "Two-temperature warm dense hydrogen as a test of quantum protons driven by orbital-free density functional theory electronic forces," Matter Radiat. at Extremes **5**, 064403 (2020).

[153] Y. A. Wang, N. Govind, and E. A. Carter, "Orbital-free kinetic-energy density functionals with a density-dependent kernel," Phys. Rev. B **60**, 16350 (1999).

[154] C. Huang and E. A. Carter, "Nonlocal orbital-free kinetic energy density functional for semiconductors," Phys. Rev. B **81**, 045206 (2010).

[155] W. Mi, A. Genova, and M. Pavanello, "Nonlocal kinetic energy functionals by functional integration," J. Chem. Phys. **148**, 184107 (2018).

[156] X. Shao, W. Mi, and M. Pavanello, "Revised huang-carter nonlocal kinetic energy functional for semiconductors and their surfaces," Phys. Rev. B **104**, 045118 (2021).

[157] L. Sun, Y. Li, and M. Chen, "Truncated nonlocal kinetic energy density functionals for simple metals and silicon," Phys. Rev. B **108**, 075158 (2023).

[158] A. Bhattacharjee, S. Jana, and P. Samal, "First step toward a parameter-free, nonlocal kinetic energy density functional for semiconductors and simple metals," J. Chem. Phys. **160** (2024).

[159] M. Levy and H. Ou-Yang, "Exact properties of the pauli potential for the square root of the electron density and the kinetic energy functional," Phys. Rev. A **38**, 625 (1988).

[160] J. C. Snyder, M. Rupp, K. Hansen, K.-R. Müller, and K. Burke, "Finding density functionals with machine learning," Phys. Rev. Lett. **108**, 253002 (2012).

[161] J. Seino, R. Kageyama, M. Fujinami, Y. Ikabata, and H. Nakai, "Semilocal machine-learned kinetic energy density functional with third-order gradients of electron density," J. Chem. Phys. **148** (2018).

[162] R. Meyer, M. Weichselbaum, and A. W. Hauser, "Machine learning approaches toward orbital-free density functional theory: Simultaneous training on the kinetic energy density functional and its functional derivative," J. Chem. Theory Comput. **16**, 5685–5694 (2020).

[163] F. Imoto, M. Imada, and A. Oshiyama, "Order-N orbital-free density-functional calculations with machine learning of functional derivatives for semiconductors and metals," Phys. Rev. Research **3**, 033198 (2021).

[164] K. Ryczko, S. J. Wetzel, R. G. Melko, and I. Tamblyn, "Toward orbital-free density functional theory with small data sets and deep learning," J. Chem. Theory Comput. **18**, 1122–1128 (2022).

[165] H. Zhang, S. Liu, J. You, C. Liu, S. Zheng, Z. Lu, T. Wang, N. Zheng, and B. Shao, "Overcoming the barrier of orbital-free density functional theory for molecular systems using deep learning," Nat. Comput. Sci. **4**, 210–223 (2024).

[166] L. Sun and M. Chen, "Machine learning based nonlocal kinetic energy density functional for simple metals and alloys," Phys. Rev. B **109**, 115135 (2024).

[167] K. M. Carling and E. A. Carter, "Orbital-free density functional theory calculations of the properties of Al, Mg and Al–Mg crystalline phases," Model. Simul. Mater. Sci. Eng. **11**, 339 (2003).

[168] A. Jain, S. P. Ong, G. Hautier, W. Chen, W. D. Richards, S. Dacek, S. Cholia, D. Gunter, D. Skinner, G. Ceder, *et al.*, "Commentary: The materials project: A materials genome approach to accelerating materials innovation," APL Mater. **1** (2013).

[169] J. D. Talman, "Numerical Fourier and Bessel transforms in logarithmic variables," J. Comput. Phys. **29**, 35–48 (1978).

[170] O. A. Sharafeddin, H. Ferrel Bowen, D. J. Kouri, and D. K. Hoffman, "Numerical evaluation of spherical bessel transforms via fast Fourier transforms," J. Comput. Phys. **100**, 294–296 (1992).

[171] M. Toyoda and T. Ozaki, "Fast spherical Bessel transform via fast Fourier transform and recurrence formula," Comput. Phys. Commun. **181**, 277–282 (2010).

[172] A. Cerioni, L. Genovese, A. Mirone, and V. A. Sole, "Efficient and accurate solver of the three-dimensional screened and unscreened Poisson's equation with generic boundary conditions," J. Chem. Phys. **137**, 134108 (2012).

[173] J. M. Soler, E. Artacho, J. D. Gale, A. García, J. Junquera, P. Ordejón, and D. Sánchez-Portal, "The SIESTA method for ab initio order-N materials simulation," J. Phys. Condens. Matter **14**, 2745 (2002).

[174] O. F. Sankey and D. J. Niklewski, "Ab initio multicenter tight-binding model for molecular-dynamics simulations and other applications in covalent systems," Phys. Rev. B **40**, 3979–3995 (1989).

[175] D. Porezag, Th. Frauenheim, Th. Köhler, G. Seifert, and R. Kaschner, "Construction of tight-binding-like potentials on the basis of density-functional theory: Application to carbon," Phys. Rev. B **51**, 12947–12957 (1995).

[176] A. P. Horsfield, "Efficient ab initio tight binding," Phys. Rev. B **56**, 6594–6602 (1997).

[177] J. Junquera, Ó. Paz, D. Sánchez-Portal, and E. Artacho, "Numerical atomic orbitals for linear-scaling calculations," Phys. Rev. B **64**, 235111 (2001).

[178] T. Ozaki, "Variationally optimized atomic orbitals for large-scale electronic structures," Phys. Rev. B **67**, 155108 (2003).

[179] T. Ozaki and H. Kino, "Numerical atomic basis orbitals from H to Kr," Phys. Rev. B **69**, 195113 (2004).

[180] D. Sanchez-Portal, E. Artacho, and J. M. Soler, "Projection of plane-wave calculations into atomic orbitals," Solid State Commun. **95**, 685–690 (1995).

[181] D. Sánchez-Portal, E. Artacho, and J. M. Soler, "Analysis of atomic orbital basis sets from the projection of plane-wave results," J. Phys. Condens. Matter **8**, 3859 (1996).

[182] P. D. Haynes and M. C. Payne, "Localised spherical-wave basis set for *O(N)* total-energy pseudopotential calculations," Comput. Phys. Commun. **102**, 17–27 (1997).

[183] Y. Liu, X. Ren, and L. He, "A DFT study of energetic and structural properties of a full turn of A-form DNA under relaxed and stretching conditions," J. Chem. Phys. **151**, 215102 (2019).

[184] M. Schlipf and F. Gygi, "Optimization algorithm for the generation of ONCV pseudopotentials," Comput. Phys. Commun. **196**, 36–44 (2015).

[185] ABACUS team, "CGH and LRH basis sets," https://abacus.ustc.edu.cn/pseudo/list.htm (2020).

[186] https://netlib.org/scalapack/ (2024).

[187] https://elpa.mpcdf.mpg.de/ (2024).

[188] V. W.-z. Yu, J. Moussa, P. Kuus, A. Marek, P. Messmer, M. Yoon, H. Lederer, and V. Blum, "GPU-acceleration of the ELPA2 distributed eigensolver for dense symmetric and hermitian eigenproblems," Comput. Phys. Commun. **262**, 107808 (2021).

[189] A. Tal, M. Marsman, G. Kresse, A. Anders, S. Rodriguez, K. Kim, A. Kalinkin, A. Romanenko, M. Noack, P. Atkinson, et al., "Solving millions of eigenvectors in large-scale quantum-many-body-theory computations," in ISC High Performance 2024 Research Paper Proceedings (39th International Conference) (Prometeus GmbH, 2024) pp. 1–11.

[190] A. Seidl, A. Görling, P. Vogl, J. A. Majewski, and M. Levy, "Generalized Kohn-Sham schemes and the band-gap problem," Phys. Rev. B **53**, 3764–3774 (1996).

[191] J. P. Perdew and K. Schmidt, "Jacob's ladder of density functional approximations for the exchange-correlation energy," AIP Conf. Proc. **577**, 1–20 (2001).

[192] J. P. Perdew and A. Zunger, "Self-interaction correction to density-functional approximations for many-electron systems," Phys. Rev. B **23**, 5048–5079 (1981).

[193] P. Mori-Sánchez, A. J. Cohen, and W. Yang, "Localization and Delocalization Errors in Density Functional Theory and Implications for Band-Gap Prediction," Phys. Rev. Lett. **100**, 146401 (2008).

[194] M. Ernzerhof and G. E. Scuseria, "Assessment of the Perdew–Burke–Ernzerhof exchange-correlation functional," J. Chem. Phys. **110**, 5029–5036 (1999).

[195] C. Adamo and V. Barone, "Toward reliable density functional methods without adjustable parameters: The PBE0 model," J. Chem. Phys. **110**, 6158–6170 (1999).

[196] K. Hui and J.-D. Chai, "SCAN-based hybrid and double-hybrid density functionals from models without fitted parameters," J. Chem. Phys. **144**, 044114 (2016).

[197] S. Lehtola, C. Steigemann, M. J. Oliveira, and M. A. Marques, "Recent developments in libxc — a comprehensive library of functionals for density functional theory," SoftwareX **7**, 1–5 (2018).

[198] M. Feyereisen, G. Fitzgerald, and A. Komornicki, "Use of approximate integrals in ab initio theory. an application in MP2 energy calculations," Chem. Phys. Lett. **208**, 359–363 (1993).

[199] O. Vahtras, J. Almlöf, and M. Feyereisen, "Integral approximations for LCAO-SCF calculations," Chem. Phys. Lett. **213**, 514–518 (1993).

[200] X. Ren, P. Rinke, V. Blum, J. Wieferink, A. Tkatchenko, A. Sanfilippo, K. Reuter, and M. Scheffler, "Resolution-of-identity approach to hartree–fock, hybrid density functionals, RPA, MP2 and GW with numeric atom-centered basis functions," New J. Phys. **14**, 053020 (2012).

[201] J. L. Whitten, "Coulombic potential energy integrals and approximations," J. Chem. Phys. **58**, 4496–4501 (1973).

[202] S. V. Levchenko, X. Ren, J. Wieferink, R. Johanni, P. Rinke, V. Blum, and M. Scheffler, "Hybrid functionals for large periodic systems in an all-electron, numeric atom-centered basis framework," Comput. Phys. Commun. **192**, 60–69 (2015).

[203] A. C. Ihrig, J. Wieferink, I. Y. Zhang, M. Ropo, X. Ren, P. Rinke, M. Scheffler, and V. Blum, "Accurate localized resolution of identity approach for linear-scaling hybrid density functionals and for many-body perturbation theory," New J. Phys. **17**, 093020 (2015).

[204] Y. Ji, P. Lin, X. Ren, and L. He, "Reproducibility of Hybrid Density Functional Calculations for Equation-of-State Properties and Band Gaps," J. Phys. Chem. A **126**, 5924–5931 (2022).

[205] M. Chen, G.-C. Guo, and L. He, "Systematically improvable optimized atomic basis sets for ab initio calculations," J. Phys. Condens. Matter **22**, 445501 (2010).

[206] M. Chen, G.-C. Guo, and L. He, "Electronic structure interpolation via atomic orbitals," J. Phys. Condens. Matter **23**, 325501 (2011).

[207] LibRI: https://github.com/abacusmodeling/LibRI (2024).

[208] LibRPA: https://github.com/Srlive1201/LibRPA (2024).

[209] Y. Ji, P. Lin, X. Ren, and L. He, "Geometric and electronic structures of $Cs_2BB'X_6$ double perovskites: The importance of exact exchange," Phys. Rev. Res. **6**, 033172 (2024).

[210] Z. Tang, H. Li, P. Lin, X. Gong, G. Jin, L. He, H. Jiang, X. Ren, W. Duan, and Y. Xu, "A deep equivariant neural network approach for efficient hybrid density functional calculations," Nat. Commun. **15**, 8815 (2024).

[211] Z.-H. Cui, Y.-C. Wang, M.-Y. Zhang, X. Xu, and H. Jiang, "Doubly screened hybrid functional: an accurate first-principles approach for both narrow-and wide-gap semiconductors," J. Phys. Chem. Lett. **9**, 2338–2345 (2018).

[212] B. Delley, "An all-electron numerical method for solving the local density functional for polyatomic molecules," J. Chem. Phys. **92**, 508–517 (1990).

[213] J. P. Perdew, "Jacob's ladder of density functional approximations for the exchange-correlation energy," in AIP Conf. Proc., Vol. 577 (AIP, Antwerp (Belgium), 2001) pp. 1–20.

[214] H. J. Kulik, T. Hammerschmidt, J. Schmidt, S. Botti, M. A. L. Marques, M. Boley, M. Scheffler, M. Todorović, P. Rinke, C. Oses, A. Smolyanyuk, S. Curtarolo, A. Tkatchenko, A. P. Bartók, S. Manzhos, M. Ihara, T. Carrington, J. Behler, O. Isayev, M. Veit, A. Grisafi, J. Nigam, M. Ceriotti, K. T. Schütt, J. Westermayr, M. Gastegger, R. J. Maurer, B. Kalita, K. Burke, R. Nagai, R. Akashi, O. Sugino, J. Hermann, F. Noé, S. Pilati, C. Draxl, M. Kuban, S. Rigamonti, M. Scheidgen, M. Esters, D. Hicks, C. Toher, P. V. Balachandran, I. Tamblyn, S. Whitelam, C. Bellinger, and L. M. Ghiringhelli, "Roadmap on Machine learning in electronic structure," Electron. Struct. **4**, 023004 (2022).

[215] B. Huang, G. F. Von Rudorff, and O. A. Von Lilienfeld, "The central role of density functional theory in the AI age," Science **381**, 170–175 (2023).

[216] Q. Ou, P. Tuo, W. Li, X. Wang, Y. Chen, and L. Zhang, "DeePKS Model for Halide Perovskites with the Accuracy of a Hybrid Functional," J. Phys. Chem. C **127**, 18755–18764 (2023).

[217] P. Zhang, A. T. Gardini, X. Xu, and M. Parrinello, "Intramolecular and Water Mediated Tautomerism of Solvated Glycine," J. Chem. Inf. Model. **64**, 3599–3604 (2024).

[218] Y. Zhao and D. G. Truhlar, "The M06 suite of density functionals for main group thermochemistry, thermochemical kinetics, noncovalent interactions, excited states, and transition elements: two new functionals and systematic testing of four M06-class functionals and 12 other functionals," Theor. Chem. Acc. **120**, 215–241 (2008).

[219] M. Invernizzi and M. Parrinello, "Rethinking metadynamics: from bias potentials to probability distributions," J. Phys. Chem. Lett. **11**, 2731–2736 (2020).

[220] P. Zhang and X. Xu, "Propensity of water self-ions at air (oil)-water interfaces revealed by deep potential molecular dynamics with enhanced sampling," arXiv preprint arXiv:2404.07027 (2024).

[221] M. J. Han, T. Ozaki, and J. Yu, "O(N) LDA+U electronic structure calculation method based on the nonorthogonal pseudoatomic orbital basis," Phys. Rev. B **73**, 045110 (2006).

[222] L. Messick, W. Walker, and R. Glosser, "Direct and temperature-modulated reflectance spectra of MnO, CoO, and NiO," Phys. Rev. B **6**, 3941 (1972).

[223] A. Cheetham and D. Hope, "Magnetic ordering and exchange effects in the antiferromagnetic solid solutions $Mn_xNi_{1-x}O$," Phys. Rev. B **27**, 6964 (1983).

[224] H. Bowen, D. Adler, and B. Auker, "Electrical and optical properties of feo," J. Solid. State Chem. **12**, 355–359 (1975).

[225] B. Fender, A. Jacobson, and F. Wedgwood, "Covalency parameters in MnO, α-MnS, and NiO," J. Chem. Phys. **48**, 990–994 (1968).

[226] R. Powell and W. Spicer, "Optical properties of NiO and CoO," Phys. Rev. B **2**, 2182 (1970).

[227] W. Roth, "Magnetic structures of MnO, FeO, CoO, and NiO," Phys. Rev. **110**, 1333 (1958).

[228] G. Sawatzky and J. Allen, "Magnitude and origin of the band gap in NiO," Phys. Rev. Lett. **53**, 2339 (1984).

[229] S. Hüfner, J. Osterwalder, T. Riesterer, and F. Hulliger, "Photoemission and inverse photoemission spectroscopy of NiO," Solid State Commun. **52**, 793–796 (1984).

[230] D. Khan and R. Erickson, "Magnetic form factor of Co++ ion in cobaltous oxide," Phys. Rev. B **1**, 2243 (1970).

[231] F. Tran, P. Blaha, K. Schwarz, and P. Novák, "Hybrid exchange-correlation energy functionals for strongly correlated electrons: Applications to transition-metal monoxides," Phys. Rev. B **74**, 155108 (2006).

[232] D. Bagayoko, "Understanding density functional theory (dft) and completing it in practice," AIP Adv. **4** (2014).

[233] E. Runge and E. K. Gross, "Density-functional theory for time-dependent systems," Phys. Rev. Lett. **52**, 997 (1984).

[234] J. Ren, E. Kaxiras, and S. Meng, "Optical properties of clusters and molecules from real-time time-dependent density functional theory using a self-consistent field," Mol. Phys. **108**, 1829–1844 (2010).

[235] I. Maliyov, J.-P. Crocombette, and F. Bruneval, "Electronic stopping power from time-dependent density-functional theory in gaussian basis," Eur. Phys. J. B **91**, 1–7 (2018).

[236] Y. Ren, Y. Fu, N. Li, C. You, J. Huang, K. Huang, Z. Sun, J. Zhou, Y. Si, Y. Zhu, W. Chen, L. Duan, and M. Liu, "Concentrated solar CO_2 reduction in H2O vapour with energy conversion efficiency," Nat. Commun. **15** (2024), 10.1038/s41467-024-49003-8.

[237] S. Meng and E. Kaxiras, "Real-time, local basis-set implementation of time-dependent density functional theory for excited state dynamics simulations," J. Chem. Phys. **129** (2008).

[238] C. Lian, M. Guan, S. Hu, J. Zhang, and S. Meng, "Photoexcitation in solids: First-principles quantum simulations by real-time TDDFT," Adv. Theory Simul. **1**, 1800055 (2018).

[239] N. J. Mason, J. M. Gingell, J. A. Davies, H. Zhao, I. C. Walker, and M. R. F. Siggel, "Vuv optical absorption and electron energy-loss spectroscopy of ozone," J. Phys. B **29**, 3075 (1996).

[240] W.-H. Liu, Y.-X. Gu, Z. Wang, S.-S. Li, L.-W. Wang, and J.-W. Luo, "Origin of immediate damping of coherent oscillations in photoinduced charge-density-wave transition," Phys. Rev. Lett. **130**, 146901 (2023).

[241] J. Sun, C.-W. Lee, A. Kononov, A. Schleife, and C. A. Ullrich, "Real-time exciton dynamics with time-dependent density-functional theory," Phys. Rev. Lett. **127**, 077401 (2021).

[242] P. You, D. Chen, X. Liu, C. Zhang, A. Selloni, and S. Meng, "Correlated electron–nuclear dynamics of photoinduced water dissociation on rutile TiO_2," Nat. Mater. **23**, 1100–1106 (2024).

[243] K. Onda, B. Li, J. Zhao, K. D. Jordan, J. Yang, and H. Petek, "Wet electrons at the H_2O/TiO_2(110) surface," Science **308**, 1154–1158 (2005).

[244] J. Chen, Y. Ren, Y. Fu, Y. Si, J. Huang, J. Zhou, M. Liu, L. Duan, and N. Li, "Integration of co single atoms and ni clusters on defect-rich zro2 for strong photothermal coupling boosts photocatalytic co2 reduction," ACS Nano **18**, 13035–13048 (2024).

[245] D. Zhang, H. Bi, F.-Z. Dai, W. Jiang, X. Liu, L. Zhang, and H. Wang, "Pretraining of attention-based deep learning potential model for molecular simulation," npj Comput. Mater. **10**, 94 (2024).

[246] D. Zhang, X. Liu, X. Zhang, C. Zhang, C. Cai, H. Bi, Y. Du, X. Qin, A. Peng, J. Huang, B. Li, Y. Shan, J. Zeng, Y. Zhang, S. Liu, Y. Li, J. Chang, X. Wang, S. Zhou, J. Liu, X. Luo, Z. Wang, W. Jiang, J. Wu, Y. Yang, J. Yang, M. Yang, F.-Q. Gong, L. Zhang, M. Shi, F.-Z. Dai, D. M. York, S. Liu, T. Zhu, Z. Zhong, J. Lv, J. Cheng, W. Jia, M. Chen, G. Ke, W. E, L. Zhang, and H. Wang, "DPA-2: A large atomic model as a multitask learner," npj Comput. Mater. **10**, 1–15 (2024).

[247] A. Jain, J. Montoya, S. Dwaraknath, N. E. Zimmermann, J. Dagdelen, M. Horton, P. Huck, D. Winston, S. Cholia, S. P. Ong, *et al.*, "The materials project: Accelerating materials design through theory-driven data and tools," *Handbook of Materials Modeling: Methods: Theory and Modeling*, 1751–1784 (2020).

[248] L. Talirz, S. Kumbhar, E. Passaro, A. V. Yakutovich, V. Granata, F. Gargiulo, M. Borelli, M. Uhrin, S. P. Huber, S. Zoupanos, *et al.*, "Materials cloud, a platform for open computational science," Sci. Data **7**, 299 (2020).

[249] D. D. Landis, J. S. Hummelshøj, S. Nestorov, J. Greeley, M. Dułak, T. Bligaard, J. K. Nørskov, and K. W. Jacobsen, "The computational materials repository," Comput. Sci. Eng. **14**, 51–57 (2012).

[250] K. Lejaeghere, G. Bihlmayer, T. Björkman, P. Blaha, S. Blügel, V. Blum, D. Caliste, I. E. Castelli, S. J. Clark, A. D. Corso, S. de Gironcoli, T. Deutsch, J. K. Dewhurst, I. D. Marco, C. Draxl, M. Dułak, O. Eriksson, J. A. Flores-Livas, K. F. Garrity, L. Genovese, P. Giannozzi, M. Giantomassi, S. Goedecker, X. Gonze, O. Grånäs, E. K. U. Gross, A. Gulans, F. Gygi, D. R. Hamann, P. J. Hasnip, N. A. W. Holzwarth, D. Iuşan, D. B. Jochym, F. Jollet, D. Jones, G. Kresse, K. Koepernik, E. Küçükbenli, Y. O. Kvashnin, I. L. M. Locht, S. Lubeck, M. Marsman, N. Marzari, U. Nitzsche, L. Nordström, T. Ozaki, L. Paulatto, C. J. Pickard, W. Poelmans, M. I. J. Probert, K. Refson, M. Richter, G.-M. Rignanese, S. Saha, M. Scheffler, M. Schlipf, K. Schwarz, S. Sharma, F. Tavazza, P. Thunström, A. Tkatchenko, M. Torrent, D. Vanderbilt, M. J. van Setten, V. V. Speybroeck, J. M. Wills, J. R. Yates, G.-X. Zhang, and S. Cottenier, "Reproducibility in density functional theory calculations of solids," Science **351**, aad3000 (2016).

[251] N. A. W. Holzwarth, M. Torrent, J.-B. Charraud, and M. Côté, "Cubic spline solver for generalized density functional treatments of atoms and generation of atomic datasets for use with exchange-correlation functionals including meta-gga," Phys. Rev. B **105**, 125144 (2022).

[252] SG15 ONCV Potentials, http://www.quantum-simulation.org/potentials/sg15_oncv/.

[253] Pseudo Dojo, http://www.pseudo-dojo.org/.

[254] PWmat-website, https://www.pwmat.com/potential-download.

[255] M. Krack, "Pseudopotentials for h to kr optimized for gradient-corrected exchange-correlation functionals," Theor. Chem. Acc. **114**, 145–152 (2005).

[256] theos-pp, http://theossrv1.epfl.ch/Main/Pseudopotentials.

[257] K. F. Garrity, J. W. Bennett, K. M. Rabe, and D. Vanderbilt, "Pseudopotentials for high-throughput DFT calculations," Comput. Mater. Sci. **81**, 446–452 (2014).

[258] GBRV pseudopotentials, https://www.physics.rutgers.edu/gbrv/.

[259] C. W. Andersen, R. Armiento, E. Blokhin, G. J. Conduit, S. Dwaraknath, M. L. Evans, Á. Fekete, A. Gopakumar, S. Gražulis, A. Merkys, *et al.*, "Optimade, an api for exchanging materials data," Sci. Data **8**, 217 (2021).

[260] S. Gražulis, D. Chateigner, R. T. Downs, A. Yokochi, M. Quirós, L. Lutterotti, E. Manakova, J. Butkus, P. Moeck, and A. Le Bail, "Crystallography open database–an open-access collection of crystal structures," J. Appl. Crystallogr. **42**, 726–729 (2009).

[261] A. Togo, K. Shinohara, and I. Tanaka, "Spglib: a software library for crystal symmetry search," Sci. Technol. Adv. Mater.: Methods , 2384822 (2024).

[262] Y. Hinuma, G. Pizzi, Y. Kumagai, F. Oba, and I. Tanaka, "Band structure diagram paths based on crystallography," Comput. Mater. Sci. **128**, 140–184 (2017).

[263] G. Prandini, A. Marrazzo, I. E. Castelli, N. Mounet, and N. Marzari, "Precision and efficiency in solid-state pseudopotential calculations," npj Comput. Mater. **4**, 72 (2018).

[264] K. Lejaeghere, V. Van Speybroeck, G. Van Oost, and S. Cottenier, "Error estimates for solid-state density-functional theory predictions: an overview by means of the ground-state elemental crystals," Critical reviews in solid state and materials sciences **39**, 1–24 (2014).

[265] F. Birch, "Finite elastic strain of cubic crystals," Phys. Rev. **71**, 809 (1947).

[266] J. Wu, J. Yang, Y.-J. Liu, D. Zhang, Y. Yang, Y. Zhang, L. Zhang, and S. Liu, "Universal interatomic potential for perovskite oxides," Phys. Rev. B **108**, L180104 (2023).

[267] J. Wu, J. Yang, L. Ma, L. Zhang, and S. Liu, "Modular development of deep potential for complex solid solutions," Phys. Rev. B **107**, 144102 (2023).

[268] F.-H. Gong, Y.-L. Tang, Y.-L. Zhu, H. Zhang, Y.-J. Wang, Y.-T. Chen, Y.-P. Feng, M.-J. Zou, B. Wu, W.-R. Geng, *et al.*, "Atomic mapping of periodic dipole waves in ferroelectric oxide," Sci. Adv. **7**, eabg5503 (2021).

[269] J. Liu, X. Zhang, T. Chen, Y. Zhang, D. Zhang, L. Zhang, and M. Chen, "Machine-learning-based interatomic potentials for group IIB to VIA semiconductors: Toward a universal model," J. Chem. Theory Comput. (2024).

[270] https://github.com/ZLI-afk/static/tree/main/storage/abacus_alloy_pp (2024).

[271] Y. Zhang, H. Wang, W. Chen, J. Zeng, L. Zhang, H. Wang, and W. E, "DP-GEN: A concurrent learning platform for the generation of reliable deep learning based potential energy models," Comput. Phys. Commun. **253**, 107206 (2020).

[272] Z. Li, T. Wen, Y. Zhang, X. Liu, C. Zhang, A. S. L. S. Pattamatta, X. Gong, B. Ye, H. Wang, L. Zhang, and D. J. Srolovitz, "An extendable cloud-native alloy property explorer," (2024), arXiv:2404.17330 [cond-mat.mtrl-sci].

[273] I. Batatia, P. Benner, Y. Chiang, A. M. Elena, D. P. Kovács, J. Riebesell, X. R. Advincula, M. Asta, M. Avaylon, W. J. Baldwin, F. Berger, N. Bernstein, A. Bhowmik, S. M. Blau, V. Cărare, J. P. Darby, S. De, F. D. Pia, V. L. Deringer, R. Elijošius, Z. El-Machachi, F. Falcioni, E. Fako, A. C. Ferrari, A. Genreith-Schriever, J. George, R. E. A. Goodall, C. P. Grey, P. Grigorev, S. Han, W. Handley, H. H. Heenen, K. Hermansson, C. Holm, J. Jaafar, S. Hofmann, K. S. Jakob, H. Jung, V. Kapil, A. D. Kaplan, N. Karimitari, J. R. Kermode, N. Kroupa, J. Kullgren, M. C. Kuner, D. Kuryla, G. Liepuoniute, J. T. Margraf, I.-B. Magdău, A. Michaelides, J. H. Moore, A. A. Naik, S. P. Niblett, S. W. Norwood, N. O'Neill, C. Ortner, K. A. Persson, K. Reuter, A. S. Rosen, L. L. Schaaf, C. Schran,

B. X. Shi, E. Sivonxay, T. K. Stenczel, V. Svahn, C. Sutton, T. D. Swinburne, J. Tilly, C. van der Oord, E. Varga-Umbrich, T. Vegge, M. Vondrák, Y. Wang, W. C. Witt, F. Zills, and G. Csányi, "A foundation model for atomistic materials chemistry," (2024), arXiv:2401.00096 [physics.chem-ph].

[274] A. Togo, L. Chaput, T. Tadano, and I. Tanaka, "Implementation strategies in phonopy and phono3py," J. Phys. Condens. Matter 35, 353001 (2023).

[275] A. Togo, "First-principles phonon calculations with phonopy and phono3py," J. Phys. Soc. Jpn. 92, 012001 (2023).

[276] L. Zhang, J. Han, H. Wang, W. A. Saidi, R. Car, and E. Weinan, "End-to-end symmetry preserving inter-atomic potential energy model for finite and extended systems," in *Proceedings of the 32nd International Conference on Neural Information Processing Systems*, NIPS'18 (Curran Associates Inc., 2018) p. 4441–4451.

[277] https://github.com/deepmodeling/dpdata (2024).

[278] L. Zhang, D.-Y. Lin, H. Wang, R. Car, and W. E, "Active learning of uniformly accurate interatomic potentials for materials simulation," Phys. Rev. Mater. 3, 023804 (2019).

[279] H. Li, Z. Wang, N. Zou, M. Ye, R. Xu, X. Gong, W. Duan, and Y. Xu, "Deep-learning density functional theory hamiltonian for efficient ab initio electronic-structure calculation," Nat. Comput. Sci. 2, 367–377 (2022).

[280] W. Kohn, "Density functional and density matrix method scaling linearly with the number of atoms," Phys. Rev. Lett. 76, 3168 (1996).

[281] X. Gong, H. Li, N. Zou, R. Xu, W. Duan, and Y. Xu, "General framework for E(3)-equivariant neural network representation of density functional theory Hamiltonian," Nat. Commun. 14, 2848 (2023).

[282] H. Li, Z. Tang, J. Fu, W.-H. Dong, N. Zou, X. Gong, W. Duan, and Y. Xu, "Deep-learning density functional perturbation theory," Phys. Rev. Lett. 132, 096401 (2024).

[283] DeepH, https://github.com/mzjb/DeepH-pack.

[284] DeepH-E3, https://github.com/Xiaoxun-Gong/DeepH-E3.

[285] Y. Wang, H. Li, Z. Tang, H. Tao, Y. Wang, Z. Yuan, Z. Chen, W. Duan, and Y. Xu, "DeepH-2: Enhancing deep-learning electronic structure via an equivariant local-coordinate transformer," arXiv:2401.17015 (2024).

[286] S. Yang, J. Chen, C.-F. Liu, and M. Chen, "Evolution of flat bands in MoSe$_2$/WSe$_2$ moiré lattices: A study combining machine learning and band unfolding methods," Phys. Rev. B 110, 235410 (2024).

[287] H. Li, Z. Tang, X. Gong, N. Zou, W. Duan, and Y. Xu, "Deep-learning electronic-structure calculation of magnetic superstructures," Nat. Comput. Sci. 3, 321 (2023).

[288] Z. Tang, H. Li, P. Lin, X. Gong, G. Jin, L. He, H. Jiang, X. Ren, W. Duan, and Y. Xu, "Code and dataset for the article "A deep equivariant neural network approach for efficient hybrid density functional calculations"," (2023).

[289] X. Gong, S. G. Louie, W. Duan, and Y. Xu, "Generalizing deep learning electronic structure calculation to the plane-wave basis," Nat. Comput. Sci. , 1–9 (2024).

[290] Y. Wang, Y. Li, Z. Tang, H. Li, Z. Yuan, H. Tao, N. Zou, T. Bao, X. Liang, Z. Chen, *et al.*, "Universal materials model of deep-learning density functional theory hamiltonian," Sci. Bull. 69, 2514 (2024).

[291] Q. Gu, Z. Zhouyin, S. K. Pandey, P. Zhang, L. Zhang, and W. E, "Deep learning tight-binding approach for large-scale electronic simulations at finite temperatures with ab initio accuracy," Nat. Commun. 15, 6772 (2024).

[292] Z. Zhouyin, Z. Gan, S. K. Pandey, L. Zhang, and Q. Gu, "Learning local equivariant representations for quantum operators," (2024), arXiv:2407.06053 [cond-mat, physics:quant-ph].

[293] J. Zou, Z. Zhouyin, D. Lin, L. Zhang, S. Hou, and Q. Gu, "Deep Learning Accelerated Quantum Transport Simulations in Nanoelectronics: From Break Junctions to Field-Effect Transistors," (2024), arXiv:2411.08800.

[294] G. Jin, H. Pang, Y. Ji, Z. Dai, and L. He, "PYATB: An efficient python package for electronic structure calculations using ab initio tight-binding model," Comput. Phys. Commun. 291, 108844 (2023).

[295] D. Xiao, M.-C. Chang, and Q. Niu, "Berry phase effects on electronic properties," Rev. Mod. Phys. 82, 1959–2007 (2010).

[296] M. Z. Hasan and C. L. Kane, "Colloquium: Topological insulators," Rev. Mod. Phys. 82, 3045–3067 (2010).

[297] B. I. Sturman and V. M. Fridkin, *The Photovoltaic and Photorefractive Effects in Noncentrosymmetric Materials* (Gordon and Breach Science Publishers, 1992).

[298] J. E. Sipe and A. I. Shkrebtii, "Second-order optical response in semiconductors," Phys. Rev. B 61, 5337–5352 (2000).

[299] G. Jin and L. He, "Peculiar band geometry induced giant shift current in ferroelectric snte monolayer," npj Comput. Mater. 10, 23.

[300] I. Sodemann and L. Fu, "Quantum nonlinear hall effect induced by berry curvature dipole in time-reversal invariant materials," Phys. Rev. Lett. 115, 216806 (2015).

[301] H. Pang, G. Jin, and L. He, "Tuning of berry-curvature dipole in TaAs slabs: An effective route to enhance the nonlinear hall response," Phys. Rev. Materials 8, 043403.

[302] G. Jin, D. Zheng, and L. He, "Calculation of berry curvature using non-orthogonal atomic orbitals," J. Phys. Condens. Matter 33, 325503 (2021).

[303] Q. Zheng, W. Chu, C. Zhao, L. Zhang, H. Guo, Y. Wang, X. Jiang, and J. Zhao, "*Ab Initio* Nonadiabatic Molecular Dynamics Investigations on the Excited Carriers in Condensed Matter Systems," Wires Comput. Mol. Sci. 9, e1411 (2019).

[304] Z. Zheng, Q. Zheng, and J. Zhao, "Spin-orbit Coupling Induced Demagnetization in Ni: *Ab Initio* Nonadiabatic Molecular Dynamics Perspective," Phys. Rev. B 105, 085142 (2022).

[305] X. Jiang, Q. Zheng, Z. Lan, W. A. Saidi, X. Ren, and J. Zhao, "Real-Time GW-BSE Investigations on Spin-Valley Exciton Dynamics in Monolayer Transition Metal Dichalcogenide," Sci. Adv. 7, eabf3759 (2021).

[306] Z. Zheng, Y. Shi, J.-J. Zhou, O. V. Prezhdo, Q. Zheng, and J. Zhao, "*Ab Initio* Real-time Quantum Dynamics of Charge Carriers in Momentum Space," Nat. Comput. Sci. 3, 532–541 (2023).

[307] https://abacus.deepmodeling.com/en/v3.5.2/advanced/interface/Hefei-NAMD.html (2024).

[308] L. Lin, J. Lu, L. Ying, R. Car, and W. E, "Fast algorithm for extracting the diagonal of the inverse matrix with application to the electronic structure analysis of metallic systems," Comm. Math. Sci. 7, 755 (2009).

[309] L. Lin, M. Chen, C. Yang, and L. He, "Accelerating atomic orbital-based electronic structure calculation via pole expansion and selected inversion," J. Phys. Condens. Matter 25, 295501 (2013).

[310] https://wiki.fysik.dtu.dk/ase (2024).

[311] https://gitlab.com/1041176461/ase-abacus (2024).

[312] H. Jónsson, G. Mills, and K. W. Jacobsen, "Nudged elastic band method for finding minimum energy paths of transitions," in *Classical and quantum dynamics in condensed phase simulations* (World Scientific, 1998) pp. 385–404.

[313] G. Henkelman and H. Jónsson, "Improved tangent estimate in the nudged elastic band method for finding minimum energy paths and saddle points," J. Chem. Phys. 113, 9978–9985 (2000).

[314] G. Henkelman, B. P. Uberuaga, and H. Jónsson, "A climbing image nudged elastic band method for finding saddle points and minimum energy paths," J. Chem. Phys. 113, 9901–9904 (2000).

[315] G. Henkelman and H. Jónsson, "A dimer method for finding saddle points on high dimensional potential surfaces using only first derivatives," J. Chem. Phys. 111, 7010–7022 (1999).

[316] R. A. Olsen, G. J. Kroes, G. Henkelman, A. Arnaldsson, and H. Jónsson, "Comparison of methods for finding saddle points without knowledge of the final states," J. Chem. Phys. 121, 9776–9792 (2004).

[317] A. Heyden, A. T. Bell, and F. J. Keil, "Efficient methods for finding transition states in chemical reactions: Comparison of improved dimer method and partitioned rational function optimization method," J. Chem. Phys. 123, 224101 (2005).

[318] J. Kästner and P. Sherwood, "Superlinearly converging dimer method for transition state search," J. Chem. Phys. 128, 014106 (2008).

[319] P. Lindgren, G. Kastlunger, and A. A. Peterson, "Scaled and Dynamic Optimizations of Nudged Elastic Bands," J. Chem. Theory Comput. 15, 5787–5793 (2019).

[320] E. L. Kolsbjerg, M. N. Groves, and B. Hammer, "An automated nudged elastic band method," J. Chem. Phys. 145, 094107 (2016).

[321] E. D. Hermes, K. Sargsyan, H. N. Najm, and J. Zádor, "Accelerated Saddle Point Refinement through Full Exploitation of Partial Hessian Diagonalization," J. Chem. Theory Comput. 15, 6536–6549 (2019).

[322] E. D. Hermes, K. Sargsyan, H. N. Najm, and J. Zádor, "Geometry optimization speedup through a geodesic approach to internal coordinates," J. Chem. Phys. 155, 094105 (2021).

[323] E. D. Hermes, K. Sargsyan, H. N. Najm, and J. Zádor, "Sella, an Open-Source Automation-Friendly Molecular Saddle Point Optimizer," J. Chem.

Theory Comput. **18**, 6974–6988 (2022).

[324] https://github.com/QuantumMisaka/ATST-Tools (2024).

[325] L.-W. Wang, L.-S. Xie, P.-X. Xu, and K. Xia, "First-principles study of magnon-phonon interactions in gadolinium iron garnet," Phys. Rev. B **101**, 165137 (2020).

[326] X. He, N. Helbig, M. J. Verstraete, and E. Bousquet, "TB2J: A python package for computing magnetic interaction parameters," Comput. Phys. Commun. **264**, 107938 (2021).

[327] A. I. Liechtenstein, M. Katsnelson, V. Antropov, and V. Gubanov, "Local spin density functional approach to the theory of exchange interactions in ferromagnetic metals and alloys," J. Magn. Magn. Mater. **67**, 65–74 (1987).

[328] T. Zhang, Y. Cao, B. Zhang, H. Guo, L. Qiao, F. Li, and Z. Li, "Short-range order and strong interplay between local and itinerant magnetism in $GeFe_3N$," Phys. Rev. B **110**, 224419 (2024).

[329] G. Pizzi, V. Vitale, R. Arita, S. Blügel, F. Freimuth, G. Géranton, M. Gibertini, D. Gresch, C. Johnson, T. Koretsune, J. Ibañez-Azpiroz, H. Lee, J.-M. Lihm, D. Marchand, A. Marrazzo, Y. Mokrousov, J. I. Mustafa, Y. Nohara, Y. Nomura, L. Paulatto, S. Poncé, T. Ponweiser, J. Qiao, F. Thöle, S. S. Tsirkin, M. Wierzbowska, N. Marzari, D. Vanderbilt, I. Souza, A. A. Mostofi, and J. R. Yates, "Wannier90 as a community code: new features and applications," J. Phys. Condens. Matter **32**, 165902 (2020).

[330] N. Marzari and D. Vanderbilt, "Maximally localized generalized wannier functions for composite energy bands," Phys. Rev. B **56**, 12847–12865 (1997).

[331] Q. Wu, S. Zhang, H.-F. Song, M. Troyer, and A. A. Soluyanov, "Wanniertools: An open-source software package for novel topological materials," Comput. Phys. Commun. **224**, 405–416 (2018).

[332] V. I. Lebedev and D. N. Laikov, "A quadrature formula for the sphere of the 131st algebraic order of accuracy," Doklady Mathematics **59**, 477–481 (1999).